Improving the interface stability of cross-linked films by ink formulation in printed organic light emitting diodes

Hibon, Pauline

(2020)

TECHNISCHE UNIVERSITÄT DARMSTADT

Improving the interface stability of cross-linked films by ink formulation in printed organic light emitting diodes

at the Material Science Faculty of the Technische Universität Darmstadt

submitted in fulfilment of the requirements for the degree of Doctor-Engineer (Dr.-Ing.)

Doctoral thesis by M.Eng. Paulie Hibon, born in Reims (France)

First assessor: Prof. Dr. **Heinz von Seggern**
Second assessor: Prof. Dr. **Edgar Dörsam**

Darmstadt 2020 (year of the viva voce)

Pauline Hibon: Improving the interface stability of cross-linked films by ink formulation in printed organic light emitting diodes
Darmstadt, Technische Universität Darmstadt,
Year thesis published in TUprints 2020
Date of the viva voce 11.09.2020

Table of content

Erklärung zur Dissertation

Hiermit versichere ich, die vorliegende Dissertation ohne Hilfe Dritter nur mit den angegebenen Quellen und Hilfsmitteln angefertigt zu haben. Alle Stellen, die aus Quellen entnommen wurden, sind als solche kenntlich gemacht. Diese Arbeit hat in gleicher oder ähnlicher Form noch keiner Prüfungsbehörde vorgelegen. Eine Promotion wurde bisher noch nicht versucht.

Darmstadt, den 05.10.2020

(Pauline Hibon)

1. Introduction

The first display in form of a cathode ray tube was demonstrated in 1897 by the Nobel-prize physicist and inventor Karl Ferdinand Braun. The basic operation consists of an electron gun firing electrons onto a phosphor-coated screen leading to image formation. Colours appeared in 1954 and it was the most popular display technology utilised for television and computer monitors until the arrival of liquid crystal displays in 1968, which gradually replaced the cathode ray tubes. Electroluminescent displays were not commercially ready until the late 1970's when Sharp Corporation introduced the so-called alternating-current-thin-film approach.[1] Organic (i.e., carbon-based) electroluminescence emanated in the late 1980's with the first Organic Light Emitting Diode (OLED) by Tang et al.[2] The use of polymers as electrically conductive materials was revealed by inadvertence in the late 1970's by Shirakawa and co-workers at the Tokyo University.[3] The advantage of using polymers as electronic materials is that they combine the electronic properties of semiconductors with the ease of processability of plastics. The first conjugated polymer-based OLED, also called PLED was demonstrated in 1990 at the Cavendish laboratory using poly(phenylene vinylene) (PPV).[4] It established that light emitting devices could be made with organic and solution-processed materials.[5] Thus, OLED has become an established technology in the display market because of their very high luminous efficiency, low power consumption, and long lifetime thanks to complex multilayer architectures.[2, 4, 6-8]

Display application is boosted by a race for higher performance, such as higher resolution and lower price. Unlike thermal evaporation,[9] solution processes are lowering production costs due to high material usage and ease of scalability for different sizes.[10] For solution-processed OLED display fabrication techniques, inkjet printing (IJP) has the potential to be the state-of-the-art technology for high resolution R-G-B pixel definition.[11-14] However, some challenges related to the soluble OLED technology have to be understood and overcome, e.g., the influence of different molecular orientations and the intermixing between layers.[15]

Intermixing between successive solution-processed layers was shown to damage the previously deposited layer and to be hard to prevent.[16-18] Therefore, interface control remains a top challenge of solution-processed OLEDs since device performance heavily relies on it. Such undefined interfaces are detrimental to OLED performance (e.g., shifted emission zone),[19] but also for quantum dot based PLEDs.[20] Due to the nanometre thickness of the layers composing these devices, even the smallest interface mixing affects their performance.

To control interfaces, several approaches such as orthogonal solvent[21-22] or cross-linked materials[23-25] have been intensively studied. Dummy buffer layers have proved to stop intermixing but add an additional layer to an already complex architecture[26]. For preventing this effect fast drying was used to shorten the diffusion time of the solvents in the wet state.[27-28]

Orthogonal solvents are of interest especially when low molecular weight or non-cross-linkable materials are used. Finding such solvent can be complicated, since two consecutive layer materials must show a significant difference in their polarity or solubility profile.[29-31] Besides the solubility/orthogonality challenge, other criteria have to be taken into account such as solvent/print-head compatibility, low toxicity of the solvent, low amount of impurities that could diminish device performance, and impact of the solvent itself on the overall device. In this work, the focus was set on

cross-linked materials. Material characterisation is generally performed by a lab-scale soluble process, i.e., spin coating. Unlike IJP, the method of choice for display fabrication, spin coating offers a fast-drying speed to the processed layer, and drying speed is a driving force for reducing strong mixing of two subsequent layers. For this reason, film stability of an inkjet deposited and cross-linked layer against subsequent exposure to a suitable inkjet printing solvent has been investigated. Impact of ink solvent on solution-cast thin film properties has already been studied for polyvinyl acetate films.[32-33] The objective was to determine the influence of the ink solvent on the cross-linking degree of a polymer in thin films.

This work concentrates on the stability of a hole transport layer (HTL) against a subsequent solution deposition of an emissive layer (EML) ink. The emissive material is composed of small molecules known to be very mobile in multilayer stacks. Sharp interfaces between the HTL and the EML were proven essential to guarantee an efficient exciton confinement within the EML layer by avoiding shifted emission zones.[34] Thus, OLED device efficiency is directly affected by the interface sharpness between HTL and EML.[35]

The theoretical principles used in this thesis are described in Chapter 2. Chapter 3 illustrates the detailed experimental conditions and settings. In this thesis, the studied polymer solutions were first characterised to differentiate them from one another by describing the polymer-solvent interaction in solution (Chapter 4). The interactions were determined experimentally and based on empirical descriptions, like Kramer equation, Huggins equation and Solomon Cuita equation. Thereafter, the polymer cross-linking reaction was examined in the bulk material and in the films (Chapter 5). Differential scanning calorimetry (DSC) was used to quantify the efficiency of polymer cross-linking reactions in powder and in films processed from different solvents. The stability of polymer films against solvent exposure was inspected with the aim to identify the impact of ink solvent on the film stability. An understanding of the correlation between cross-linking reaction efficiency in film and film stability against solvent exposure was drawn. Finally, OLED devices were produced with the aim to study the influence of HTL ink solvent on optical and electrical properties of the devices (Chapter 6). A summary and outlook constitute the final Chapter 7 of this thesis.

2. Theory

2.1. OLED introduction and architecture

Electroluminescence in organic materials was first demonstrated in 1963 by Pope et al.[36] and in 1965 by Helfrich and Schneider[37] with a single layer OLED. They observed green light emission from a layer of an anthracene crystal sandwiched between two electrodes biased with 400 V. When voltage is applied across the two electrodes, an electrical current is generated, and charge carriers of opposite polarity are introduced into the layers which upon recombination converted to light. This proof-of-concept OLED, composed of a transparent anode, a combined transport and emissive layer and a metallic cathode, suffered from high voltage and poor power-conversion efficiency. In 1987, Tang and Van Slyke presented the first multilayer OLED stack[2] introducing an ultra-thin monopolar hole transport layer (HTL) in combination with an ultra-thin electron transport layer (ETL) as seen in Figure 2.1 which acted simultaneously as emissive layer between the anode and cathode resulting in lower driving voltages and improved electroluminescent emission efficiency. Since then, more advanced stack designs were used to create OLED devices with more and more functional layers.[38] The overall stack thickness is usually in the range of few hundred of nanometres.

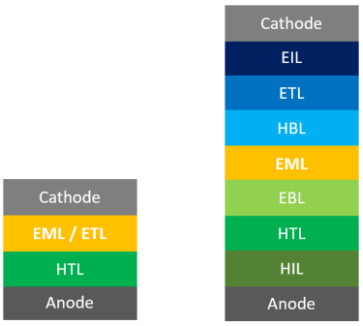

Figure 2.1: Development of OLED stacks from two functional layers to a multilayer structure. (left) Two layers OLED from Tang and van Slyke published in 1987. (right) A complex OLED structure commonly used in recent devices. It consists of charge carrier injection layers (HIL, EIL), transport layers (HTL, ETL), blocking layers (HBL, EBL) located on either sides of the central emission layer (EML).

Modern OLEDs consist of multiple thin films of organic layers sandwiched between two electrodes. In order to enhance the injection of charge carriers from the electrodes into the organic layers, a hole (/electron) injection layer (HIL/EIL) is added followed by a hole (/electron) transport layer (HTL/ETL). Efficient confinement of hole and electrons in the emissive layer can be improved by hole (/electron) blocking layers (HBL/EBL). This avoids the loss of electrons and holes from the emissive layer and leads to an efficiency increase. The anode has to be transparent to guarantee the light output and commonly consists of indium tin oxide (ITO). The cathode is normally reflective and made of metals such as aluminium.

Working principle of OLED

The semiconductor properties of organic materials, no matter whether small molecules or polymers, are based on conjugated bonds, i.e., π-orbitals "filled with" delocalised electrons, which impact the electronic and optical properties of the materials. An overlap of atomic orbitals results in a set of new

orbitals called bonding and anti-bonding molecular orbitals. Electrons in π-orbitals provide a lower stabilisation than those in σ bond. Figure 2.2a shows the two different types of bond. As a consequence, the energy gap between bonding (π) and anti-bonding molecular orbital (π*) is smaller than in the case of σ bonding. The highest occupied π state is called HOMO and the lowest unoccupied molecular orbital (π^*) is called LUMO. The energy gap (E_g) of a molecule is determined by the energy difference between HOMO and LUMO. An energetic representation of these bond types is depicted in Figure 2.2b.

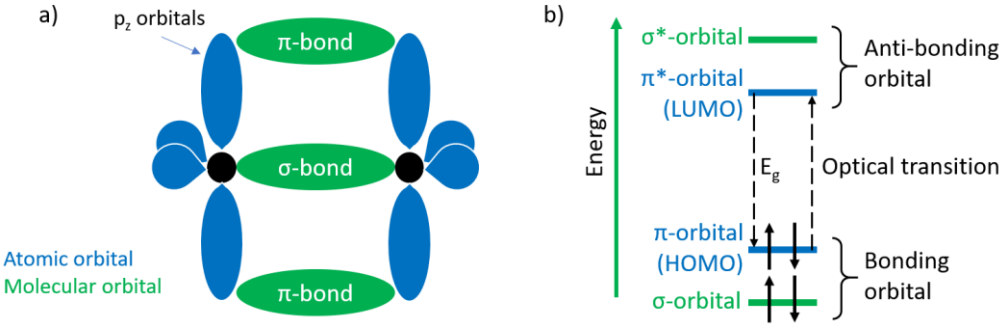

Figure 2.2: a) Schematic representation of p_z-orbitals, σ- and π-bonds between two carbon atoms. b) Energy levels of bonding (π)and antibonding orbitals (π^*).

Positive charges, designated as holes, are injected from the Fermi level of the anode into the HOMO of the neighbouring organic layer, and the electrons are injected from the Fermi level of the cathode into the LUMO of the neighbouring organic layer under applied positive bias voltage V_0. The voltage induced electric field forces electrons and holes to move towards each other to preferentially recombine in the EML resulting in photon emission. Thanks to a high HTL LUMO and a low ETL HOMO, the electrons and the holes are confined in the EML. The energy gap E_g of the emissive species in the EML determines the frequency of the emitted light, i.e., the emitted light colour. The working principle of an OLED under electrical field is represented in Figure 2.3.

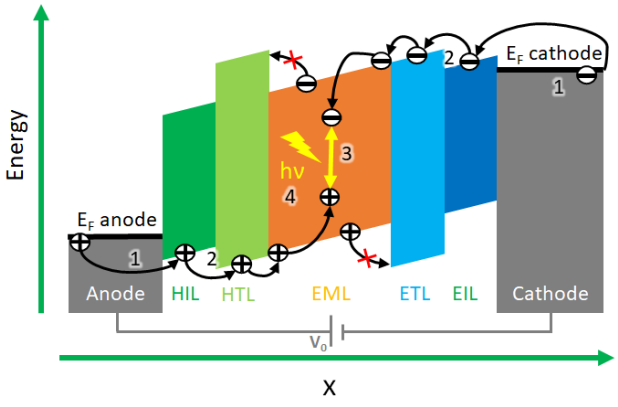

Figure 2.3: Schematic representation of the fundamental processes of an OLED in operation. (1) Charge carrier injection. (2) Charge carrier transport. (3) Recombination of the charge carriers to excitons. (4) Emission of light.

Charge injection

Charge carrier injection corresponds to the introduction of holes and electrons into the HOMO and the LUMO of the organic layer from the anode and the cathode, respectively. However, for charge carrier injection to happen, there are injection barriers $E_{b,e}$ for electrons and $E_{b,h}$ for holes that must be overcome, as shown in Figure 2.4.

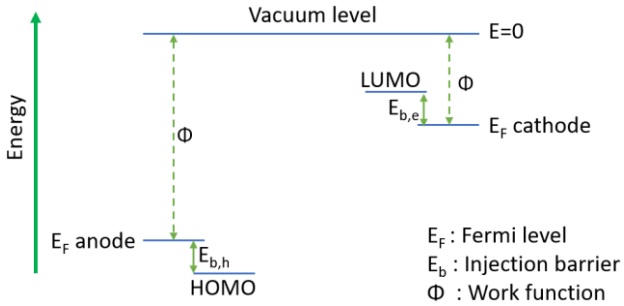

Figure 2.4: Energy diagram of injection process from the electrodes in an OLED device.

When applying an external electric field to the OLED device, the electron and hole injection barriers can be overcome. Alignment of Fermi level of the cathode and the anode takes place with the LUMO and the HOMO levels of the adjacent molecules, respectively, resulting in charges injection.[39] Reducing the injection barriers from the electrodes to the organic layers can be achieved by choosing high work function anodes, whereas the cathode consists mainly of metals with low work function. Another strategy is to select the organic materials so that the HOMO (/LUMO) of the HIL (/EIL) lays closely to the Fermi level of the anode (/cathode).

Charge transport

Movement of charge carriers within organic layers can be described by the hopping mechanism, developed by Bässler in 1993.[40] This kind of transport can be illustrated as a succession of redox reactions between identical partners. Disorder in amorphous solid is responsible for the formation of spatially and energetically discrete states following a statistical distribution with a Gaussian shape. This density of states (DOS) has an energetic width of about 0.1 eV.[41]

Electron transport takes place on the LUMO level and hole transport on the HOMO level of the organic material. The moving direction of charge carriers is established by the applied electric field. Hopping from one site to sites with lower energy requires no energy, whereas hopping from one site to sites with higher energy requests energy to overcome the energetic barrier. The hopping distance of charge carriers is typically ~ 1 nm, which is in the same order of magnitude as the intermolecular distances. The frequency of hopping processes, determining the mobility of charge carriers, strongly depends on the electric field and temperature.[40] The hopping mechanism is represented in Figure 2.5. The mobility of charge carriers in organic semiconductors is generally in the range of $10^{-2} – 10^{-7}$ $cm^2 \cdot V^{-1} \cdot s^{-1}$, which is significantly lower than that of inorganic semiconductors.[42]

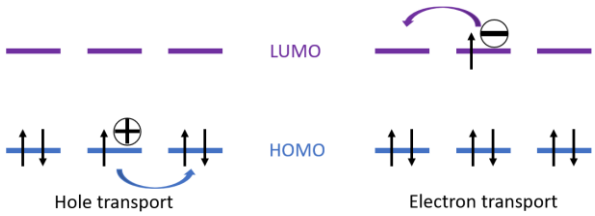

Figure 2.5: Hopping mechanism responsible for charge transport in OLED device.

Charge recombination and light generation

For the recombination of electrons and holes to occur in the emissive layer, both charge carriers need to be within a certain distance of each other called the effective interactive capture radius r_c, and is defined as:[43]

$$r_c = \frac{e^2}{4\pi\varepsilon\varepsilon_0 k_B T} \tag{2.1}$$

where ε is the dielectric constant and ε_0 is the vacuum permittivity, k_B is the Boltzmann constant 1.38×10^{-23} $m^2{\cdot}kg{\cdot}s^{-2}{\cdot}K^{-1}$, e is the elementary electron charge 1.6021765×10^{-19} C and T is the temperature. This capture or recombination radius is on a length scale of 10 nm. Due to Coulomb attraction, an excited state is created by combining an electron and hole on a single molecule, called exciton. This exciton can now diffuse and radiatively decays within an area of the OLED, named the recombination zone. The location of the recombination zone depends on the balance of both charge carriers; it can be located close to the anode if there is a majority of electrons or close to the cathode in case of holes. Within the emissive layer, the exciton migrates to the emitting molecules by intermolecular energy transfer called Dexter or Förster transfers, see Figure 2.6. The exciton is thereby defined by its binding energy. Relaxation and light emission take place locally on the emitting molecules; the higher the binding energy, the more localised the exciton is.

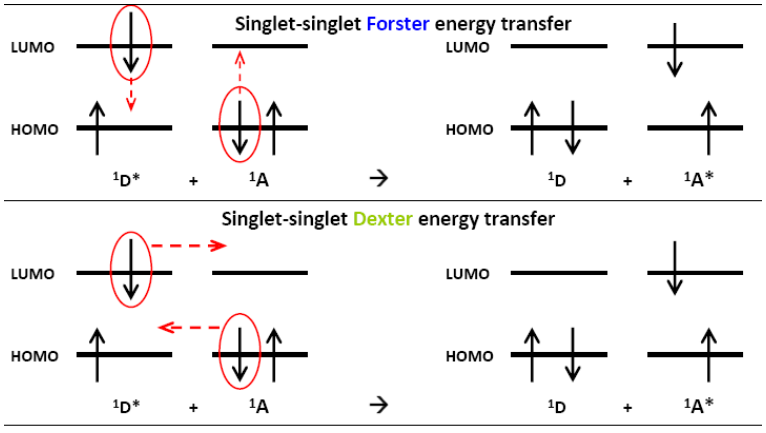

Figure 2.6: Förster and Dexter energy transfer schematics. Reprinted from reference.[44]

Spin statistics states that electron and hole both carry a spin of -1/2 and +1/2. During recombination of the charge carriers, two different spin orientations are possible.[45] The parallel orientation shows three-fold degeneracy and is called triplet state, whereas the anti-parallel is referred as singlet state. Consequently, they are formed in a 3/1 ratio. In fluorescent materials, the light emission from pure singlet excitons limits the internal quantum efficiency to 25%. For a radiative decay to occur from the

triplet states (phosphorescence), intersystem crossing from triplet to singlet states is performed by using materials containing heavy metals.[46] These materials, also referred as triplet or phosphorescent dopants, can harvest both singlet and triplet excitons and achieve a theoretical quantum efficiency of 100%, see Figure 2.7.[46]

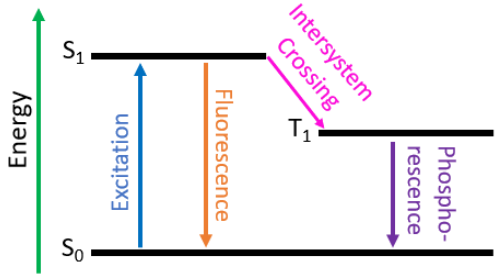

Figure 2.7: Simplified energy diagram representing different light emission mechanisms. Fluorescence and phosphorescence process are illustrated. S_0, S_1 and T_1 designate the singlet ground state, the first singlet excited state and the first triplet excited state, respectively.

2.1.1. Material deposition process

Electroluminescent materials can be divided in two types: small molecules[2] and polymers[47]. The choice of material is determining the deposition process of thin film organic layer. While small molecules can be deposited by thermal vacuum evaporation and solution process, polymers can only be processed out of solution (e.g., printing techniques[4]). Thin films of OLED materials in this work are prepared by physical vapour deposition (PVD) and by inkjet printing. The details of the deposition techniques and their application will be discussed below.

Physical vapour deposition process

Physical vapour deposition (PVD) is the most commonly used deposition process for OLEDs since its introduction by Tang and VanSlyke in 1987.[2] Under low pressure, pure materials are evaporated from crucibles at elevated temperatures. Typically, OLED materials are evaporated at a pressure below 10^{-7} mbar at relatively low temperature (< 300°C). The crucibles are resistively heated and controlled using a thermocouple allowing regulation of the evaporation rate and the deposition rate. Thereby the organic material is sublimed and the vapour propagates along the line-of-sight path towards a cooled substrate, where it condenses to form a film. Using pure material under low vacuum makes PVD one of the cleanest methods for material deposition. Cleanliness of the OLED fabrication method is critical to achieve high device performance and long lifetime. PVD has several other advantages such as precise control of thickness at the nanometre scale. It allows depositing complex multilayer stacks of a wide range of materials with no interaction between subsequent layers. To control the lateral distribution, the use of shadow masking is necessary and widely used for both lighting and display applications. However, the alignment between mask and substrate is facing technological and physical limitations when very fine patterning is requested, such as in high-resolution displays. In addition, the process of evaporation under vacuum limits the panel size which must fit inside the chamber. In the recent years, roll-to-roll thermal-evaporation was developed to enable the fabrication of large area and flexible OLEDs.[48]

Solution process

In contrast, solution processes are compatible with large area substrates. For example, glass substrates of 2.5 metres x 2.8 metres are coated by roll-to-roll processes allowing large scale material deposition on both flexible and rigid substrates.[10] The main advantage of solution processes is their cost effectiveness. This is of high interest for OLED display costs to be competitive compared to LCDs and plasma technologies. Solution processes can be used to deposit all organic layers, including small molecules and polymer materials, with a very efficient material utilisation. Indeed, materials are deposited only on the active areas of the substrate, unlike PVD which deposits material over the whole substrate and the walls of the evaporation chamber. The "wet" deposition is compatible with a roll-to-roll process on flexible substrates such as plastic films. Nonetheless, building complex multilayer structures by soluble processes remains challenging. Each layer must be insoluble in the solvent used to deposit the subsequent layer.[49] This can be done by cross-linking the subjacent layer or by using orthogonal solvents to process the next layer.[50] Typically, soluble OLEDs fully processed from solution are limited to three or four organic layers, whereas OLED processed from PVD can be composed of more than ten layers.

Solution processes combine spin coating and printing. A low amount of ink is deposited onto a substrate which spins to homogenise the thin film by centrifugal forces in the spin coating process. Printing includes various processes, such as inkjet printing, screen printing, gravure, offset lithography and flexography. For solution-processed OLED display fabrication, inkjet printing has the potential to be the state-of-the-art technology for high R-G-B pixel definition.[11-12] Patterning is used to set the resolution of the overall display creating subpixel arrangements.[51] Homogeneity is critical in both inter- and intra- pixel film thickness, since inhomogeneous layer thickness results in poor colour distribution, high voltage and lower device lifetime.

2.1.2. Soluble organic semiconductors

Both small molecules and polymers can be processed from solution as introduced in the previous sections. The main difference between the two material classes is their weight distribution. Polymers have a broad weight distribution and are referred as polydisperse materials, whereas small molecules are monodisperse. Besides, the chain length of conjugated polymers can influence strongly the solution viscosity which is an important criterion in solution processes. Both small molecules and polymer materials can be used for hole injection, hole transport and/or emissive layers. In this work, the hole injection and transport layers are made of polymers and the emissive layer of solution processable small molecules.

Emissive materials: Small molecules

Small molecules were used in this work in the EML where holes and electrons recombine. The EML can be either composed of one single material (undoped layer) or a mixture of materials (doped layer). The non-doped configuration suffers from close packing in the solid state which leads to excimer (excited dimer) and exciplex (excited complex) formation. Fluorescence quenching is hard to prevent in the case of a single material in the EML.[52] Nonetheless, aggregation of emitting molecules in the solid state can be avoided in doped layers, i.e., a matrix composed of a small amount of emitting material (usually 1-10%) diluted in a host material. This matrix configuration prevents luminescence quenching.

Charge carriers are injected in the HOMO and the LUMO of the host material, followed by exciton formation.

Combining emitters opens the possibility for a wide range of emissive colours, like white which can be created with red, green and blue emitters,[53] or yellow and blue emitters.[54] Unlike polymers, small molecules can be synthesised with very high purity, since they can be purified by recrystallisation and sublimation.

Hole injection and hole transport materials: Polymers

The use of polymers in electronic applications has been made possible by Alan J. Heeger, Alan G. MacDiarmid and Hideki Shirakawa in 1977 thanks to the discovery of iodine doped polyacetylene exhibiting a high electrical conductivity.[55]

In this work, polymers are used for hole injection and hole transport. These materials must have a low-lying HOMO comparable to the Fermi level of the anode to allow for efficient injection and transport of holes into the HIL, the HTL and finally into the emissive layer (EML). In the case of the HTL, a high-lying LUMO is needed to block negative charge carriers coming from the cathode. Attaching side chains to the polymer helps tuning its solubility as well as its electronic and mechanical properties. Commonly used hole transport materials are depicted in Figure 2.8.[56]

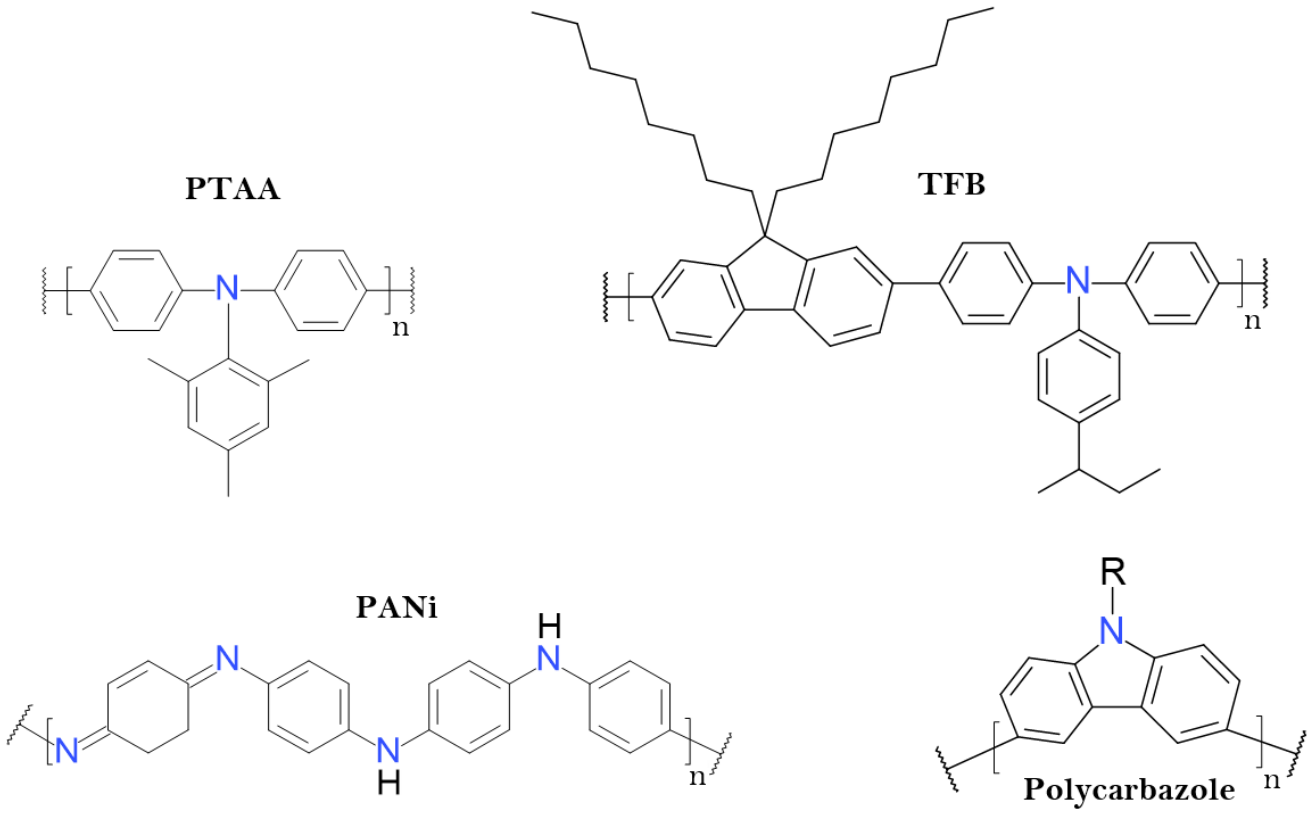

Figure 2.8: Chemical structure of common hole transporting materials.

PTAA stands for poly[bis(4-phenyl)(2,4,6-trimethylphenyl)]amine and is an excellent hole transport and electron blocking material.[57] Polyaniline is written as PANi and TFB corresponds to poly(9,9-

dioctylfluorene-alt-N-(4-sec-butylphenyl)-diphenylamine), a common hole transport polymer.[58-59] Polycarbazole shows strong interchain charge transport properties through hopping.[60]

Polymer materials are composed of a succession of monomers which are classified depending on their functionality. Three monomer types exist: amine, backbone, and cross-linker units. The amine monomer controls the HOMO level and the charge transport properties. The backbone is responsible for the rigidity of the material. Side chains attached to the backbone help for a good material solubility. Cross-linking units added to the polymer chain enhance mechanical, thermal and chemical resistance properties after the cross-linking reaction has been successfully performed. The cross-linking chemistry is discussed in the following section.

Cross-linker units

Cross-linking units can be thermally or photochemically activated, like styrene and acrylate moieties, respectively.[61] The cross-linking process leads to the creation of a covalent bond between two or more molecules. It forms a network encompassing the entire system. A fully cross-linked polymer can only be swollen in a solvent, it cannot be dissolved. These cross-linking units are widely used for solution processable OLED materials.[61] The challenge is the degree of cross-linking, which characterises how complete the cross-linking reaction succeeded. Indeed, remaining unreacted cross-linking units can significantly reduce device performance and lifetime.

It exists a wide range of cross-linker units used for OLED devices.[61] Siloxane was reported for the first time to be used for cross-linking in an OLED device in 1999.[25] Despite strong and stable resulting bonds, water and alcohols were found in the film and behave as impurities. Styrene moieties can be attached to small molecules and polymers to perform cross-linking by thermal activation. Consequently, the material to which the styrene is attached must be stable at its reaction temperature. Besides these popular cross-linker units, trifluorovinylether, benzocyclobutene, oxetane, cinnamate and chalcone, are also used for cross-linking in OLED devices.

2.2. Inkjet printing of thin films

Inkjet printing is the method of choice for various organic electronic applications such as OLEDs,[4] OPVs[62] and OFETs.[63] As introduced in Chapter 2.1.1, the main reason is that inkjet printing offers high precision control over numerous substrates without the need of shadow masking. This non-contact deposition technique is one of the most cost-efficient ways of producing complex pattern thanks to its efficient use of materials.

2.2.1. Instrumentation and operation mode

Continuous inkjet printer[64] and drop-on-demand (DoD) inkjet printer[65] are the two commercial types of inkjet printers. Commercial marking and coding of products and packages are mainly produced by continuous printers, whereas drop-on-demand inkjet printers are used for organic electronics applications.[66]

A continuous inkjet printer is composed of a fluid reservoir which supplies the ink, one or more nozzles and electrostatically charged plates. The droplet is ejected from the nozzle(s) and the charged plates

deflect the droplet so that it reaches the desired position on the substrate. A cup is used to collect the droplets that should not be printed on the substrate.

In opposite, DoD inkjet printer consists of a low fluid impedance nozzle[67] and a thermal or piezoelectric actuator which generates a pressure pulse in the fluid to push a droplet out of the nozzle. The landing of the droplet is controlled by a highly precise mechanical system that moves the print-head in two dimensions and the substrate holder in one dimension leading to the positions of the desired pattern, see Figure 2.9c. The droplet ejection process is displayed in Figure 2.9a from a continuous inkjet printer and in Figure 2.9b from a DoD printer. The display industry favours DoD inkjet printers as being able to create complex pixelated structures with the dimensions and precision needed for state of the art OLED performance.[68]

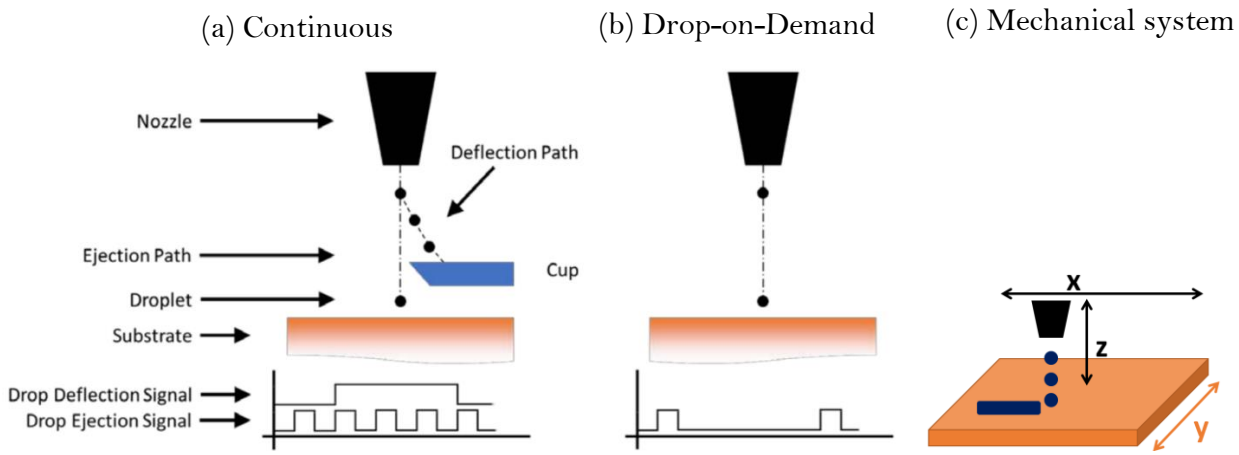

Figure 2.9: Schematics of (a) continuous, (b) Drop-on-Demand printing. Droplet ejection process from the print-head reprinted from reference.[69] (c) Schematics of mechanical system control of the substrate holder and the print-head in one and two dimensions, respectively.

2.2.2. Print-heads

As introduced in Chapter 2.2.1., DoD inkjet printers can use thermal or piezoelectric inkjet print-heads. The extreme heat needed to form a droplet from a thermal print-head is unfavourable for its use in printed electronics. Therefore, piezoelectric inkjet print-heads are the system of choice. A schematic diagram of a piezoelectric inkjet print-head is illustrated in Figure 2.10.

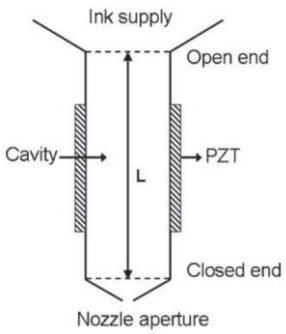

Figure 2.10: Schematic diagram of a piezoelectric inkjet print-head. Reprinted from reference.[66]

In piezoelectric inkjet print-heads, the piezoelectric material converts electrical energy into mechanical deformation of the ink chamber resulting in a pressure change in the chamber. This leads to the formation and ejection of a drop from the nozzle. Different modes of deformation are possible and represented in Figure 2.11.

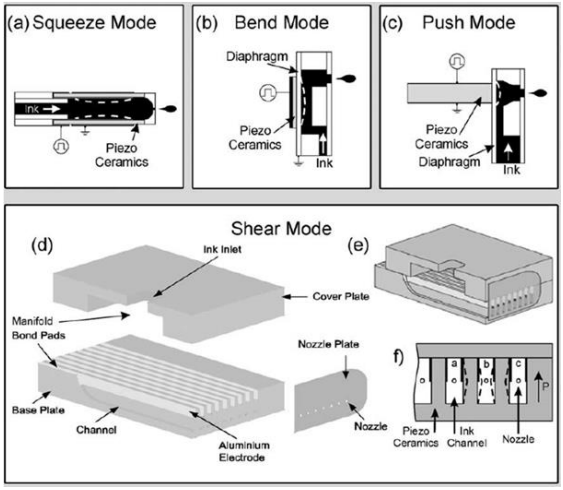

Figure 2.11: Different piezoelectric element arrangement in drop-on-demand inkjet print-heads. Reprinted from reference.[70]

The ink reservoir is connected to the capillary cavity by an open end. A pressure line is also linked to the ink supply in order to aspirate and flush ink through the print-head for maintenance. The capillary cavity is enveloped by a piezoelectric actuator running at eigenfrequency. The print-head ends with a nozzle aperture from where droplets are generated from the ink. The diameter of the nozzle is much smaller than the cavity, thus it is called a closed end. To avoid dripping of ink from the nozzle, a slight under-pressure is applied. A droplet is formed by applying a generally square shaped waveform with double-peak. For the Dimatix print-head DMC, the eigenfrequency is 12 kHz. To produce a 10 pL droplet from DMC, the nozzle diameter is of 21.5 µm and the applied under-pressure is 2 mbar compared to the surrounding pressure. The Q-class print-head requires an under-pressure of 25 mbar.

When a positive pressure wave approaches the nozzle, a droplet is generated if the amplitude and velocity of the wave are large enough. The surface energy needed to form a droplet at the nozzle plate must be exceeded by the amount of kinetic energy transferred outwards.[71] In addition, due to the decelerating action of ambient air, the velocity of a droplet necessitates to be several metres per second so that the droplet can meet the targeted landing position.[72] Generally, piezoelectric print-heads can process ink with a viscosity lower than 20 mPa·s and surface tensions between 20 $mN \cdot m^{-1}$ and 70 $mN \cdot m^{-1}$.

2.2.3. Challenges

Despite the advantages of inkjet printing techniques presented in Chapter 2.1.1, ink jetting through the nozzle(s) and film formation are challenging steps of the process.

Droplet formation

In the case of a piezoelectric inkjet print-head, a droplet is formed by the piezoelectric crystal excited by an electrical pulse, called waveform,[73] which can be tuned accordingly to the ink viscosity,

concentration and surface tension. Changes in the waveform directly impact the droplet velocity which is targeted at 4-5 $m \cdot s^{-1}$. The droplet volume is not only influenced by the nozzle diameter, but also strongly by the waveform[66] and printer type. The volume can vary between 1 pL to 20 pL, it should be chosen in line with the pattern resolution wanted, or rather the display resolution (individual pixel size). In this work, droplet of 10 pL were printed. Printing in a pixelated substrate requires a stable droplet, which includes reproducible droplet formation at high frequency and a reproducible droplet landing. This can be achieved when the droplet forms an angle of less than 1° with the line perpendicular to the substrate.

The droplet formation through a nozzle typically shows a non-Newtonian fluid behaviour. After the pulse ejecting the fluid out of the nozzle, the droplet remains attached to the nozzle by a filament. Then, a pinch point is formed right above the droplet which breaks the connection to the nozzle and a filament appears. The filament undergoes thinning and either retracts back into the droplet or it can eventually break up into satellite droplets of much smaller volume.[66] Satellite droplets and long filament can create misprints in the desired patterning resulting in inhomogeneous printing, problematic especially for functional printing. No droplet formation might occur due to mismatch of fluid surface tension and the print-head material. Elastic stresses are associated to the behaviour of polymer solution, as suggested by Schubert et al.[74] This behaviour stops operating for very viscous solution of high concentration, or made with high molecular weight materials. In this case, capillary forces cannot break the filament and the droplet bounces back to the nozzle plate. The different stages of droplet formation are depicted in Figure 2.12.

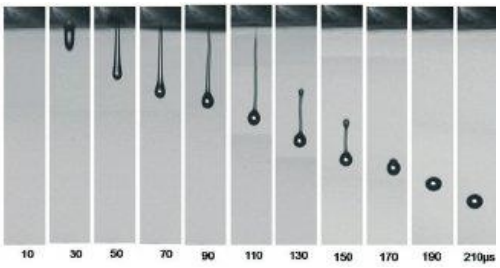

Figure 2.12: High speed photographic images of droplet formation from a DoD printer. Through time, the droplet is attached to the print-head by a ligament, which then breaks into satellite. Finally, they retract to the leading droplet. Reprinted from reference.[75]

The printability of conjugated polymers can also be affected by inter-chain interaction and thus impacts film morphology. Solvent polarity, its aromatic nature and polymer concentration are important parameters influencing the degree of inter-chain interactions.[76]

Large area film formation

The inkjet printing technique using high boiling point solvents, exhibit a great challenge concerning film formation. In the frame of this work, large area squares (4 cm^2) must be printed in order to pursue thin film characterisation techniques. In order to reach a flat and smooth film, the first criterion is that every droplet printed on a substrate must merge to the neighbouring one without a big overlap. The droplet spacing should be smaller than the critical value but too small droplet spacing bring film instabilities.[76] The impact of the droplet spacing on line formation is depicted Figure 2.13, where the droplet spacing decreases from (a) to (d). The critical value is reached between the droplet spacing displayed in (a) and (b), where merging occurred.

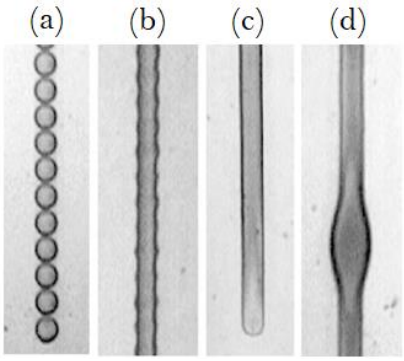

Figure 2.13: Pictures of liquid droplets on a substrate where the droplet spacing was varied to test the critical value of droplet merging and the beginning of line formation. (a) Droplet spacing is too large for the drops to merge together. (b) Droplet spacing is above the critical value and drops merge together resulting in a line formation with a periodic irregularity. (c) When the droplet spacing is optimised, a line with parallel sides is formed. (d) Droplet spacing is very small and a bulging instability forms along the line. Reprinted from reference.[77]

To satisfy the prerequisite for successive droplets to merge together, the ink solvent should exhibit a low contact angle with the substrate.[78] In addition, a levelling time larger than the drying time assures a homogeneous printed layer.[79] While drying, one commonly encountered effect is the coffee-ring effect, which remains being a considerable challenge, see Figure 2.14a. Deegan et al. demonstrated that the pattern of this ring-like shape is a consequence of a faster solvent evaporation at the boundary of a droplet with a pinned contact line and of a surface tension gradient at the surface.[80-81] In the case of such a pinned contact line, represented in Figure 2.14c, an outward flow of fluid takes place due to loss of fluid by evaporation at the edges. Therefore, there is a constant material motion towards the edges which produces a coffee ring effect, whereas without pinned contact line, the diameter of the droplet shrinks due to fast evaporation resulting in a homogeneous drying process, see Figure 2.14b. The resulting surface tension gradient generates as well a material flow towards the edges, this phenomenon is called the Marangoni effect. The coffee ring effect can be eliminated by the use of solvents mixtures of various boiling points generating consistent drying everywhere in the droplet and thus a more homogeneous film.[66]

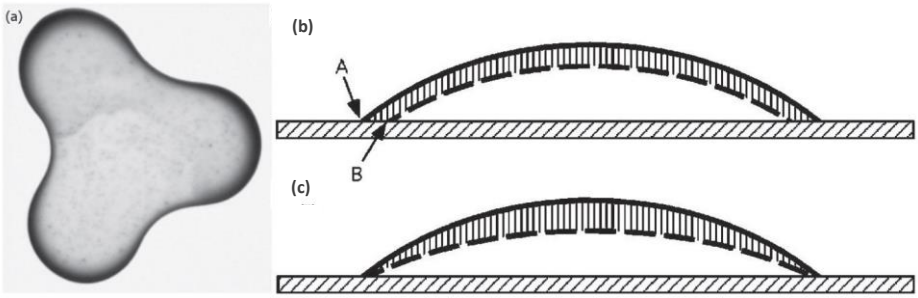

Figure 2.14: (a) Schematic representation of drying process of a droplet. (b) A droplet having an unpinned contact line leads to droplet shrinking while drying, whereas (c) a droplet having a pinned contact line exhibits a coffee ring effect. Reprinted from references.[80-81]

Experiments by Moon et al. using inkjet printed aqueous droplets of suspended silica particles revealed that the contact angle of the ink has an influence on drying patterns (Fig. 3).[82] They found that when the ink formed a high contact angle with the substrate, coffee staining did not occur. However, high contact angle inks are not preferred for a homogeneous film deposition by inkjet printing. Indeed, while drying, a film has the tendency to shrink. Thus, inkjet printing requires a consequent work on ink formulation, including polymer properties (molecular weight), solvent choice (viscosity), in order to reach targeted thickness, roughness and homogeneity.[83]

2.3. IJP inks: Polymer solutions

In this work, the focus is set on polymer solutions, which can be seen as a mixture of long macromolecular chains and small molecules of solvents.[84] Due to diverse conformations that the flexible chains may take, special methods must be taken into account. In order to study the physical-chemical properties of polymers in solution, the mixture must be in the dilute regime where no interaction between the chains is taking place or is reduced to a minimum. In dilute solutions, individual macromolecules properties are studied, whereas in concentrated solutions, the chains are entangled and consequently the contribution of a single macromolecule cannot be evaluated.

2.3.1. Polymer solubility profile

Complete polymer dissolution can occur instantaneously but can also last up to days or weeks. Billmeyer Jr. identified polymer dissolution following two steps.[85] First the polymer swells, then second the dissolution itself takes place. The polymer coil, together with solvent molecules attached, adopts a thermodynamic arrangement in solution, as displayed in Figure 2.15.

Figure 2.15: Schematic representation of the dissolution process for polymer molecules. In a theta solvent, the polymer coil adopts a spherical form.

The rule of thumb stating "like dissolves like" gives a good appreciation of polymer solubility.[86] (Non)Polar solvents dissolve (non)polar solutes. Yet, polymer dissolution depends on many other parameters, such as molecular weight, branching, degree of cross-linking and crystallinity. An increase of molecular weight, at constant temperature, leads to a decrease in polymer solubility. The same behaviour is observed as the degree of cross-linking increases. Indeed, the cross-linked polymer hinders interaction between polymer chains and solvent molecules, rendering them insoluble and resulting in a swollen gel. When the solubility of a polymer cannot be directly determined by standard measurements, an indirect method allows understanding the solubility range of a polymer and the ink stability. The Non-solvent Induced Phase Separation (NIPS) is a well-established technique also known as Loeb-Sourirajan method, as well as immersion precipitation and Diffusion Induced Phase Separation (DIPS).[87] To perform this method, three components are needed: a polymer, a solvent and a non-solvent for the investigated polymer. A typical ternary NIPS, illustrated in Figure 2.16, was used to describe an ink stability, i.e., the capability of an ink to remain a single-phase system while non-solvent is added.

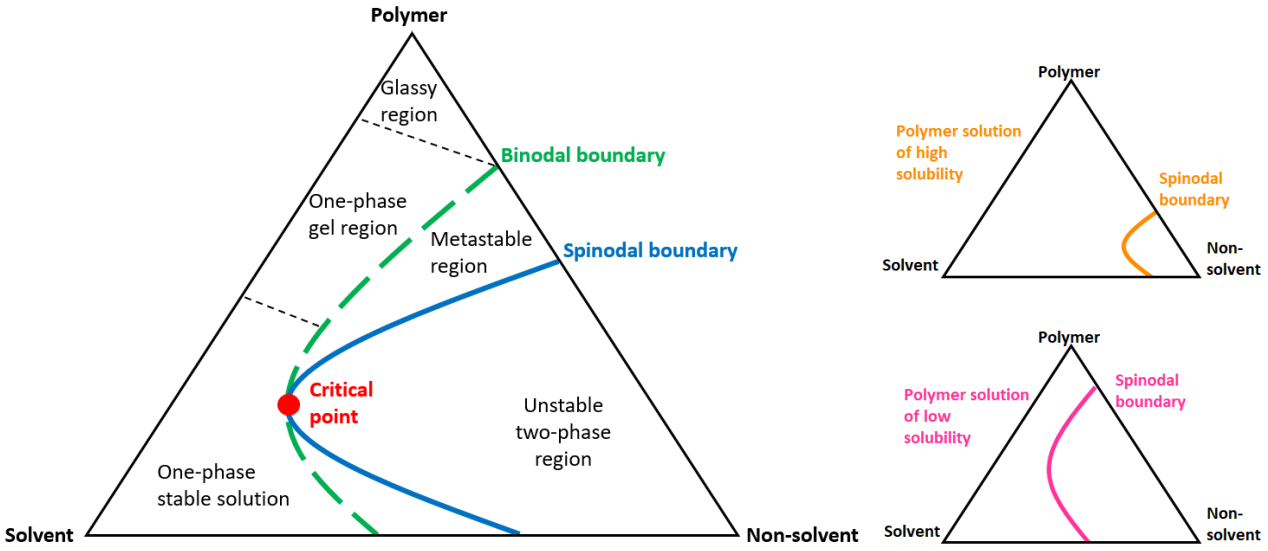

Figure 2.16: (left) Diagram of ternary Non-solvent Induced Phase Separation (NIPS). (right) Phase diagrams of polymer solutions presenting the variation of the spinodal boundary depending on their solubility.

The corners represent the pure components and any point contained in the diagram equals to a mixture of the three components. The spinodal curve is the limit of a solution stability standing for the boundary of absolute instability of a solution to decompose into multiple phases. In the one-phase region the polymer solution is thermodynamically stable. As more non-solvent is added, the composition of the solution changes, the attractive forces between polymer segments become stronger than the polymer-solvent interactions. Then, the solution enters the binodal and spinodal phases, where demixing occurs. These boundaries can be determined by visual observation of cloud points, meaning when the solution changes from clear to turbid. To perform the NIPS method, the pure non-solvent is added slowly to a stirred polymer solution. The system solvent needs to be miscible with the non-solvent to perform NIPS. A polymer exhibiting a high solubility in a given solvent has wide soluble concentration range, hence a small binodal region in the phase diagram.

2.3.2. Size of polymer chain in solution

Polymers chains are composed of many carbon atoms. The backbone of a conjugated polymer consists of an alternation of single and double bonds. While more rigid than a polymer consisting of only single bonds, twisting between monomers can occur in conjugated polymers thanks to the alternation.[88] Therefore, long polymer chains can adopt a lot of different conformations. Polymer chains form tightly folded coils which can be entangled to each other; due to their flexibility the chains adopt a random coil formation as depicted in Figure 2.17. These coils hold together thanks to cohesive and attractive intra- and inter-molecular forces (e.g., dispersion, dipole-dipole interaction, induction, and hydrogen bonding).

Figure 2.17: Scheme of polymer arrangement in random coil.

The volume occupied by a polymer in solution is defined by the radius of gyration R_g, calculated as the average squared distance of any point in the polymer coil from its centre of mass. R_g can be experimentally determined by light scattering. The conformation of a polymer dissolved in a solvent depends on many parameters such as their polarity, chemical characteristics and solubility parameter.[89] A *good* solvent for a given polymer confers stronger polymer-solvent interactions than polymer-polymer attraction forces. In this system, the polymer volume marked by R_g increases and the segments are "solvated" instead of "aggregated" as in the solid state. One way to measure this interaction is by rheological methods. Rheology is a measure of the fluid resistance being deformed by shear stress. The viscosity of a polymer solution is distinctive of the dissolved polymer concentration and its size. High polymer solution viscosity is due to intermolecular frictions created by distorting the flow lines around individual particles. The most popular drag flow rheometer is a cone-plate rheometer which usually consists of a rotating upper plate (small-angle cone) and a fixed lower plate with a fluid sample contained between them. The applied torque is measured with the programmed motion.

The radius of gyration R_g differs from the hydrodynamic radius R_h. R_g describes the distribution of mass centres in the polymer coil, whereas R_h varies depending on both mass and polymer conformation. Therefore, the shape of the polymer, whether it is spherical, random-coiled or rod-like, can be determined by R_h. The hydrodynamic diameter d_h is defined by the Stokes-Einstein equation as:

$$d_h = 2R_h = \frac{kT}{3\pi\eta D} \tag{2.2}$$

where d_h is the hydrodynamic diameter, R_h is the hydrodynamic radius, k is the Boltzmann constant 1.38×10^{-23} $m^2{\cdot}kg{\cdot}s^{-2}{\cdot}K^{-1}$, T is the temperature, η is the viscosity of the polymer solution and D is the diffusion coefficient. The factor $3\pi\eta$ corresponds to the friction coefficient ζ introduced in the Nernst-Einstein equation, which can be applied to any form of particles in solution.

Another method to define the polymer volume in a solvent is by using the Einstein equation which describes the relationship between hard sphere volume and viscosity in a dilute system:

$$\eta_r = \frac{\eta}{\eta_s} = 1 + 2.5\Phi \tag{2.3}$$

where η_r is the relative viscosity, η is the viscosity of the suspension, η_s is the viscosity of the suspending solvent and Φ is the volume fraction of particles in the suspension. This model can be transferred to macromolecules with necessary considerations, which are not perfect spheres in solution. The coefficient 2.5 corresponds to the intrinsic viscosity of a hard sphere in a very dilute system. For macromolecules, the Einstein equation should be adapted including the intrinsic viscosity. It can be

inferred that for a polymer dissolved in a *poor* solvent, conferring stronger polymer-polymer attraction forces than polymer-solvent interactions, the resulting viscosity of the solution should be small. Thus, rheology is a tool to record solvent interaction with a given polymer.

2.3.3. Interaction between polymer and solvent

As described in the previous Chapter 2.3.2, polymer-solvent interactions determine the volume fraction of a polymer in solution but also the conformation of a polymer coil. Thus, in a *good* solvent, the random polymer coil adopts an unfolded conformation due to the strong polymer-solvent interactions. Inversely, in a *poor* solvent, the polymer-solvent interactions are smaller than the attraction forces between chain segments, so the random polymer coil adopts a tight and contracted conformation. In a *very poor* solvent, the random polymer coil is so contracted that it can eventually precipitate. In this case, the polymer is in a "non-solvent". The different conformations are illustrated in Figure 2.18.

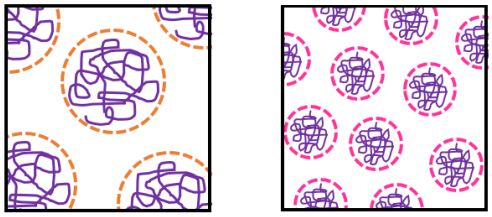

Figure 2.18: Schematic of polymer size in solution made from a good solvent (left) and from a bad solvent (right).

The Einstein equation (2.3) can be rearranged by converting the volume fraction to solution concentration using the intrinsic viscosity, a measure of molecular density. The coefficient 2.5 in Eq. 2.3 corresponds to the intrinsic viscosity of a hard sphere in a very dilute system. The volume fraction Φ of solids in suspension is practically the concentration of a material in solution. Thus, the equation can be rewritten as:

$$\eta = \eta_s(1 + [\eta]c) \tag{2.4}$$

where η is the viscosity of the polymer solution, η_s is the viscosity of the solvent in mPa·s, c is the concentration of polymer in solution in g·dL^{-1} and $[\eta]$ is the intrinsic viscosity of the polymer in the specific solvent in dL·g^{-1}. The unit of intrinsic viscosity is volume per unit mass. The intrinsic viscosity is inversely proportional to molecular density. Therefore, a dense polymer molecule has a low intrinsic viscosity. Since the measure of polymer solution viscosity is determined by the volume fraction of solids in the suspension, a polymer with a high intrinsic viscosity has a strong impact on the solution viscosity.

The Kuhn-Mark-Houwink-Sakurada equation, often referred to as the Mark-Houwink equation, describes how the intrinsic viscosity of a polymer is affected by molecular weight, structural characteristics and the solvent affinity (*good* or *poor* solvent) in which the polymer is dissolved. If the Mark-Houwink parameters k and a are known, the intrinsic viscosity of a polymer in a specific solution can be resolved as follow:

$$[\eta] = k \cdot Mw^{a} \tag{2.5}$$

where $[\eta]$ is the intrinsic viscosity of the polymer in the specific solvent, Mw is the molecular weight, and k and a are the MH parameters. The intrinsic viscosity can also be determined by measuring the viscosity of the polymer solution over a range of concentrations and fitting the Huggins or Kraemer equations.[90] These empirical observations will be detailed in Chapter 4.

3. Investigated System and Methods

The hole transport material under investigation was processed from five different inkjet printing solvents. The interaction between the polymer and each solvent was characterised by various techniques in solution. The resulting inkjet printed polymer film properties were determined to understand their stability against solvent exposure. Finally, OLED devices were built to evaluate the impact of the HTL ink solvent on their electrical properties.

3.1. Materials

In this work, two classes of organic semiconductors were used. The HIL consists of a mixture of a polymer and small molecules. For the HTL, a polymer is employed. A blend of small molecules composes the EML where the molecules either emit light or transport charge carriers. The HIL, HTL and EML were processed from solution. The ETL and the EIL consist of small molecules that were deposited by PVD. Unlike polymers whose molecular weight is over 20,000 g·mol^{-1}, small molecules exhibit a molecular weight of up to 3000 g·mol^{-1} which enables them to be either evaporated under high vacuum or processed from solution.

3.1.1. Hole transport materials

X-Po, a Merck cross-linkable hole transport material, described in the patent WO2013/156130 A1 as polymer Po2,[91] is the main investigated polymer in this thesis. The molecular weight of the X-Po batch is 82 kg·mol^{-1}. The hole transport layer material consists of a random co-polymer, whose monomers are displayed in Figure 3.1.

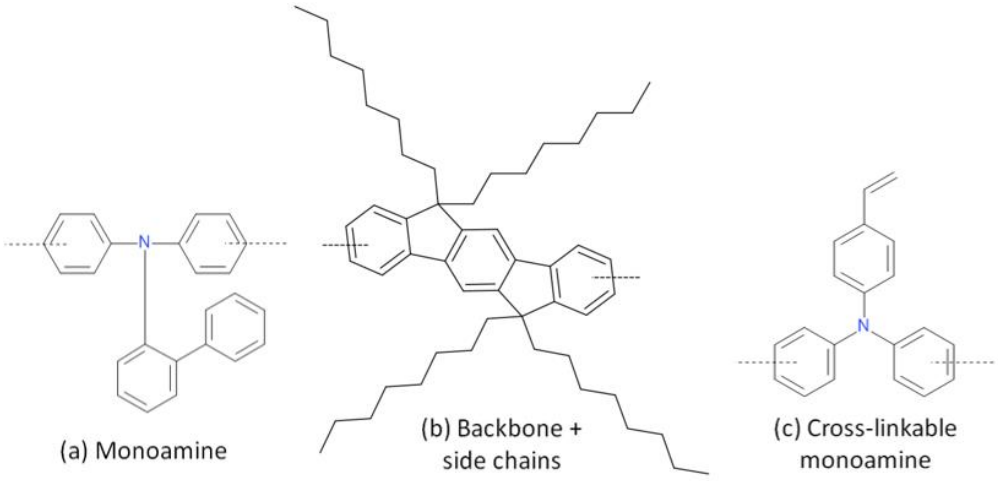

Figure 3.1: Monomer units forming the two polymers used in this work. The different monomers drawn from (a) to (c) were present in the polymers to the proportions displayed in Table 3.1. The dashed lines each indicate the continuation of the polymer chain.

Po, the non-cross-linkable version of X-Po, was also studied. X-Po and Po differ in the presence of a cross-linkable unit, whose ratio between the different monomer units is reported in Table 3.1. These were the following monomers: (a) a triaryl amine (TAA) unit, (b) the backbone where side chains are attached which have the purpose to increase the chain solubility, and (c) a TAA hosting a thermally cross-linkable group. The cross-linkable group consisted of a styrene-type cross-linker.

Table 3.1: Monomer units contained in X-Po and Po.

Polymer	(a) Monoamine	(b) Backbone + side chains	(c) Cross-linkable monoamine
X-Po	40%	50%	10%
Po	50%	50%	0%

Figure 3.2 displays the absorption spectra of the two hole transport materials measured from spin coated films processed from toluene. The absorption edge is at 436 nm, which results in a calculated energy gap $E_g = \frac{hc}{\lambda}$ of 2.84 eV for both polymers. The HOMO values were measured in films by photoelectron spectroscopy in air using a Riken AC3. The LUMO values were estimated by adding the calculated energy gap to the Riken HOMO level. The HOMO and LUMO levels of both polymers are listed in
Table 3.2.

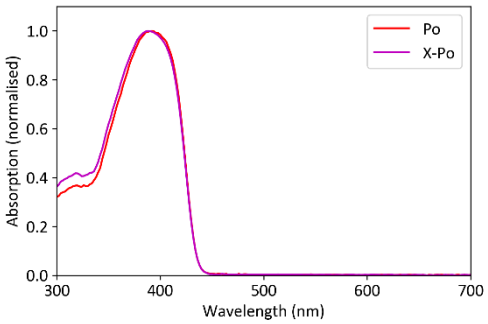

Figure 3.2: Absorption spectra of the hole transport materials measured in spin coated films processed from toluene.

Table 3.2: HOMO and LUMO levels of X-Po and Po. HOMO values of the hole transport materials measured by photoelectron spectroscopy (Riken) and the calculated LUMO of these materials.

Polymer material	HOMO (Riken)	LUMO (Riken + Abs.)	$E_g = hc/\lambda$
X-Po	-5.61 eV	-2.77 eV	1240/436 = 2.84 eV
Po	-5.58 eV	-2.74 eV	1240/436 = 2.84 eV

3.1.2. Inkjet printing solvents

To process organic semiconductors from solution, and more specifically for inkjet printing, the chosen solvents must obey specific criteria. Their surface tension should allow for the formation of well-shaped droplets after ejection from the print-head, see Chapter 2.2.3, and they should wet the substrate. In addition, the solvents need a low viscosity, especially taking into account that linear polymers show a

strong increase in viscosity with concentration. Further, solvents with a high boiling point were chosen to avoid clogging of the 21.5 µm diameter nozzles of the print-head. At the same time, the processing of organic semiconductors from solution requires that the materials have good solubility in the solvents and that the solvent should be chemically inert to the materials dissolved therein.

The under these boundary conditions selected solvents used in this work were 1-methylnaphthalene (1-MYN), 1-methoxynaphthalene (1-MXN), 3-phenoxytoluene (PXT), cyclohexyl hexanoate (CYX) and menthyl isovalerate (MISO). They are listed with their physical properties and their structural formulas in Table 3.3. All these solvents are liquid at room temperature and their boiling points are 244°C and 248°C for 1-methylnaphthalene and cyclohexyl hexanoate, respectively, 269°C for 1-methoxynaphthalene and 270°C for 3-phenoxytoluene as well as for menthyl isovalerate. The following organic solvents were purchased from Sigma Aldrich in a purity of 98%: Menthyl isovalerate, 1-methylnaphthalene, 1-methoxynaphthalene and 3-phenoxytoluene. The solvents were purified by distillation to a purity of more than 99 %, as judged by gas chromatography analysis. Cyclohexyl hexanoate was bought from ABCR in a purity of 99%. For titration test, ethanol and acetone were purchased from Sigma Aldrich in a purity of more than 99.5% and used as received.

Table 3.3: Inkjet printing solvents used in this work to process the hole transport material.

CAS number	**Solvent name**	**Acronym**	**Surface Tension at 22°C (in $mN \cdot m^{-1}$)**	**Viscosity at 25°C (in mPa·s)**	**Boiling Point at 1 atm (in °C)**	**Chemical Structure**
90-12-0	1-Methyl naphthalene	1-MYN	38.3	3.0	244	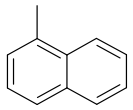
2216-69-5	1-Methoxy naphthalene	1-MXN	42.0	6.0	269	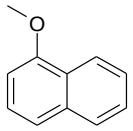
3586-14-9	3-Phenoxy toluene	PXT	37.8	4.4	270	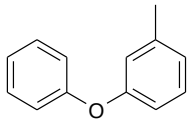
6243-10-3	Cyclohexyl hexanoate	CYX	28.7	3.5	248	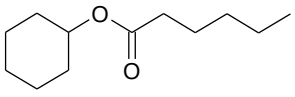
16409-46-4	Menthyl isovalerate	MISO	26.5	5.9	270	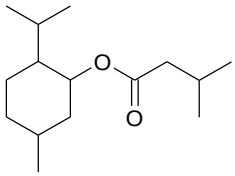

1-Methylnaphthalene, 1-methoxynaphthalene, 3-phenoxytoluene, cyclohexyl hexanoate and menthyl isovalerate have been chosen so that various surface tensions and boiling points could be tested. These

five solvents cover a meaningful range of surface tensions and boiling points applicable to inkjet printing, see Figure 3.3.

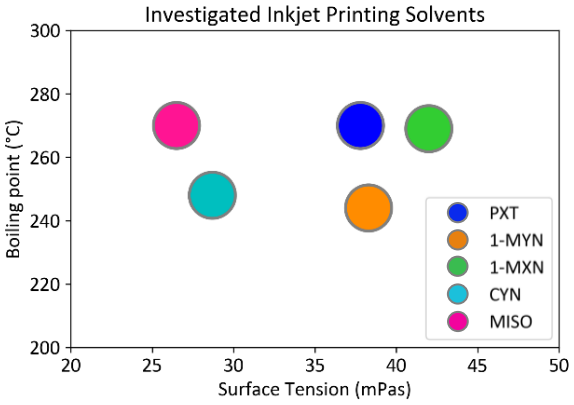

Figure 3.3: Mapping of surface tension and boiling point of the investigated inkjet printing solvents.

3.1.3. Ink formulations

All compounds for the ink preparation were handled by weight. First, the solid material or solid material mixture was weighted and filled into a glass bottle. After being purged with argon for at least 20 minutes, the solvent was added dropwise with a glass pipette. In case of a solvent mixture, the solvent with the highest solubility was first added to dissolve the solid. Then, the other solvents were added. The dissolution occurred at room temperature under magnetic stirring in argon atmosphere. After complete dissolution of the material, the ink was seeping through a 0.2 µm PTFE filter into a brown bottle with argon overlay. The inks for inkjet printing were additionally degassed at a reduced pressure of 25 mbar for five minutes. The amount of prepared ink varied accordingly to the print-head used to process it. Five millilitres of ink were prepared for DMC cartridges and 30 ml for Q-class print-head reservoirs.

The inks for the hole injection layer (HIL) and the emissive layer (EML) are composed of a material mixture solubilised in a solvent mixture. The hole transport layer (HTL) ink consists of a single material dissolved in a single solvent.

Solubility test

In order to determine the solubility of a material in a given solvent, a solubility test was performed in the same way as for an ink formulation. The highest concentration at which the material completely dissolved was recorded.

3.1.4. Solution characterisation

To examine the properties of the employed polymer solution, the system was characterised with established and newly developed methods. Therefore, the affinity between polymer and solvent was investigated, the hydrodynamic radius of the polymer chains in the solvents were measured, the polymer solution viscosity was recorded at room temperature after heat treatment and the volatility of the solvent from a polymer film was studied.

Polymer-solvent affinity

Polymer-solvent affinity was determined using a precipitation/demixing test based on the NIPS technique, introduced in Chapter 2.3.3.[87] Ethanol was considered to be a *poor* solvent for X-Po. It was used to precipitate the polymer X-Po from solution of each solvent utilised in the present study. A 1.5 mL solution of polymer X-Po was prepared at 30 $g \cdot L^{-1}$ with each solvent in glass bottles. The high concentration of 30 $g \cdot L^{-1}$ facilitated the visualisation of the precipitation onset. Ethanol was added to the mixture dropwise under magnetic stirring. The beginning of precipitation was determined visually as the moment the solution turned turbid. The amount of ethanol added at which the mixture started to precipitate was recorded. The more ethanol was needed to start the precipitation of the polymer solution, the stronger was the interaction between polymer and solvent. Such strong interaction was characteristic of a *good* solvent[92] for X-Po.

Size of particles in solution: Hydrodynamic radius R_h

The size and organisation of the polymer in solution was investigated by light scattering methodologies.[93] "Classical light scattering", also called "static" or "Rayleigh" scattering is employed to directly measure the weight-average molecular weight of a polymer (M_w). "Dynamic light scattering" (DLS), also known as "photon correlation spectroscopy" (PCS) or "quasi-elastic light scattering" (QELS) can be used to measure the rate of diffusion of polymer particles in solution. This diffused light collected from the Brownian motion of polymer particles is sensitive to the presence of very small amounts of aggregated polymer particles and can deliver the polymer size distribution over a large range of masses. Thereby small particles diffuse rapidly, whereas large particles diffuse slowly. Additionally, the speed of diffusion also depends on the viscosity of the dispersant.

The size distribution obtained by DLS is representative for the light intensity that is scattered by particles in suspension of diverse diameters. If the sample is polymodal (more than one discrete peak) and polydisperse (broad peak), it is recommended to use the Mie theory to convert the intensity distribution to a volume distribution by considering the refractive index of the polymer solution. The volume representation of a polymodal and polydisperse sample provides a more real picture of the proportions of the particle sizes in solution.[94] DLS measurements were carried out with disposable plastic cuvettes at 25°C. In order to utilise the volume representation, the viscosity of the solution had to be introduced to the software.

Viscosity

Viscosity measurements were carried out using a HAAKE MARS rheometer (Modular Advanced Rheometer System), see Figure 3.4. The viscosity was measured in a cone-plate geometry over a range of shear rates from 0.5 to 1000 s^{-1} with 20 logarithmically spaced steps at a constant temperature of 25°C. The temperature was controlled by a Peltier plate with 0.2°C accuracy. A small fluid sample (1.3 mL) was placed with an Eppendorf pipette in the space between a fixed lower plate of radius r (TMP60) and a rotating cone of the same radius with a very small angle α (C60/1°). The sample must have a free spherical shaped surface at the outer edge to insure an accurate measurement.[95]

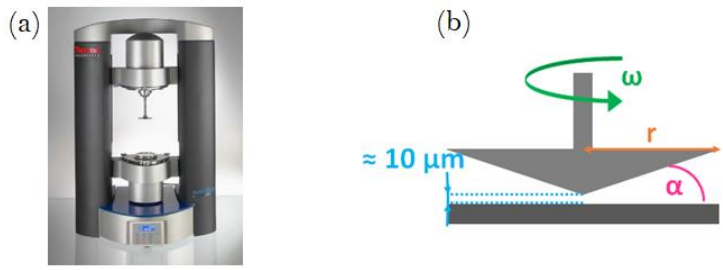

Figure 3.4: HAAKE MARS rheometer. (a) Photo of the measurement equipment.[44] (b) Diagram of rotation cone and fixed lower plate.

The viscosity of a polymer solution varies under the influence of many parameters, such as solution concentration, solution impurities, polymer molecular weight, measurement temperature and pressure. Generally, low concentrated polymer solutions exhibit a Newtonian behaviour, following Newton's law of viscosity:

$$\sigma = \eta \cdot \dot{\gamma} \tag{3.1}$$

where σ is the shear stress in Pa, η is the viscosity in mPa·s and $\dot{\gamma}$ is the shear rate in s^{-1}. The shear stress is also defined as $\sigma = \frac{F}{A}$, where F is the force applied and A is the cross-sectional area parallel to the applied force. The shear rate is determined by $\dot{\gamma} = \frac{v}{h}$, where v is the velocity of the plate and h is the distance between the plate and the cone. By introducing the angular speed ω, the shear rate can be expressed by $\dot{\gamma} = \frac{v}{h} = \frac{r\omega}{r \tan \alpha} \approx \frac{\omega}{\alpha}$, where r is the plate radius and α is the angle of the cone.

A Newtonian or a non-Newtonian behaviour can be determined by the response of a fluid to shear stress. In a Newtonian fluid, the shear stress has a linear relationship with shear rate, as shown in Figure 3.5. In a non-Newtonian fluid, the shear stress does not exhibit a linear dependence with shear rate. One distinguishes shear thickening which describes a solution whose viscosity increases with shear rate and shear thinning when the viscosity decreases with shear rate. Shear thickening can be a problem while printing, because it can cause nozzle clogging.[96] On the other hand, shear thinning makes droplet formation also problematic. For inkjet printing, a viscosity between 2 mPa·s and 30 mPa·s is recommended with an optimum value at 10 mPa·s.

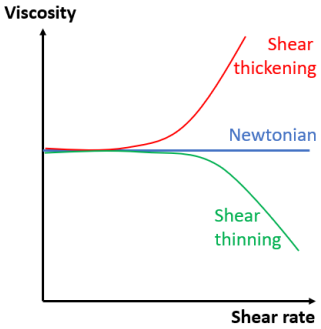

Figure 3.5: Graphical representation of viscosity change of polymer solutions over a wide range of shear rates. A Newtonian solution and two non-Newtonian solutions, one presenting shear thickening and the other one shear thinning are represented.

Surface tension

The KRÜSS DSA100, depicted in Figure 3.6, was used for surface tension (SFT) analysis of pure solvents and inks by calculating the SFT through liquid density and two-dimensional shape analysis. This calculation method is called the pendant drop method. The contour of the drop is extracted by

the function "profile detection" which analyses the picture contrast. The surface tension is calculated by a fit of the Young-Laplace equation to the pendant drop contour.

Figure 3.6: Photograph of KRÜSS DSA 100 used for surface tension and contact angle measurement. [44]

The measurements were carried at room temperature in air with pendant drops of 15 µL (± 5 µL). The temperature was recorded to perform rigorous calculations. The SFT results give information about the printability and the jettability of a solvent or an ink. To jet an ink through the nozzle plate, a minimum surface tension should be respected. To provide a good nozzle plate wetting and an adequate droplet formation, an optimal surface tension of 30 mPa·s is recommended. However, droplet wetting on the substrate is limiting the upper range of the surface tension. A maximum of 40 $mN \cdot m^{-1}$ is the upper limit enabling a uniform wetting of the ink in the pixelated substrate used in this work.

Cross-linking in solution

The cross-linkable polymer X-Po was dissolved in the different solvents of Table 3.3 at a concentration of 50 $g \cdot L^{-1}$. Each of the polymer solutions was divided into multiple glass bottles of 1 mL each, so that each bottle could be heated at a specific temperature. After degassing and argon overlay, the bottles were sealed. The bottles were surrounded by an aluminium block placed on a hotplate covering the whole bottle except the cap. Each of these bottles was annealed at a fixed temperature for three hours under constant stirring. After annealing, the bottles were placed into a cold-water bath to cool down back to room temperature. The viscosity of the solutions before and after the annealing procedure was measured at room temperature with a shear rate of 500 s^{-1}, following the procedure explained in Chapter 3.1.4 *Viscocity*.

Solvent volatility

The drying behaviour of the polymer solution is characteristic for the polymer-solvent interactions. The volatility correlates with the binding energy between polymer chains and solvent molecules. Weak polymer-solvent interactions lead to a fast evaporation of solvent under vacuum since polymer chain interactions are preferred. However, due to the speed of evaporation of solvent at the interface of air and polymer solution, the surface dries much faster than the bulk resulting in a polymer-rich surface and trapped solvent in the bulk.

In this work, the volatility of the solvent was defined by the solvent residue contained in the bulk after drying the solvent under vacuum. Therefore, the polymer solutions of 5 $g \cdot L^{-1}$ were poured inside a DSC pan in a volume of 30 µL. The pans were placed in a vacuum chamber and were exposed to a

pressure of 10^{-4} mbar for two hours. The volatility of a solvent from the polymer solution was calculated as:

$$r_s = \frac{m_s}{m_f} \cdot 100 \tag{3.2}$$

$$m_s = m_f - \left(c \cdot \frac{m_i}{d_s}\right) \tag{3.3}$$

where r_s is the solvent residue in weight percent, m_s is the mass of solvent residual in bulk, m_f is the total mass after drying of material and solvent residue, c is the polymer solution concentration, m_i is the mass of the wet film and d_s is the solvent density.

3.2. Processing of an inkjet printed layer

As introduced in Chapter 2.1.1, solution processing is offering a high material utilisation and is therefore the most cost-effective deposition technique for OLED devices. Due to the high precision at which the material is deposited onto a substrate, inkjet printing is a promising technology for high resolution display applications.

3.2.1. Inkjet printer

To process solution layers by inkjet printing, the research printer Pixdro LP50 from Meyer Burger was used, see Figure 3.7. Numerous printing parameters (e.g., waveform, printing frequency, pattern…) can be adjusted in the software of the printer. Two different print-heads were used during this work to adapt to the printing needs. Dimatix cartridges (DMCs) are disposable print-head cartridges that can contain up to 2 mL of ink. They are preferred for testing new inks, for example newly developed solvents or materials, due to its low material consumption. The print-head is composed of 16 nozzles, while only one nozzle was activated to print to increase precision. The second print-heads used are Fujifilm Q-Class™ Emerald heads which are commonly used for industrial applications and display best-in-class jetting accuracy. An ink reservoir of 30 mL is attached to the print-head consisting of 256 nozzles. The nozzles of both print-heads are aligned on one row and the nozzles are separated by 254 µm. The Q-Class print-head is used for reference inks and for pre-testing inks before industrial application. A reference ink is an ink that was tested several times; its process and resulting film performance are known. A reference ink is printed at every experiment to show that the process is reproducible. With this knowledge the performance of the thin films resulting from the new inks can be analysed. To fabricate OLED devices, two Pixdro LP50 printers were used, one located in a cleanroom 100 in air, and the other in a glovebox in nitrogen atmosphere.

Figure 3.7: Pixdro printer LP50.[44]

3.2.2. Printing substrates

To test inks developed for display applications, pixelated substrates were used to study film formation of inks and OLED device performance. The dimensions and layout of subpixels define the resolution of a display. The substrates used in this work had 135 x 45 subpixels with a pixel density of 80 pixels per inch (PPI) in the diagonal direction. Each subpixel measured 212 µm x 64 µm. A grouping of 33 x 11 subpixels defined one pixel with an active area of 4.606 mm² and an aperture ratio of 39.1%. The four active pixels were surrounded by a so-called "dummy" area, represented by the yellow dotted area in Figure 3.8a. Using a dummy area is a well-known technique to eliminate drying patterns caused by inhomogeneous drying (e.g., faster drying at the edges compared to the centre of the substrate). It enables a constant layer thickness of the respective printed material across the whole substrate resulting in homogenous light emission of fabricated OLEDs. The design of a pixelated substrate is shown in

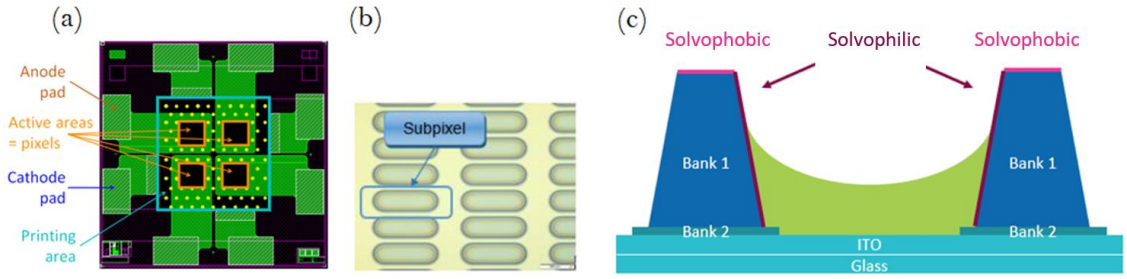

Figure 3.8.

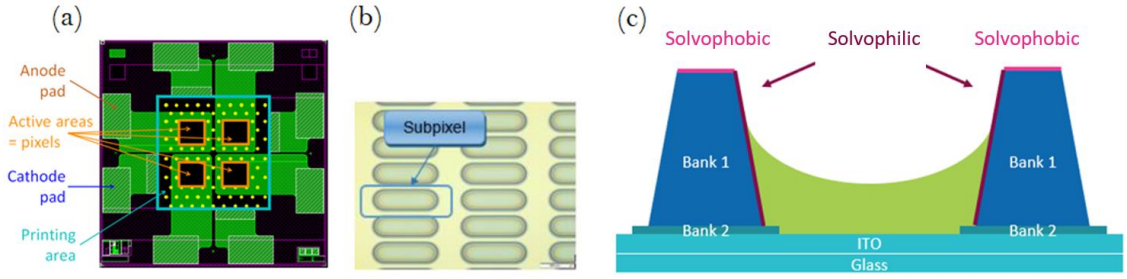

Figure 3.8: (a) Photograph of an inkjet printing substrate of 30 x 30 mm² containing four pixels with an active area of 4.606 mm². (b) Microscope picture of a subpixel where a pixel contains 11 x 33 subpixels. (c) Schematic of the cross-section of a single subpixel

The pre-structured substrate was composed of subpixels as illustrated in

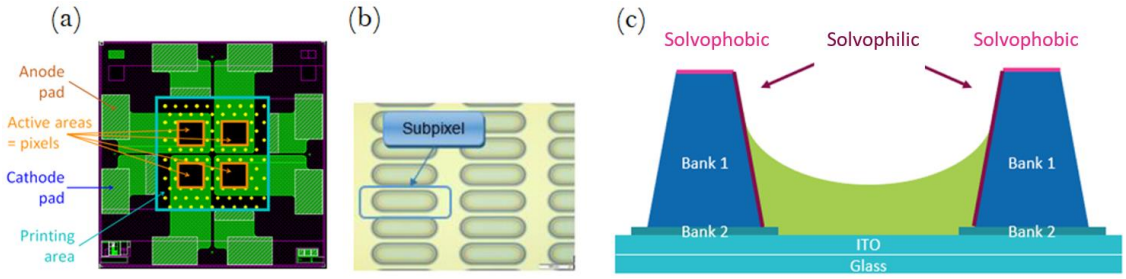

Figure 3.8c formed by bank materials on top of a 50 nm thick indium tin oxide (ITO) layer. Bank 1 was made of a solvophilic coating on the inner part and a solvophobic coating on the top. These coatings aim to concentrate the ink within the subpixel after printing. In contrast, bank 2, which was made of

insulating silicon dioxide, was used to increase the homogeneity of the layer thickness of printed OLEDs as will be explained in the next section.

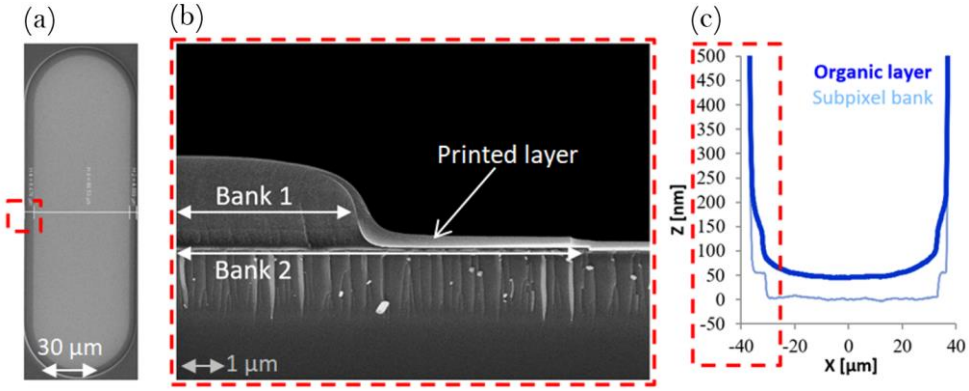

Figure 3.9: (a) Microscope picture of one subpixel. (b) SEM picture of bank 1 and bank 2 with one organic layer printed in subpixel. Picture taken from the side. (c) Film profile in subpixel measured by profilometer. The outer region of the subpixel is depicted by a red dashed box.

In the outer region of a subpixel emphasised by a red dashed box in Figure 3.9, it is often seen that the layer is not uniform due to adhesion on the bank material. Because of the insulating bank 2, no electrical current can be injected into the organic layers in the outer regions of the subpixel and thus only the flat and uniform layer in the centre of the subpixel contributes to light emission of the OLED device. The film formation inside a subpixel is presented in Chapter 6.1.2.

In addition to the pre-patterned substrates presented above, bare glass substrates of 30 mm x 30 mm were used for film stability tests against solvent exposure and for optical measurements of printed films, which were carried out on large area films.

3.2.3. Film formation process

Printing

The printing speed has a direct impact on the printing quality, i.e., the film homogeneity and the droplet landing precision. An increase in printing speed can lead to higher film homogeneity since the drying start with a shorter delay between the first and last printed droplet.[76] However, a maximum printing speed should not be exceeded; otherwise it could also result in a heterogeneous droplet spacing, thus a discontinuous printing resolution. With the Pixdro LP50 printer, a maximum of 250 $m \cdot s^{-1}$ printing speed is possible. Only one nozzle was used to jet the ink droplet and the printing was bi-directional. The printing speed was then adjusted to reach an intended droplet spacing according to Eq. 3.4.

$$v_{print} = DS \cdot f \tag{3.4}$$

where v_{print} is the printing speed in $m \cdot s^{-1}$, DS is the droplet spacing in metre and f is the printing frequency in s^{-1}. The droplet spacing was utilised to vary and tune the layer thickness. The printing time varied between 20 seconds to 100 seconds.

Drying

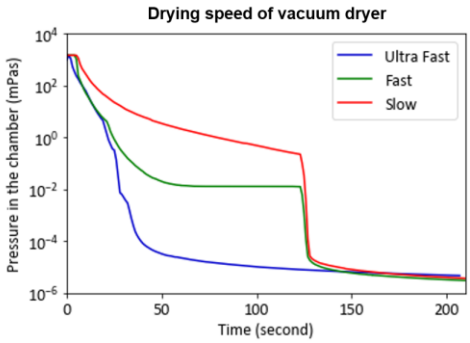

Figure 3.10: Pressure profiles with time in the vacuum chamber in dependence on the selected drying speed.

After printing the ink into the subpixels, the high boiling point solvent had to be removed prior to the thermal annealing step. The vacuum dryer was equipped with two different pumps in order to achieve a high vacuum of 10^{-5}-10^{-6} mbar at various speeds. The pressure profile in the chamber during the vacuum drying process was tuned by pump-down programs, as depicted in Figure 3.10. The drying conditions were adapted to the respective ink, since material-solvent mixtures behaved differently depending on their viscosity, vapour pressure, material-solvent interaction and affinity to the bank materials. The time to place the printing film under vacuum varied due to manual handling and it fluctuated between 15 seconds up to 5 minutes. This duration was not identified as having an influence on the film formation due to a fast ink levelling on the substrate.

Drying: Drying of large area films

In the beginning of the drying process, the evaporation rate of the solvent was the highest at the substrate edges and weaker in the centre. In Figure 3.11, the drying evolution of a large area printed film on a glass substrate can be seen. The drying does not start homogeneously over the layer due to disparate vapour pressure at the layer edges compared to the centre of the layer.

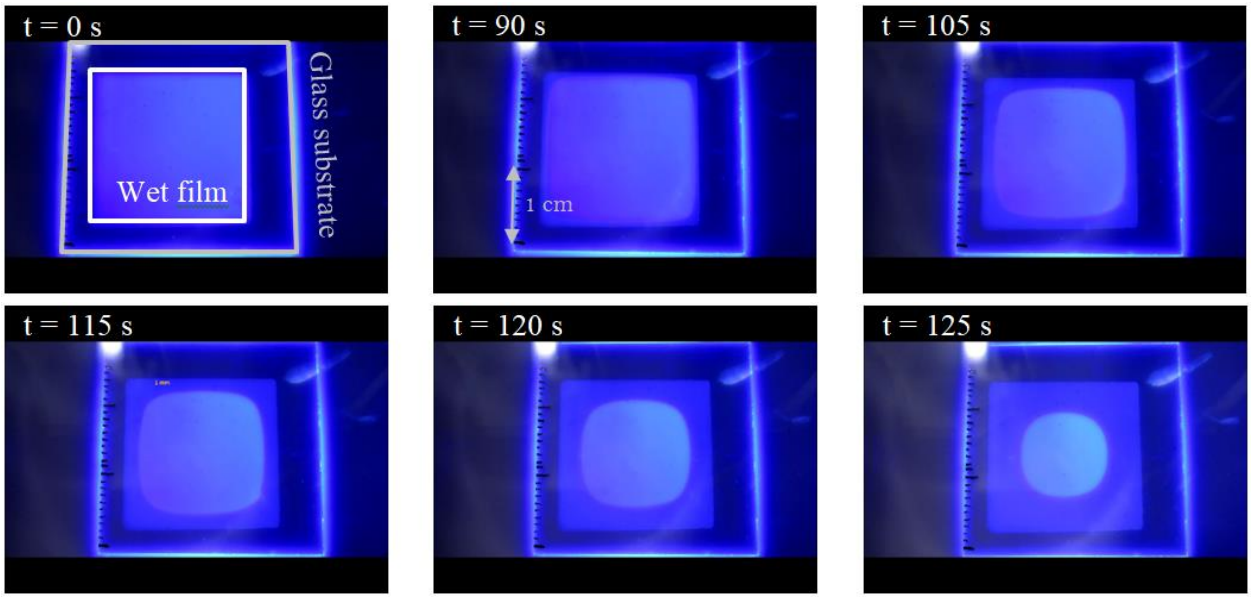

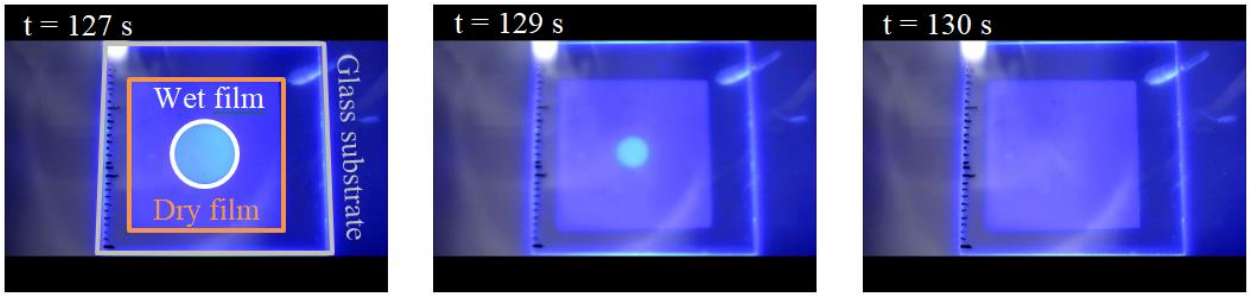

Figure 3.11: Photographs of a large area film during the drying process in the vacuum chamber taken by camera under UV illumination. An emissive material mixture was printed from menthyl isovalerate on glass substrate and dried with the slow drying speed program. For an easier identification at t = 0 s and t = 127 s, the substrate has been marked in grey, the wet film in white and the dry film in orange.

Drying: Drying in a patterned substrate with banks

In a patterned substrate, the solvent evaporation was more complex than for the large area films. After the ink level has dropped below the bank height, a capillary suction from the bank walls occurred due to the negative curvature of the drop. This negative curvature was caused by the droplet pinning at the top of the bank wall.[97] The dried film pinned on bank 1 and bank 2 as can be seen in Figure 3.9b. Due to the insulating material composing the banks, the part of the printed film pinned on the banks did not conduct charge carriers.

Annealing

After drying, the substrate was transferred to a N_2-filled glovebox where thermal annealing was performed on a hotplate. This thermal treatment was necessary to trigger the cross-linking reaction of the HIL and the HTL. For the EML, thermal treatment was also utilised to remove solvent residue from the layer. The substrate was placed on a hotplate, printing side up, at a fixed and stable temperature for various times depending on the layer. The HIL and HTL were annealed for 30 minutes at 225°C (the HTL annealing temperature was varied in the study) and the EML was treated for 10 minutes at 150°C.

3.2.4. Film thickness measurement

Film thickness determination was carried out on thin films after being inkjet printed, vacuum dried and annealed. The layer profile was measured by the profilometer Dektak 150 from Veeco Instruments Inc. utilising a diamond needle.

Large area films

To determine the thickness of large area printed films, the printed layer was scratched with a scalpel so that the cross-section was accessible to the measurement. Subsequently, the needle of the profilometer was moved perpendicular to this scratch and the deflection of the needle was recorded. The needle scanned a defined length and recorded points every 100 nm with a contact force of 5 mN. The precision of the thickness measurement was ±2 nm.

Pixelated substrates

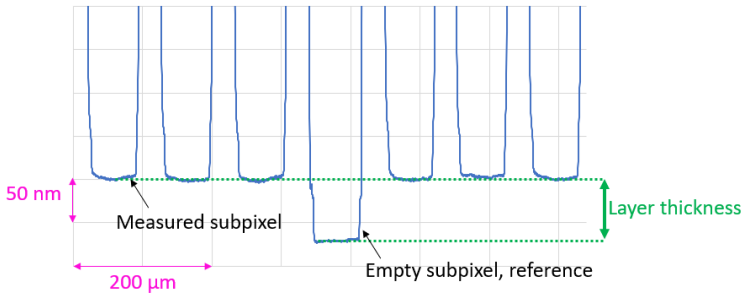

Figure 3.12: Example of a measurement scan to determine layer thickness over seven subpixels of a pixelated substrate.

The measurement of a printed layer within a pixelated substrate remains a challenge. Indeed, the small dimensions of the subpixels may request several trials to target the centre of the subpixel where the average layer thickness is taken. The thickness of a layer was determined by the relative difference between an empty subpixel as reference where no ink was deposited and the third subpixel away from the reference.[98] This printing pattern was especially employed for film thickness measurements. The first two subpixels could be influenced by the empty subpixel during drying due to different vapour pressure environments, thus they could have a different film thickness and film profile compared to a fully printed substrate without empty reference pixels. The needle scanned the measurement area consisting of seven subpixels. An example of a scan is shown in Figure 3.12.

3.2.5. Polymer bulk properties

A range of characterisation techniques was used in this work to describe the solvent impact on material properties. The hole transport material was characterised as powder, as film and as solution.

Cross-linking enthalpy

Differential Scanning Calorimetry (DSC) measurements of the polymer were performed under ambient atmosphere using TA Analysis model Discovery Serie 1. Powder samples (ca. 2 mg) were measured in standard aluminium crucibles with a closed lid. Sample thermograms from a single heating ramp were recorded from room temperature to 300°C under argon atmosphere with a gradient of 20 $K \cdot min^{-1}$.

Thermal stability

Thermogravimetric analysis (TGA) was performed to investigate the material stability against thermal stress by analysing the mass change of a sample as a function of temperature. The measurements were carried out using an instrument from TA analysis model Discovery Serie 1. Samples of 1- 4 mg were heated up from room temperature to 500 °C in inert crucibles at a constant heating rate of 20 $K \cdot min^{-1}$. The furnace was constantly flushed with nitrogen to avoid possible material oxidation by atmospheric oxygen. Mass loss of a sample usually occurs through physical processes

(evaporation, sublimation), chemical reactions (oxidation, reduction), or decomposition of the sample to form volatile fragments.

Infrared spectroscopy

The cross-linking reaction of styrene in polymer powders was evaluated with FT-IR by monitoring the reduction of the styrene signal after annealing. Infrared spectra were measured with a LUMOS FT-IR spectrometer from Brucker. The polymer powders were placed on silver-coated substrates and measured in reflection mode (ATR) with a germanium crystal detector. Before every measurement, the background noise was measured. Spectra were recorded at 4 cm^{-1} resolution and 60 scans were averaged to reduce the noise. Different pressing forces were tested and the level "hard" (setting of the instrument software) was used to measure the polymer powders.

3.2.6. Polymer film properties

The surface roughness and film homogeneity of the polymer films were measured as well as the surface energy. The cross-linking reaction in film was characterised by determining the cross-linking enthalpy by assessing the film stability against solvent exposure, and by evaluating the change in optical properties of the film.

Surface analysis vs. interferometry

Film surface information, such as roughness, layer homogeneity, but also thickness of thin films (< 1 µm), was investigated by an S neox 3D optical profiler from Sensofar Metrology. This non-contact optical 3D surface profiler provides a sub-nanometre vertical resolution. A Mirau objective with 10 x magnification was used to perform the measurements. The working principle of this interferometer is illustrated in Figure 3.13.

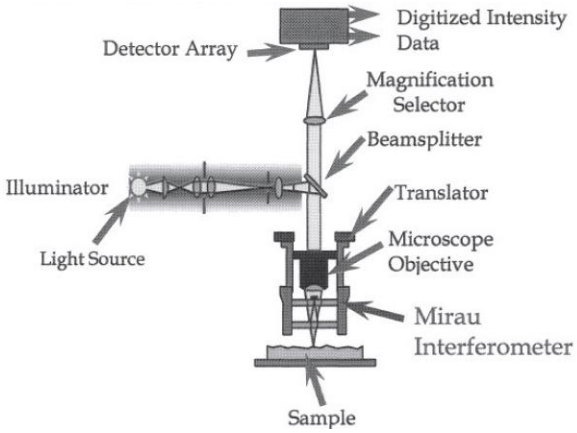

Figure 3.13: Schematic representation of a white light scanning microscopy. Reprinted from reference.[99]

The light source illuminates via a beam splitter the microscope objective and subsequently a Mirau interferometer and the sample. Interference patterns are created by superposition of the reflected light from the surface of the sample and the directly reflected light from the light source to the detector which is then picked up by a detector array consisting of a charge-coupled device (CCD) and a digital acquisition system. The surface profile is then calculated from the distortion of the interference pattern. Due to short coherence length of the light, a vertical scanning method is employed so that the focus

on various heights is possible for the same order of the light coherence length. Scanning the film layer by layer eliminates the short dynamic range problem and allows for a measure of the height profile.[99]

Surface energy

In order to study the surface energy of the polymer inks, contact angle measurements were performed with a drop of each ink on a glass substrate. The KRÜSS DSA100 permits to measure the contact angle defined as being the angle between the substrate and the tangent to the formed droplet, as illustrated in Figure 3.14.

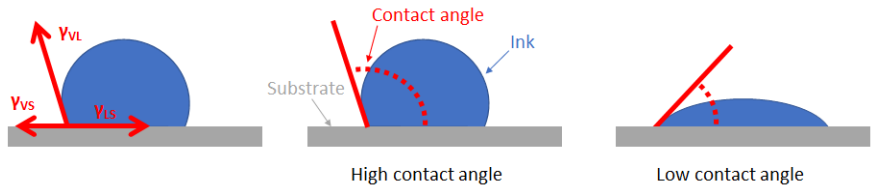

Figure 3.14: Schematic of contact angle measurement for different inks. γ_{VL}, γ_{VS} and γ_{LS} correspond to the surface energy at the liquid/vapor interface, at the vapour/solid interface and at the liquid/solid interface, respectively.

The contact angle is defined by the surface tension of the solvent and the substrate. It gives information about the wetting potential of an ink on a given substrate, as depicted in Figure 3.15. A sessile drop was deposited on a perfectly flat and homogeneous substrate and a high-speed zoom camera combined with an LED backlighting permitted a high-resolution imaging of the droplet wetting. The drop tends to minimise its surface free energy until the contact angle with the substrate achieves its equilibrium value.[100] The contact angle was taken at the equilibrium position and adjusted to a theoretically determined angle by using a circular fitting for contact angle lower than 20° and fitting the tangent of the droplet for higher contact angle.

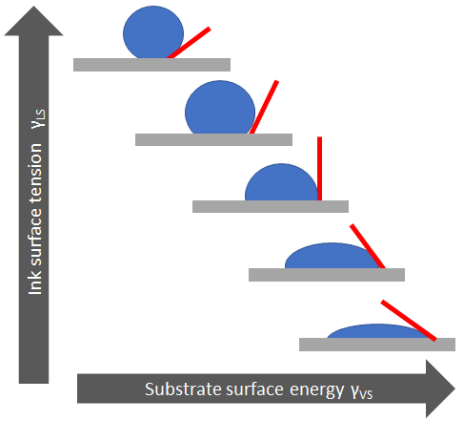

Figure 3.15: Contact angle-dependency on ink surface tension and substrate surface energy.

The contact angle of a droplet can be used to gain information about its drying behaviour, as depicted in Figure 3.16. Droplets of low contact angle lead to homogeneous distribution of the polymer particle on the surface. In opposite, droplets of high contact angle aggregate the polymer particles more in the centre. The contact angle of a droplet on a given substrate provides information on the resulting film formation since the drying process impacts the material distribution over the substrate. To obtain flat and homogeneous films, inks exhibiting low contact angles are preferred.

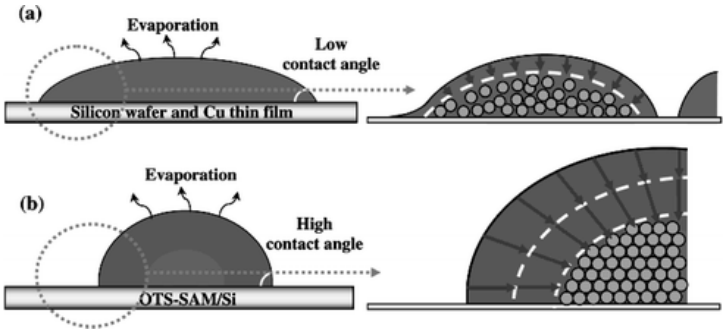

Figure 3.16: Impact of droplet contact angle on the particle arrangement in suspension. (a) Hydrophilic droplet leads to homogeneous repartition of the particle on the surface. (b) Hydrophobic droplet drives the particles to aggregate in the centre. Reprinted from reference.[66]

Cross-linking enthalpy in polymer film

In order to measure the cross-linking enthalpy of X-Po in films, DSC was performed under ambient atmosphere using an instrument from TA analysis model Discovery Serie 1. Polymer ink (ca. 30 µL of ink at 50 $g \cdot L^{-1}$) was dropped into standard aluminium crucibles. Then the crucibles were place for 3 hours under vacuum to remove most of the solvent. Prior to the measurement, the crucibles were closed with a lid. Thermograms were recorded from a single heating ramp starting at room temperature up to 300°C at a heating rate of 20 $K \cdot min^{-1}$.

Film stability against solvent exposure: Spin coated film

To determine the film stability against solvent exposure, rinsing tests were carried out on spin-coated films. A thin film was deposited on top of a glass substrate by spin-coating and subsequently cross-linked by heat treatment. Film thicknesses were measured before and after rinsing with an organic solvent, to remove non-cross-linked parts of the layer. The film stability against solvent exposure was defined as the ratio of thickness before and after solvent rinsing.

Film stability against solvent exposure: Inkjet printed film

To test the stability of an inkjet printed film against solvent exposure, a new method was developed where the deformation of the film surface due to solvent exposure is quantified. A square shaped large area layer was printed from each ink onto a glass substrate. The wet film was dried in a vacuum chamber and then annealed in a nitrogen atmosphere for 30 minutes at 225°C on a hotplate to activate the cross-linking reaction. To test the solvent exposure stability of the polymer thin film, a 90 pL drop of 3-phenoxytoluene was dropped on the centre of the layer since it is also the solvent used to process the EML. After five minutes soaking, the drop of 3-phenoxytoluene was removed by vacuum drying. The film deformation was recorded by interferometry and the cross-section of the deformation was analysed, see Figure 3.17.

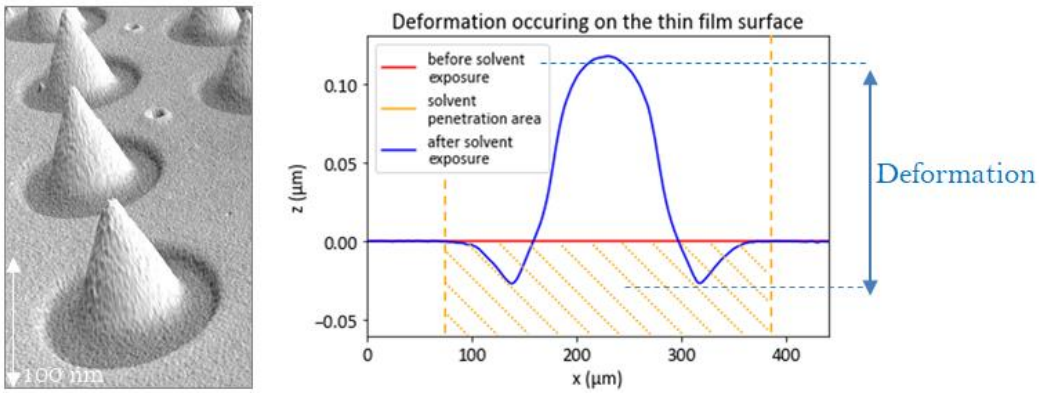

Figure 3.17: Deformation of X-Po polymer surface processed from 1-methylnaphalene observed by interferometry (left). A 90 pL drop of 3-phenoxytoluene was left on the polymer surface for five minutes and removed by vacuum drying. Cross-section of the deformation used to quantify the solvent exposure stability (right).

Optical properties

In this work, optical properties of X-Po thin films were measured by ellipsometry to study the impact of ink solvent on film properties. Ellipsometry is an optical technique used to determine film thickness and optical constants (n, k) of the small molecule(s) and polymer(s) contained in the film. It measures the change in polarisation of light after being reflected (/transmitted) on (/through) a sample. Light polarisation is characterised by an amplitude Ψ and a phase Δ. The working principle of an ellipsometer is shown in Figure 3.18a. An isotropic light source shines through a polarising filter to generate linear polarised light which is reflected or travels through the sample. Linear polarised light is used since its amplitude and phase are defined. By the reflection or transmission of the polarised light, Ψ and Δ change and are functions of film thickness and optical constants of the investigated material. The refractive index n (index of refraction) describes the ratio of the light velocity c in vacuum and to the light velocity in matter, in the present case in the investigated material (refraction), as $v = c * n^{-1}$. The extinction coefficient k describes the reduction of amplitude due to the light interaction with the material (absorption).

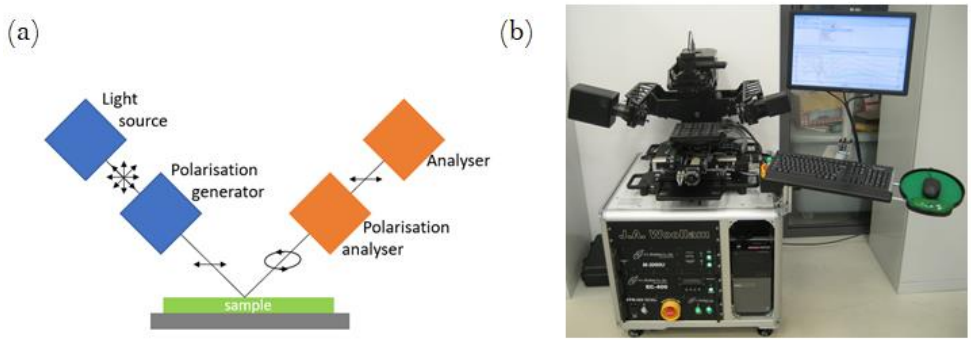

Figure 3.18: (a) Working principle of an ellipsometer. (b) Ellipsometer M-2000 from J.A. Woollam used to measure thin film optical properties.

Ψ and Δ of printed films were measured with the ellipsometer M-2000 from J.A. Woollam, see Figure 3.18b. The absorption spectra of inkjet printed thin films were recorded for each film in reflection and in transmission over a broad range of wavelengths, from 250 nm to 1000 nm. Three measurements

were performed in reflection mode at various angles around the Brewster's angle, which were set at 65°,70°,75° measured from sample normal. Also known as the polarisation angle, the Brewster's angle corresponds to the incidence angle where an isotropic light separates into a vertical polarised light going through a surface and a horizontal polarised light reflected making an angle of 90° with the transmitted light. Measuring a sample around the Brewster angle is most sensitive to absorption.

After measurement, a model was fitted to the measured data. A perfect match was not possible in practise.[101] The Mean-Square-Error (MSE) quantifies the difference between the model and the measured data for each (Ψ, Δ) pair. The MSE is the sum of the square the difference between the measured and calculated data on each measured data point, so noisy points are weighted less heavily The Levenberg-Marquardt algorithm is employed to determine the best fit to the measured data which corresponds to the lowest MSE.[102] A good fit of n and k is characterised by a low MSE. Figure 3.19 shows the importance of the layer thickness to reach a good fit. The thickness dependence of the MSE should be investigated for the Levenberg-Marquardt algorithm to find the best fit.

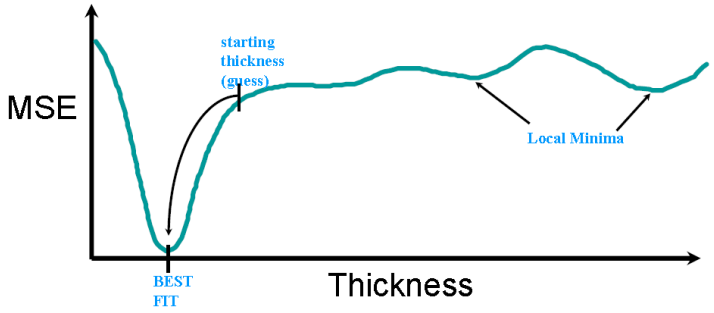

Figure 3.19: Graphical representation of the MSE depending on the layer thickness. Reproduced from www.jawoollam.com.

3.3. Electronic device

Electronics devices were built either having unipolar or bipolar transport. Both devices were essential to characterise the electronic properties of the deposited organic semiconductors and to understand the working mechanism of the OLED multilayer stack. The two different device types were processed on a pixelated patterned substrate, introduced in Chapter 3.2.2. A schematic representation of the 30x30 mm² substrate is shown in Figure 3.20.

Before device fabrication, each substrate was cleaned under ultrasonic distilled water, then dried by a nitrogen air flow and heated at 230°C for two hours. This treatment was required to increase the work function of ITO from 4.8 eV to 5.3 eV. By this treatment, the energy barrier between ITO and HIL was minimised. The printed organic layers as well as the evaporated layers, except for the cathode, were deposited in the grey region partially covering the ITO anodes (light blue in Fig. 3.20). Finally, the aluminium cathode, depicted in dark blue, was evaporated with a different shadow mask so that the 4.606 mm² active areas (yellow) were formed by the overlap of the two electrodes. To avoid the negative influence of oxygen and moisture, the OLED devices were encapsulated in a N_2-glovebox using a cover glass.

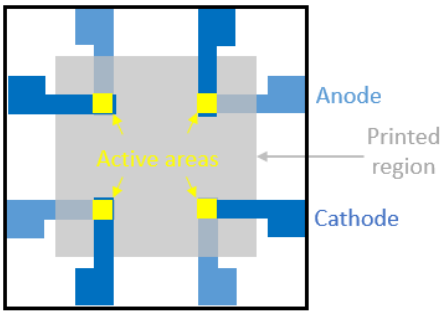

Figure 3.20: Schematic representation of a device built for electronics characterisation. Four active areas (yellow) are formed by the overlapping anodes (light blue) and cathodes (dark blue). The area in grey depicts the region where the printed as well as evaporated layers are deposited.

3.3.1. Carrier mobility in hole transport layer

The mobility is an important parameter to characterise the transport properties of organic thin films. The mobility can be measured by the so called Time of Flight (TOF) technique. However, this technique requires film thickness of about 2-8 µm. Since soluble films are commonly between 10 nm and 200 nm thick, this technique cannot be deployed. On the other hand carrier mobility can be extracted from organic field-effect transistors (OFET) measurements. Nevertheless, the OFET configuration determines the carrier mobility along the substrate direction. Thus this measurement technique is meaningful only for film with anisotropic carrier mobilities.[103] A third technique to determine the mobility is the space-charge-limited current (SCLC) technique which is well established to investigate the carrier mobility of organic thin films. The typical SCLC behaviour for polymer semiconductors is represented in Figure 3.21. To calculate the mobility of X-Po, unipolar devices were built insuring a good Ohmic contact between the organic layer and the injecting metal electrode.

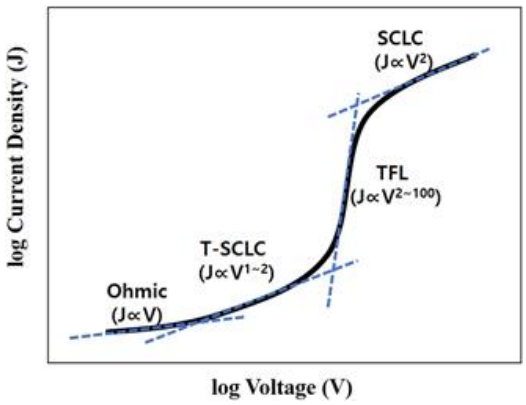

Figure 3.21: Typical space charge–limited current behaviour for polymer semiconductor. Four charge-transport regions are visible (i) Ohmic region ($J \propto V$), (ii) trap-SCLC region ($J \propto V^{1-2}$), (iii) TFL region ($J \propto V^{2-100}$), and (iv) SCLC region ($J \propto V^2$). Reprinted from reference.[104]

Unipolar devices can be fabricated by inserting the organic layer under investigation between two suited electrodes. The organic layers can be composed of a single or a mixture of material(s). Two organic layers can also be studied if they ensure a single carrier transport. In unipolar devices, recombination is absent, since only one carrier type is present.[105] Measurement of unipolar devices provide information on charge transport in an organic layer. It is obtained from a single steady-state current–voltage measurement from the device. At low current density, the current is mainly carried by thermal equilibrium charge carrier density. It is described by the Ohmic regime and a linear dependency of the current density J with voltage V. The conductivity σ is described as:

$$\sigma = en\mu \tag{3.5}$$

where e is elementary electric charge, n is the thermally induced charge carrier concentration and μ is the charge carrier mobility.[106] The carrier mobility can be determined in the space-charge-limited current (SCLC) regime reached normally at a considerably higher bias voltage than the built-in voltage. In the SCLC regime, holes are injected and the current is dominated by drift. The current becomes limited by the electric field of the injected charges at the entrance electrode, leading to a space-charge-limited current. The electric field drives towards the collecting contact. Such SCLC current is described by the Mott-Gurney equation for the J-V characteristic for trap-free transport:

$$J = \frac{9}{8}\varepsilon\mu\frac{V^2}{L^3} \tag{3.6}$$

where ε is the permittivity of the semiconductor, L is the layer thickness, μ is the charge carrier mobility, and V is the applied voltage. A large advantage of such an analytical description is that from experimental data on single-carrier devices, the charge carrier mobility can directly be obtained from current density versus voltage (J–V) measurements presuming that the dielectric constant is known and that the current exhibits a quadratic dependence on the applied voltage.

In the present thesis unipolar devices were used to limit the presence to only one charge carrier type. In this work, hole only devices were fabricated by choosing suitable electrodes and semiconductor materials so that no electrons could be injected from the cathode in the investigated voltage range. To study the impact of the degree of cross-linking of the HTL on the hole transport properties, HIL and HTL were deposited between the two electrodes as represented schematically in Figure 3.22. An aluminium cathode was deposited, its LUMO level being much higher than the one of the adjacent HTL, ensuring unipolar charge transport. Such device allowed for a simplified interpretation of the current-voltage characteristics according to the Mott- Gurney Law for space-charge-limited currents.[107] Based on this, the conductivity as well as the charge mobility could be determined. Due to the low intrinsic carrier density and the mobility-inhibiting hopping transport, organic semiconductors usually have a low mobility.

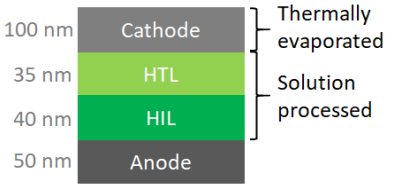

Figure 3.22: Multilayer stack of a unipolar device designed to study the mobility of the HTL.

3.3.2. Bipolar devices

As introduced in Chapter 2.1, multilayer stacks are preferred in order to have efficient and long-lasting OLED devices. The architecture of the OLEDs studied in this work is shown in Figure 3.23 and due to the use of a pre-patterned 50 nm thick ITO layer as anode it was a bottom-emission OLED. The device efficiency was strongly dependent on the distance between the emissive layer and the reflective cathode due to a weak cavity effect.[108]

On top of the ITO five organic layers were deposited subsequently in a controlled process. HIL, HTL and EML were processed from solution by inkjet printing the corresponding inks onto the pixelated substrate as shown in

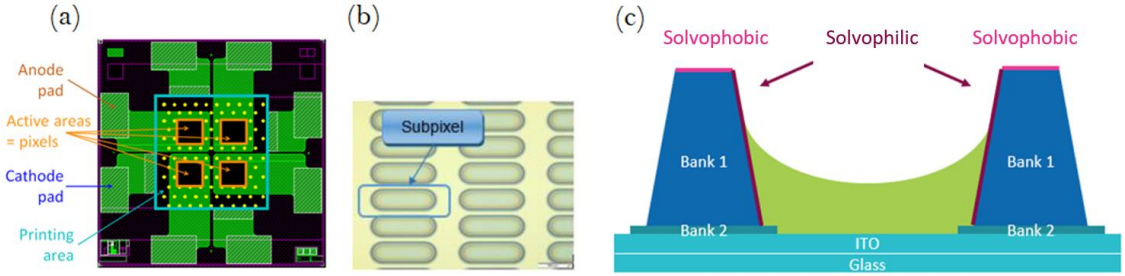

Figure 3.8. The solution deposition took place in an inert atmosphere of nitrogen. Afterwards the layers were dried under high vacuum of 10^{-5}-10^{-6} mbar as described in Chapter 3.2.3. Then, the layers were annealed in an inert atmosphere of nitrogen. The HIL and EML were annealed at 225°C and 160°C, respectively. The annealing temperature of the HTL was varied and will be mentioned for each investigation. In the case of cross-linkable polymers, the annealing enabled the solvent drying and polymer cross-linking reaction. These steps were repeated for each printed layer. Then ETL and EIL were deposited by PVD from aluminium oxide crucibles at a low pressure of 10^{-7} mbar with an evaporation rate of approximately 1-10 Å·s^{-1}. Finally, 100 nm of aluminium was evaporated as cathode.

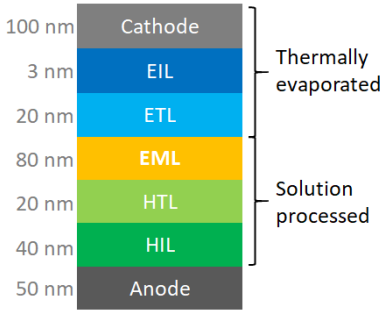

Figure 3.23: Bipolar device architecture employed to study the interface between the solution-processed layers HTL and EML by varying the cross-linking degree of the HTL.

From those bipolar devices current-voltage characteristics, luminous efficiency, electroluminescence colour and lifetime were determined. However, the analysis of current-voltage characteristics of bipolar device was not trivial due to energy barriers at each interface that affect the charge transport properties. The characterisation of OLED performance is explained in the following section.

3.3.3. Characterisation of OLED devices

In this section, the electrical and optical characterisation of OLED devices is introduced. Current-voltage characteristics were recorded on both types of devices. Luminous efficiency, electroluminescence colour and lifetime were measured for bipolar devices only. Each measurement was performed on eight identical pixels from two substrates, from which the median value is presented in this work. Defects, short-circuited or miss-printed pixels were treated as statistical outliers. Each pixel was composed of 33 x 11 subpixels, as introduced in Chapter 3.2.2. Therefore, the performance of a single pixel was calculated as the average performance of all 363 subpixels.

Current-voltage characteristics

Current-voltage characteristics were measured by a custom-made system consisting of spring contact between the anode and the cathode. A voltage ramp from 0 V to -8 V as well as the reverse ramp were

applied by a Keithley 2400 SourceMeter. Simultaneously, the current of each pixel was measured by a Keithley 2700 MultiMeter in the dark. The maximum voltage was chosen such that the maximum current density did not exceed 100 mA·cm^{-2}. In the case of hole-only devices, the measurements were recorded for voltages from 0 to 2 V in steps of 20 mV, afterwards steps of 0.2 V were applied until a current density of 100 mA·cm^{-2} was reached. In the low current density range, each measurement point was averaged over a period of 200 milliseconds to ensure that the current measurements were able to reach a steady-state. The current I through the device was measured and the current density j was calculated by the relationship:

$$j = \frac{I}{A} \tag{3.7}$$

where j is recorded in mA·cm^{-2}, I is the current in mA and A is the active luminous area with A = 4.606 mm^2.

Luminous efficiency

Simultaneously to the I-V characteristic, the incident photon flux was measured by a calibrated photodiode connected to a Keithley 6485 Picoamperemeter. In order to convert the measured photon flux into luminance in cd·m^{-2}, the photodiode was calibrated by the photometer LMT L1009 of LichtMessTechnik GmbH in combination with a V(λ) filter. The photopic luminous function V(λ) represents the light sensitivity curve of the human eye within the photopic wavelength range. The luminous efficiency η_L of OLED devices (units cd·A^{-1}) is determined as the ratio of the luminance L (units cd·m^{-2}) and the current density j (units mA·cm^{-2}), as followed:

$$\eta_L = \frac{L}{j} \tag{3.8}$$

Another method to quantify the efficiency of OLEDs is the external quantum efficiency (EQE, η_{ext}). The EQE is defined as the ratio of the extracted photons to the number of majority charge carriers injected, as described by:

$$\eta_{ext} = \eta_f \cdot \gamma_{e-h} \cdot \chi_{s/t} \cdot \varphi_{opt}. \tag{3.9}$$

Here, η_f is the yield of radiative decay from singlet excitons, γ_{e-h} is the charge carrier balance between injected holes and electrons in the EML (should be ideally 1), $\chi_{s/t}$ is the fraction of generated excitons which can decay radiatively (0.25 in fluorescence, 1 in phosphorescence) and φ_{opt} is the outcoupling efficiency defined by the ratio of light emitted at the surface to the light produced in the bulk of the device (estimated to 20%). However, directly measuring the number of photons emitted from a device is challenging. Therefore, commonly the EQE is determined from the I-V-L characteristics and the electroluminescence spectrum.

Electroluminescence

The colour of the emitted light from the OLED pixels was characterised using an Ocean Optic USB4000 fibre optic spectrometer. The emission spectra were recorded at a luminance of 1000 cd·m^{-2}

over a wavelength range from 190 nm to 1100 nm. From the electroluminescence spectrum, the CIE (x;y) coordinates (Commission Internationale de l'Éclairage) were calculated. The x and y coordinates were plotted in a chromaticity diagram, as shown in Figure 3.24. The curved edges of this diagram correspond to monochromatic light. In addition to the electroluminescence spectrum, microscope images of OLED pixels and subpixels were taken at a luminance of 1000 cd·m^{-2}. These images were used to determine the light emission homogeneity intra- and inter-subpixels.

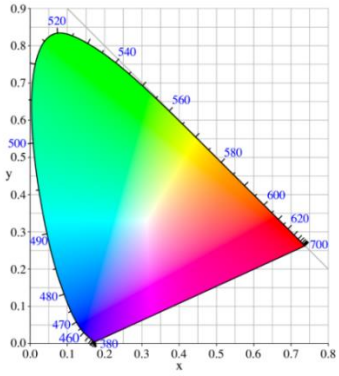

Figure 3.24: Chromaticity diagram displaying the CIE coordinate system.

Device lifetime

OLED device lifetime is defined as the time it takes for the luminance to decrease to a certain fraction of the initial luminance while being driven at constant current. For example, LT95 corresponds to the duration required for the device to reach 95% of its starting luminance. In this work, the OLED devices were driven at the current density required for a luminance of 8000 cd·m^{-2}.

For typical display applications, a luminance of 200-500 cd·m^{-2} is required. Since OLED materials can achieve lifetimes of a few years at these luminance levels, accelerated lifetime testing by using a high initial luminance have to be performed. The OLED lifetime was extrapolated from the measured lifetime using the following formula:

$$LT = LT_{measured}\left(\frac{L_0}{L}\right)^{AF} \tag{3.10}$$

where L_0 is the initial luminance, L is the extrapolated luminance at which the device lifetime was supposed to be determined, $LT_{measured}$ is the lifetime measured at L_0, and AF is the acceleration factor that is determined for each colour.

The lifetime is a critical parameter for OLED devices. It can be influenced by the material properties, by the device stack and by the fabrication process. At the beginning of operation, the OLED device undergoes severe degradations leading to a fast decline of the luminescence within the first minutes up to hours. Therefore, in this work, the luminance measured by a photodiode, was recorded every thirty seconds during the first hour of operation, in order to achieve a high measurement resolution. Then an interval of 6 minutes between every measurement was kept until two hours of operation. Subsequently, the time interval was expanded to thirty minutes and then one hour after ten hours.

4. Characterisation of polymer solutions based on experimental and empirical descriptions

Polymer solutions, as well as other fluids, do not always follow Newton's law of viscosity, as introduced in Chapter 3.1.4. Newton's law states that the ratio between the shear stress and the shear rate is constant under fixed temperature and pressure, and is defined as:

$$\sigma = \eta \cdot \dot{\gamma} \tag{4.1}$$

where σ is the shear stress in mPa, η is the viscosity in mPa·s and $\dot{\gamma}$ is the shear rate in s^{-1}. A Newtonian fluid exhibits a linear dependence of the shear stress with respect to the shear rate, i.e., a constant viscosity. On the opposite, a non-Newtonian fluid shows a dependency of the viscosity on the shear rate. An increase of viscosity with shear rate is referred as shear thickening. Shear thinning concerns a decrease of viscosity with shear rate, see Figure 3.5.

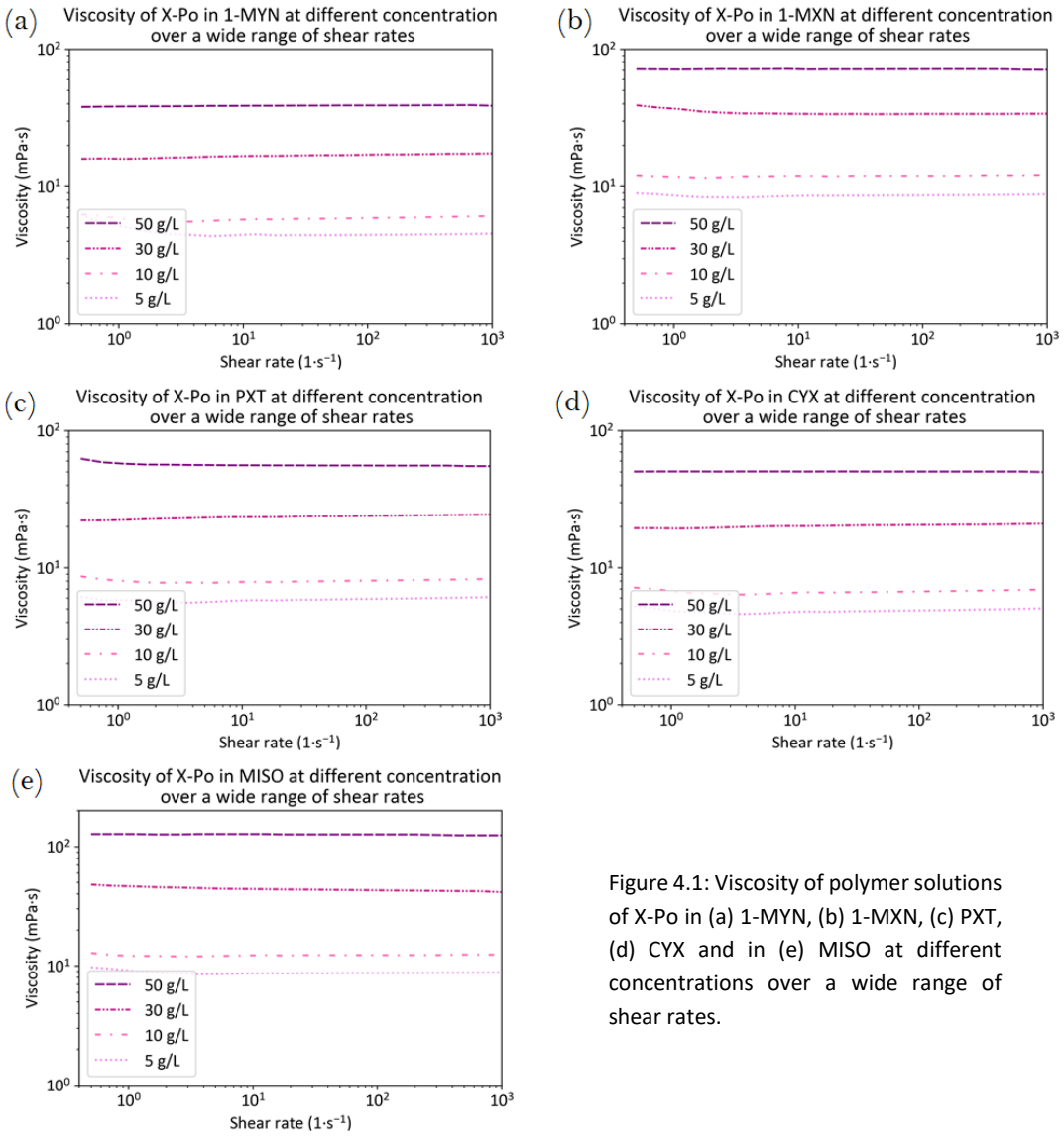

Figure 4.1: Viscosity of polymer solutions of X-Po in (a) 1-MYN, (b) 1-MXN, (c) PXT, (d) CYX and in (e) MISO at different concentrations over a wide range of shear rates.

Newtonian and non-Newtonian fluids respond to different laws and cannot be characterised by the same models. In order to identify the properties of polymer X-Po solutions, numerous viscosity measurements have been carried out. Polymer X-Po was dissolved in 1-methylnaphthalene, 1-methoxynaphthalene, 3-phenoxytoluene, cyclohexyl hexanoate and in menthyl isovalerate at the concentrations of 5 $g \cdot L^{-1}$, 10 $g \cdot L^{-1}$, 30 $g \cdot L^{-1}$ and 50 $g \cdot L^{-1}$. The viscosity dependency on the shear rate is plotted to identify whether the solutions follow the Newton's viscosity law, and if not, from which concentration the behaviour deviates from the Newtonian viscosity, see Figure 4.1.

For all polymer solutions at all tested concentrations, the viscosities are constant over a wide range of shear rates from 0.5 s^{-1} to 1000 s^{-1}. It is concluded that the polymer solutions of X-Po in 1-methylnaphthalene, 1-methoxynaphthalene, 3-phenoxytoluene, cyclohexyl hexanoate and in menthyl isovalerate at the concentration of 5 $g \cdot L^{-1}$, 10 $g \cdot L^{-1}$, 30 $g \cdot L^{-1}$ and 50 $g \cdot L^{-1}$ are all following Newton's law of viscosity.

In this chapter, the affinity of X-Po polymer with the processing solvent is characterised by experimental measurements as well as empirical descriptions such as the Mark-Houwink parameters, the Huggins and Kramer constants, and the Solomon Ciuta equation.

4.1. Polymer-solvent affinity

The affinity between a polymer and a solvent characterises the interaction occurring between the polymer chains and the solvent molecules. The polymer-solvent interaction directly impacts the size and conformation of a polymer chain in solution, defined by its hydrodynamic volume. A solvent exhibiting a low interaction with a polymer leads to enhanced intramolecular interactions resulting in a decrease of the hydrodynamic volume, i.e., a smaller radius of gyration R_g.[109] This solvent is called a *bad* or *poor* solvent for the given polymer: the polymer chains tend to minimise their interaction with the solvent molecules. A "theta" solvent corresponds to an intermediate state where the polymer acts like ideal chains, presuming a random coil conformation. When polymer chains expand and tend to maximise their contact with the solvent molecules, the solvent is called *good*.

4.1.1. Experimental determination of polymer-solvent affinity

Solubility of a polymer in a solvent describes the ability of the solute to favourably interact with the solvent. It depends on the polymer and solvent properties, as well as environmental factors like temperature and pressure. The Hildebrand-Scott equation presents the relationship between the polymer solubility and the polymer-solvent interaction.[110] The Hildebrand-Scott equation will not be discussed in details in this work. It simply states that the polymer-solvent interaction is directly proportional to the Hildebrand solubility parameters of the polymer and the solvent. So, solubility of a polymer in a solvent is a parameter that can be used to investigate the interaction between polymer and solvent.[111]

Practically, the maximum solubility is described by the saturation concentration of a material in a solvent. Starting from saturation concentration and adding more material triggers precipitation of the excess of material. The solubility of X-Po was measured in 1-methylnaphthalene, 1-methoxynaphthalene, 3-phenoxytoluene, cyclohexyl hexanoate and in menthyl isovalerate. However,

after reaching a concentration of 300 g·L^{-1}, polymer gels were obtained for all polymer solutions. The very high viscosity of gel dramatically slows down the dissolution time. The solubility of X-Po in the five tested solvents was found to be higher than 300 g·L^{-1}. Therefore another technique had to be employed to define the polymer-solvent interaction.

Polymer-solvent affinity was determined using the NIPS method presented in Chapter 2.3.1.[87] Ethanol is considered to be a very *poor* solvent for X-Po since it can barely dissolve the polymer powder. Therefore, ethanol was used to precipitate the polymer from solution in each solvent of the study. Beginning of precipitation was determined visually and defined as the amount of added ethanol necessary to observe the first signs of turbidity, see Figure 4.2. When the solution turns turbid, the cloud-point is reached. The cloud-point can be detected by the naked eye or by a change of light intensity transmitted through the solution. This method is also called precipitation test in this thesis.

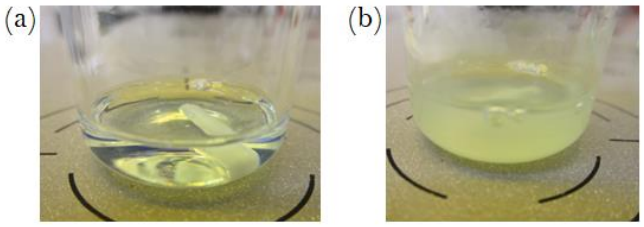

Figure 4.2: Photographs of precipitation test. (a) Polymer solution dissolved in cyclohexyl hexanoate at 30 g·L^{-1}; (b) precipitated solution after adding 21 v/v% ethanol.

The more ethanol needed to start the precipitation of the polymer solution, the stronger the interaction between polymer and solvent can be assumed. Such a strong interaction is characteristic of a *good* solvent[92] for X-Po. Solvent 1-methylnaphthalene was found to be the best solvent for polymer X-Po and menthyl isovalerate the worst, see Figure 4.3. The precipitation test was repeated with another solvent, namely acetone, considered to be a very *poor* solvent for X-Po. Results of these experiments confirm the experience made with ethanol.

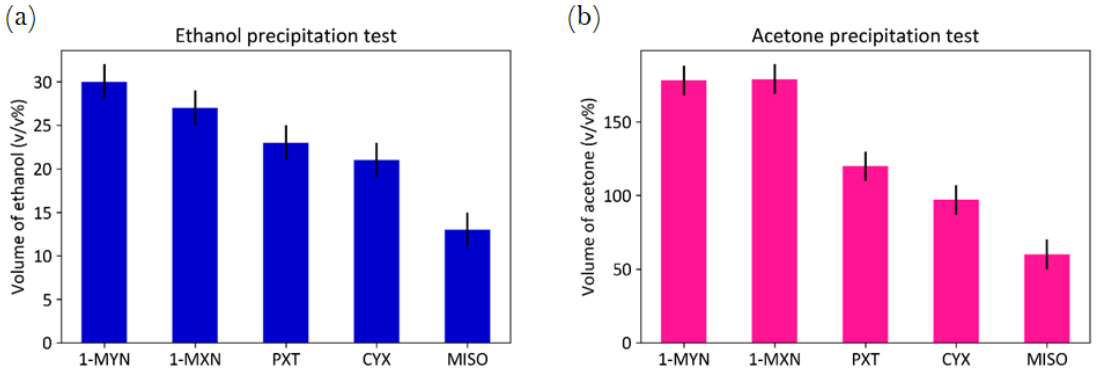

Figure 4.3: Experimental determination of polymer-solvent affinity. Precipitation test performed with (a) ethanol and (b) acetone as non-solvents dropped into X-Po polymer solution from 1-MYN, 1-MXN, PXT, CYX and in MISO.

For the tested polymer solutions, the naked eye detection was sensitive enough to differentiate the polymer-solvent interaction between different solvents. The cloud-point method is a reliable and reproducible technique to relatively judge the polymer-solvent interaction in different solutions. It is also a fast and material saving approach. The polymer X-Po adopts its most expanded conformation

in 1-methylnaphthalene. X-Po minimises its interaction more and more as it is dissolved in 1-methoxynaphthalene, in 3-phenoxytoluene, in cyclohexyl hexanoate and in menthyl isovalerate where it assumes a more collapsed conformation.

4.1.2. Empirical observations

There exist numerous empirical descriptions to calculate polymer-solvent interactions. Most of them describe the interactions in solution in a dilute regime, whereas a few solutions in the semi-dilute regime. Therefore, it is crucial to characterise the limit of each regime for each investigated solution to apply the corresponding empirical observation. At low concentrations, the polymer spheres are separated from each other by solvent molecules. As the polymer concentration in the solution increases, the polymer spheres get congested and start to touch each other. When the volume of the solution is packed with polymer spheres, the overlap concentration c* is reached.

Figure 4.4 represents three regimes of polymer solution concentration. When c is below c*, the polymer chain interacts mostly only with the solvent molecules; the solution is called dilute. The polymer chains are entangled when c is above c*, it is a concentrated solution. In this regime, the mobility of the chains is reduced, and the chains interact with each other.

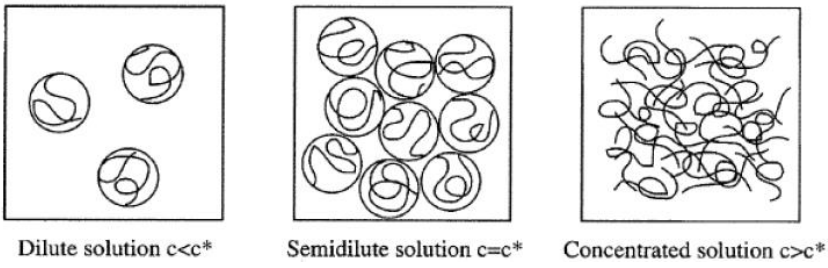

Figure 4.4: Concentration regimes for polymer solutions: dilute solution c<c*, solution at the overlap concentration c=c*, concentrated solution c>c*.

To determine the dilute and concentrated regime, Fedor introduced a relationship between the overlap concentration and intrinsic viscosity of the polymer solution, as follows:[112]

$$c^* = \frac{1.2}{[\eta]} \tag{4.2}$$

where c^* is the overlap concentration in g·dL^{-1} and $[\eta]$ is the intrinsic viscosity of the polymer solution in dL·g^{-1}.

The polymer X-Po can be dissolved in 1-methylnaphthalene, 1-methoxynaphthalene, 3-phenoxytoluene, cyclohexyl hexanoate and in menthyl isovalerate up to ~13 g·L^{-1} and remains in the dilute regime, as presented in Table 4.1. In the following section, all polymer solutions are in the dilute regime so that the various methodological investigations of polymer-solvent interactions can be performed. A dilute solution is required to neglect polymer-polymer interactions that start to occur when c > c*.

Solvent used in the polymer solution	Overlap concentration c* ($g \cdot L^{-1}$)
1-MYN	13.7
1-MXN	16.5
PXT	15.7
CYX	16.3
MISO	14.7

Table 4.1: Determination of the overlap concentration c*, determining the upper limit of the dilute regime of X-Po polymer solution from different solvents.

Mark-Houwink parameters: α and k

The Mark-Houwink parameters α and k are used to characterise the polymer-solvent affinity. The value of α is representative for the solvent affinity with a material. As introduced in Chapter 2.3.3, a strong interaction between the polymer and the solvent qualifies the solvent as *good*. Inversely, a weak interaction between the polymer and the solvent entitles the solvent as *poor*.

The empirical description claims that a *poor* solvent has α value of 0 to 0.5, where $\alpha = 0.5$ is called theta point. A *good* solvent exhibits α value between 0.5 and 0.8. Above 0.8, α corresponds to a semi-flexible to highly extended chain model, as represented in Figure 4.5.

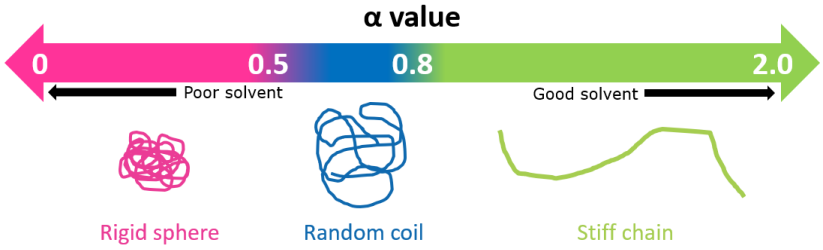

Figure 4.5: Mark-Houwink parameter α related to polymer organisation in solution.

To determine α, rheology measurements were performed. It was shown in Chapter 2.3.3 that the intrinsic viscosity of a solution $[\eta]$ is determined by:

$$[\eta] = k \cdot {M_w}^{\alpha} \tag{4.3}$$

$$\ln[\eta] = \ln k + \boldsymbol{\alpha} \ln M_w \tag{4.4}$$

where M_w is the polymer molecular weight, k and α are the MH (Mark-Houwink) parameters. These constants can be experimentally determined by calculating the intrinsic viscosity of several polymer solutions from different molecular weight which has to be figured out by an independent method. The molecular weight of X-Po was computed by gel permeation chromatography (GPC). Plotting $\ln[\eta]$ versus $\ln[M_w]$ usually gives a linear dependence, whose slope is α and the y-intercept is $\ln[k]$, as represented in Figure 4.6.

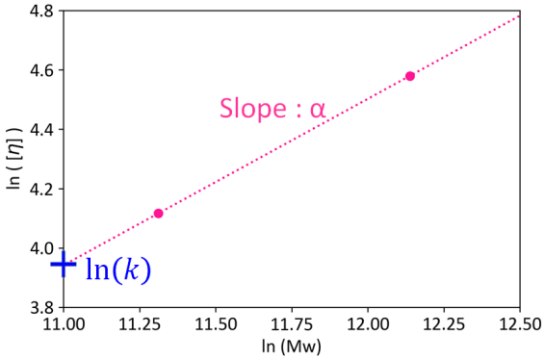

Figure 4.6: Graphical determination of Mark-Houwink parameters α and k for X-Po in CYX. The molecular weights of 81.800 g·mol^{-1} and 187.000 g·mol^{-1} were used to determine α and k.

The intrinsic viscosity $[\eta]$ represents the increase of viscosity by the individual polymer chains and can be determined only in dilute polymer solutions. It is defined as:

$$[\eta] = \lim_{c \to 0} \frac{\eta_{sp}}{c} \tag{4.5}$$

where c is the polymer concentration in the solution and η_{sp} is the specific viscosity described by:

$$\eta_{sp} = \frac{\eta_{solution}}{\eta_{solvent}} - 1 \tag{4.6}$$

Plotting the calculated specific viscosity of various polymer solutions versus their concentration usually gives a linear dependence and the extrapolation to the y-intercept is the intrinsic viscosity of the polymer solution, as illustrated in Figure 4.7.

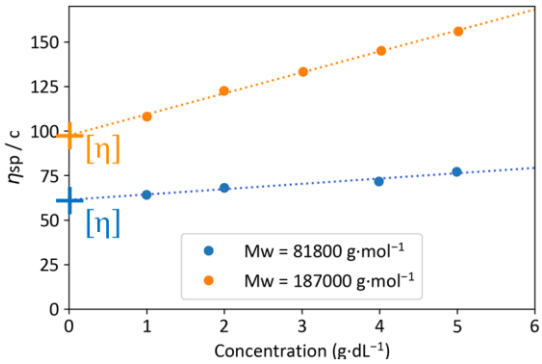

Figure 4.7: Graphical determination of the intrinsic viscosity [η] of X-Po in CYX. The molecular weights of 81.800 g·mol^{-1} and 187.000 g·mol^{-1} were used to determine [η].

Specific viscosities of X-Po solutions were determined for polymer molecular weights of 81.800 g·mol^{-1} and 187.000 g·mol^{-1} dissolved in 1-methylnaphthalene, 1-methoxynaphthalene, 3-phenoxytoluene, cyclohexyl hexanoate and in menthyl isovalerate at the following concentrations: 1 g·L^{-1}, 2 g·L^{-1}, 3 g·L^{-1}, 4 g·L^{-1}, and 5 g·L^{-1}. Viscosity of each solution was measured at 25°C. The obtained intrinsic viscosities of each polymer solution, as well as the Mark-Houwink parameters α and k are displayed in Table 4.2.

Table 4.2: Mark-Houwink parameters and intrinsic viscosities of X-Po solutions from 1-MYN, 1-MXN, PXT, CYX and in MISO.

	$[\eta]$ in L·g^{-1}	α	k
1-MYN	0.73	0.54	0.15
1-MXN	0.61	0.87	0.00
PXT	0.64	0.75	0.06
CYX	0.61	0.58	0.06
MISO	0.68	0.74	0.07

Uncertainties have to be considered in the values in Table 4.2, due to experimental errors and graphical fitting. For example, X-Po has a polydispersity index of 2.6, and the viscosity exhibits a 4% measurement error. Therefore, applying this uncertainty to α, a wide spread of values is obtained, as shown in Figure 4.8. It turns out that X-Po has a random coil conformation in all solvents, which supports the very good solubility of X-Po in all solvents. Unfortunately, this empirical description cannot be used to identify whether a solvent has a better affinity with the polymer X-Po than another one.

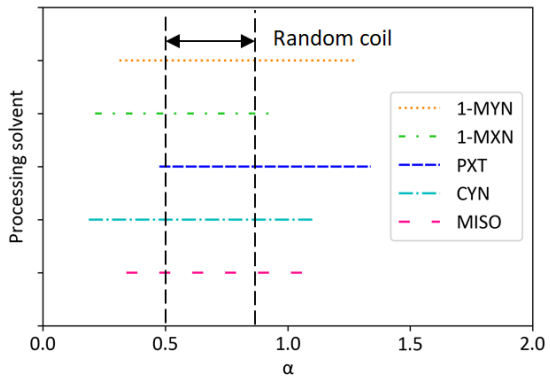

Figure 4.8: Spread of α value calculated from the uncertainties in the polydispersity and in the measurement errors.

Huggins and Kramer constants: K_H and K_K

The intrinsic viscosity $[\eta]$, describing the polymer contribution to the viscosity of polymer solution, can be also determined using the Huggins equation as well as the Kramer equation. While the Huggins equation uses the specific viscosity to define the intrinsic viscosity, the Kramer equation uses the reduced viscosity. The Huggins equation can be applied in a range of moderate concentrations (Eq. 4.7). It displays a linear dependence of $\frac{\eta_{sp}}{c}$ to the polymer solution concentration, and is defined as:[113]

$$\frac{\eta_{sp}}{c} = [\eta] + K_H[\eta]^2 c \tag{4.7}$$

where η_{sp} is the specific viscosity, c is the polymer concentration in the solution, $[\eta]$ is the intrinsic viscosity of the polymer solution and K_H is the dimensionless Huggins constant.

In the Kramer plot shown in Figure 4.9, plotting $\frac{\ln \eta_r}{c}$ versus c, $[\eta]$ can be determined by a linear extrapolation to the zero concentration.[114] $[\eta]$ is the y-intercept and $-K_K[\eta]^2$ is the slope, according to the Kramer equation:

$$\frac{\ln \eta_r}{c} = [\eta] - K_K[\eta]^2 c \tag{4.8}$$

where η_r is the reduced viscosity defined as $\eta_r = \frac{\eta_{solution}}{\eta_{solvent}}$, c is the polymer concentration in the solution, $[\eta]$ is the intrinsic viscosity of the polymer solution and K_K is the dimensionless Kramer constant.

X-Po was dissolved in 1-methylnaphthalene, 1-methoxynaphthalene, 3-phenoxytoluene, cyclohexyl hexanoate and in menthyl isovalerate at the following concentrations: 1 g·L^{-1}, 2 g·L^{-1}, 3 g·L^{-1}, 4 g·L^{-1} and 5 g·L^{-1}. Viscosity of each solution was measured at 25°C, and the respective specific viscosities determined by $\eta_{sp} = \frac{\eta_{solution}}{\eta_{solvent}} - 1$ were calculated. The intrinsic viscosity $[\eta]$ was graphically determined, as displayed in Figure 4.9.

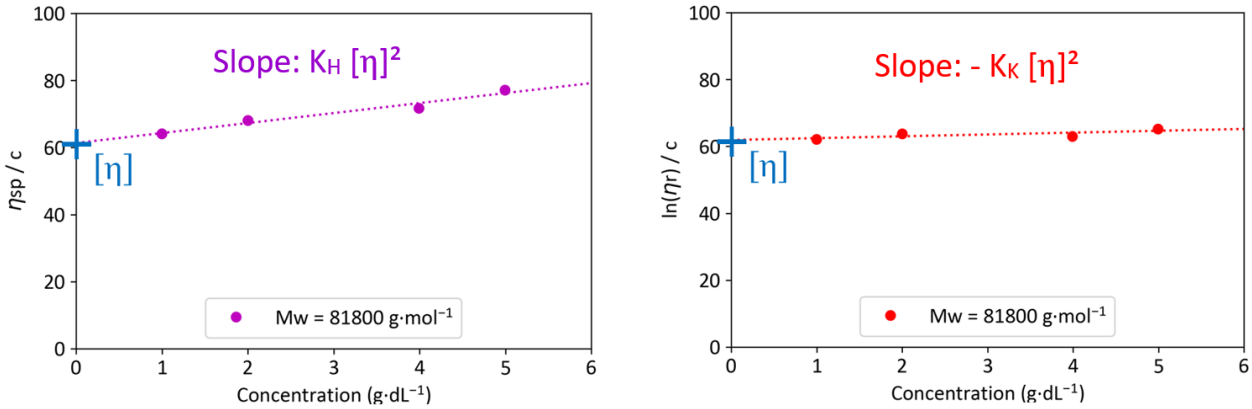

Figure 4.9: Graphical determination of the Huggins constant K_H (left) and Kramer constant K_K (right) for the polymer solution of X-Po in CYX. The molecular weight of 81.800 g·mol^{-1} was used for the determination of K_H and K_K. The y-intercept of the Huggins and Kramer plots is the intrinsic viscosity of the polymer solution.

The Huggins equation is valid for a wider range of concentrations than the Kramer equation.[115] Indeed, the Kramer plot turns into a slightly curved plot whereas the Huggins plot remains linear. The calculated Huggins and Kramer constants are displayed in Table 4.3.

Table 4.3: Huggins and Kramer constants K_H and K_K, respectively.

	K_H	K_K
1-MYN	0.31	-0.17
1-MXN	0.67	-0.04
PXT	0.78	0.15
CYX	0.79	0.15
MISO	0.80	0.12

The Huggins constant K_H is an indicator of the polymer-solvent affinity. A good affinity is characterised by a low value of K_H, less than the theta point at 0.5. Above 0.5, K_H indicates a weak affinity between the polymer and the solvent. Concerning the Kramer constant K_K, a *good* solvent leads to a negative K_K and a *bad* solvent produces a positive value. From the five tested solvents, three of them are identified as *bad* solvent from both Huggins and Kramer constants. 3-phenoxytoluene,

cyclohexyl hexanoate and menthyl isovalerate are having a weak interaction with polymer X-Po. The solvent 1-methoxynaphthalene is close to the theta point. On the other hand, 1-methylnaphthalene is considered as a *good* solvent.

Both Huggins and Kramer equations can be plotted on the same graph to identify whether the curves meet at the concentration $c = 0$, as in Figure 4.10. It is an indicator of whether the calculations and the intrinsic viscosity determinations are meaningful. For the five X-Po tested solutions, Huggins and Kramer representations coincide at concentration $c = 0$. Therefore, the intrinsic viscosities determined by both equations are similar and are meaningful. Kramer and Huggins constants are useful to identify whether a solvent exhibits a stronger affinity to a given material than another one.

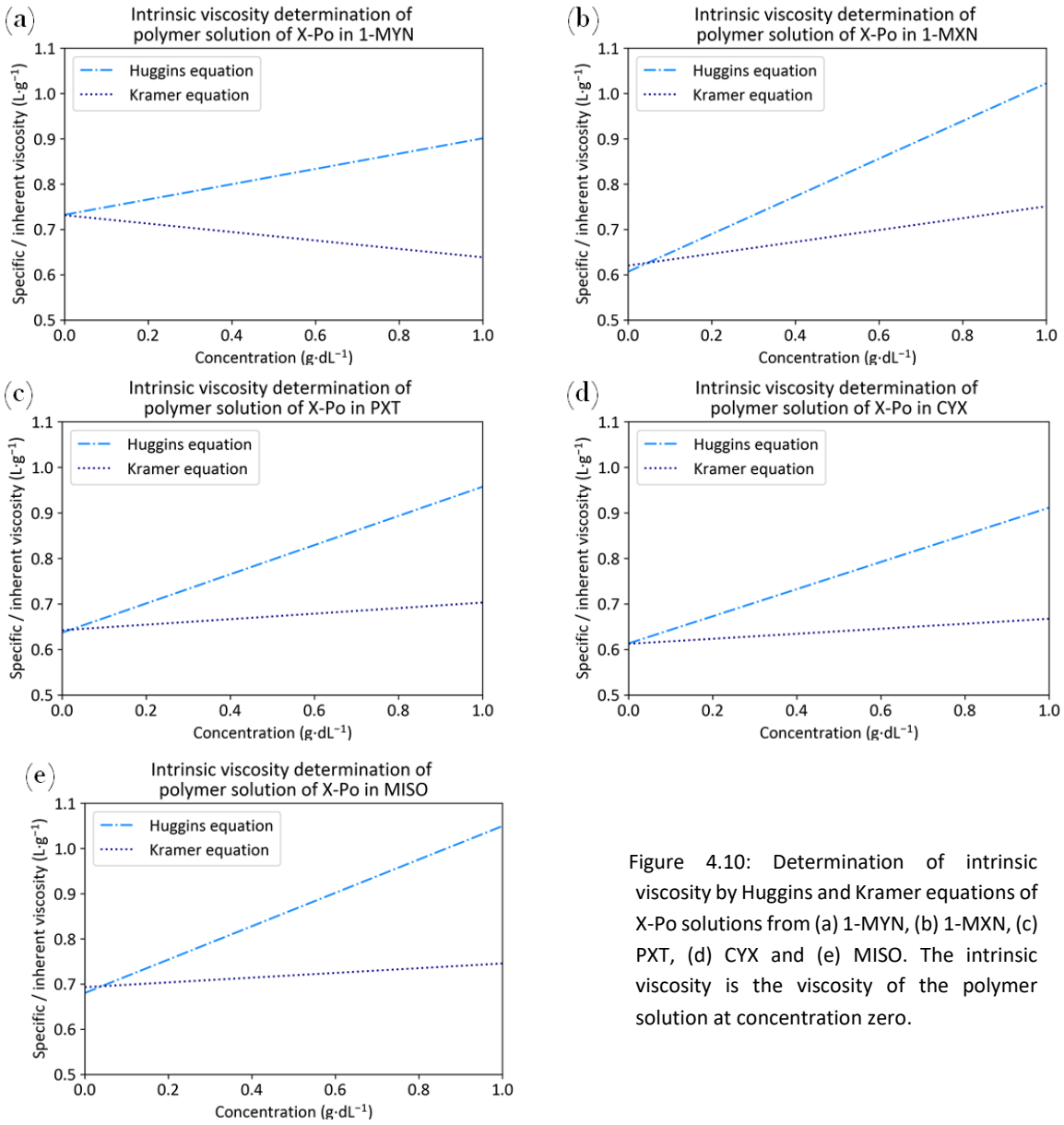

Figure 4.10: Determination of intrinsic viscosity by Huggins and Kramer equations of X-Po solutions from (a) 1-MYN, (b) 1-MXN, (c) PXT, (d) CYX and (e) MISO. The intrinsic viscosity is the viscosity of the polymer solution at concentration zero.

Solomon Ciuta equation: single point determination

At low polymer solution concentration, it can be assumed that both Huggins and Kramer equations are linear, as shown in Figure 4.10. Solomon Ciuta developed an empirical observation using a single point to determine the intrinsic viscosity of a polymer solution, stating that:[116]

$$[\eta] = \frac{\sqrt{2(\eta_{sp} - \ln \eta_r)}}{c} = \frac{\sqrt{2(\eta_r - 1 - \ln \eta_r)}}{c} \tag{4.9}$$

where $[\eta]$ is the intrinsic viscosity of the polymer solution, η_{sp} is the specific viscosity determined by $\eta_{sp} = \frac{\eta_{solution}}{\eta_{solvent}} - 1$, η_r is the reduced viscosity defined as $\eta_r = \frac{\eta_{solution}}{\eta_{solvent}}$, and c is the polymer concentration in the solution.

The Solomon Ciuta equation is valid only when the linear Huggins and Kraemer equations are both valid.[115] To perform the intrinsic viscosity evaluation, a polymer solution of X-Po at 0.1 g·L^{-1} was employed. The intrinsic viscosity of X-Po in 1-methylnaphthalene, in 1-methoxynaphthalene, in 3-phenoxytoluene, in cyclohexyl hexanoate and in menthyl isovalerate resolved by Solomon Ciuta equation are displayed in Table 4.4. A comparison of the intrinsic viscosities of the same polymer solutions determined by Mark-Houwink, Huggins and Kramer equations are also displayed.

Table 4.4: Intrinsic viscosities determined from Mark-Houwink equation, Huggins equation, Kramer equation and Solomon Ciuta equation.

	Intrinsic viscosity in L·g^{-1}			
	From Mark-Houwink equation	**From Huggins equation**	**From Kramer equation**	**From Solomon Ciuta equation**
1-MYN	0.73	0.73	0.73	0.74
1-MXN	0.61	0.61	0.62	0.64
PXT	0.64	0.64	0.64	0.66
CYX	0.61	0.61	0.61	0.65
MISO	0.68	0.68	0.69	0.72

In a very dilute polymer solution, the viscosity is defined as the viscosity of the pure solvent plus the contribution of the individual polymer chains. The intrinsic viscosity of a polymer solution describes the hydrodynamic volume of a polymer chain in a given solvent. Therefore, this measure gives an understanding of the polymer-solvent interaction. A low intrinsic viscosity is related to a small radius of gyration R_g and is obtained for a polymer in a *poor* solvent. Oppositely, a *good* solvent favours the polymer-solvent interaction resulting in a higher intrinsic viscosity.[117]

Mark-Houwink, Huggins, Kramer and Solomon Ciuta equations provide similar intrinsic viscosity values for polymer X-Po in 1-methylnaphthalene, in 1-methoxynaphthalene, in 3-phenoxytoluene, in cyclohexyl hexanoate and in menthyl isovalerate. The values are between 0.61 and 0.74 L·g^{-1}. The polymer X-Po has comparable intrinsic viscosities in all tested solvents and therefore hinders the identification of a preferred interaction of X-Po with a specific solvent. The Mark-Houwink and Solomon Ciuta equations cannot distinguish the difference in polymer-solvent interactions of the

investigated polymer solutions. However, the Huggins and the Kraemer constants identified disparities in the different polymer solutions. 1-methynaphthalene is found to exhibit the strongest interaction with X-Po, which correlates with the result obtained by the precipitation test in Chapter 4.1.1. Huggins and Kraemer constants also classified 3-phenoxytoluene, cyclohexyl hexanoate and menthyl isovalerate as *poor* solvents for X-Po. However, no differentiation of affinity is possible between the three solvents. Nevertheless, the trend obtained by Huggins and Kraemer constants goes along with the experimental measurements of the polymer-solvent interactions classifying the ink solvent from the *better* to the *worse* solvent as: 1-methylnaphthalene, 1-methoxynaphthalene, 3-phenoxytoluene, cyclohexyl hexanoate and menthyl isovalerate. This goes along with the apparently decreasing hydrophobicity of the solvents judged by the oxygen content of the solvents, as seen from Table 3.3.

4.2. Polymer size in solution

The size of a polymer chain in a solvent is directly related to the interaction of the polymer with the solvent molecules as detailed in Chapter 2.3.2. In this section, polymer size in solution was characterised by its radius of gyration R_g determined from Flory and Fox equation and by its volume fraction from Einstein equation.

Experimentally, the size of polymer in solution can be determined by various methods. Dynamic light scattering (DLS) and ultrasonic attenuation spectroscopy (UAS) are two widely used techniques. DLS, also called photon correlation spectroscopy, measures scattering intensity fluctuation over time of light passing through a solution. The fluctuations characterise the Brownian motion within the sample. These fluctuations are used to calculate the hydrodynamic radius R_h. On the other side, UAS applies plane sound waves moving through a solution. The attenuated wave is collected in a receiver and the size of polymer in solution is calculated. However, UAS suffers from a low resolution and the mathematical model requires intense data evaluation. Therefore, DLS was chosen to experimentally determine the polymer size in the tested solvents.

4.2.1. Radius of gyration

The size of a polymer in solution is defined by its radius of gyration described by R_g as in Figure 4.11.

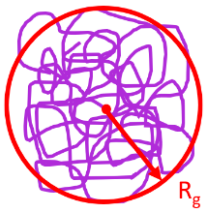

Figure 4.11: Radius of gyration R_g of a random coil polymer in solution.

In a *good* solvent, the polymer coil tends to expand, thus the radius of gyration of the polymer is bigger than the one of the same polymer in a *poor* solvent. The radius of gyration can be estimated by the Flory and Fox equation,[118] stating that:

$$[\eta] = \Phi' \cdot {R_g}^3 \cdot M^{-1} \tag{4.10}$$

or

$$R_g = \sqrt[3]{\left(\frac{[\eta]}{\Phi'} \cdot M_w\right)} \tag{4.11}$$

where $[\eta]$ is the intrinsic viscosity in $L \cdot g^{-1}$, R_g is the radius of gyration in m, $\Phi' = 2.1 \times 10^{26}$ $kmol^{-1}$ is a universal constant independent of temperature and polymer-solvent system[117] and M_w is the molecular weight of the polymer in $g \cdot kmol^{-1}$. The molecular weight can be calculated from the intrinsic viscosity of the polymer solution, determined in Chapter 3.1.4, utilising the Mark-Houwink parameters α and k,[119] as introduced in Chapter 2.3.3, by:

$$[\eta] = k \cdot {M_w}^{\alpha} \tag{4.12}$$

or

$$M_w = \sqrt[\alpha]{\left(\frac{[\eta]}{k}\right)} \tag{4.13}$$

The radii of gyration calculated for the polymer X-Po in 1-methylnaphthalene, 1-methoxynaphthalene, 3-phenoxytoluene, cyclohexyl hexanoate and in menthyl isovalerate are approximately equal to 1 nm and are displayed in Table 4.5. Taking into account the error carried by the Mark-Houwink parameters used to calculate the polymer molecular weight, and the error generated by the graphical determination of the intrinsic viscosity, it can be considered that the calculated radius of gyration of X-Po is similar in all tested solvents. Flory and Fox equation indicates that the diverse polymer sizes in the tested polymer solutions cannot be distinguished. To further investigate the polymer size in solution, the X-Po volume fraction will be determined by the Einstein equation supported by viscosity measurements. In addition, the polymer diameter in solution will be directly measured by dynamic light scattering where no calculation error is included.

Table 4.5: Radius of gyration of X-Po in the different solvents calculated by Flory and Fox equation.

Solvents	Calculated molecular weight ($g \cdot kmol^{-1}$)	Radius gyration (nm)
1-MYN	0.25273	0.5
1-MXN	30.14789	2.1
PXT	8.24511	1.4
CYX	0.53422	0.5
MISO	7.35939	1.3

4.2.2. Volume fraction

In 1945, Einstein established a relationship between the volume fraction Φ of suspended material and η the viscosity of the suspension. [120] For a sphere or a random coil, the equation is:

$$\frac{\eta}{\eta_s} = 1 + 2.5\Phi \tag{4.14}$$

where η is the viscosity of the suspension, η_s is the viscosity of the medium and Φ is the volume in parts of a cubic centimetre occupied by the dispersed solid.

The volume fraction Φ of X-Po in 1-methylnaphthalene, 1-methoxynaphthalene, 3-phenoxytoluene, cyclohexyl hexanoate and in menthyl isovalerate was calculated for the following concentrations: 1 g·L^{-1}, 2 g·L^{-1}, 3 g·L^{-1}, 4 g·L^{-1}, 5 g·L^{-1}, 10 g·L^{-1}, 30 g·L^{-1} and 50 g·L^{-1}. Up to a concentration of 10 g·L^{-1}, the volume fraction Φ occupied by X-Po in the tested solvents is identical, as shown in Figure 4.12. For 30 g·L^{-1} and 50 g·L^{-1}, the volume fraction of X-Po in menthyl isovalerate is distinctly higher than in the other solvents. Since menthyl isovalerate is a *poor* solvent for polymer X-Po, the increase in volume fraction occupied by X-Po can be explained by a measurement of the polymer chains aggregation. This is confirmed by the calculation of the dilute regime in Chapter 4.1 stating that the upper limit is 13 g·L^{-1} in all solvents. Therefore, the volume fraction measured does not correspond to a single polymer chain but to an aggregate. Like the Flory and Fox equation, the Einstein equation highlights that X-Po has a similar volume fraction in the five tested solvents. No discrepancy among the solvents can be established.

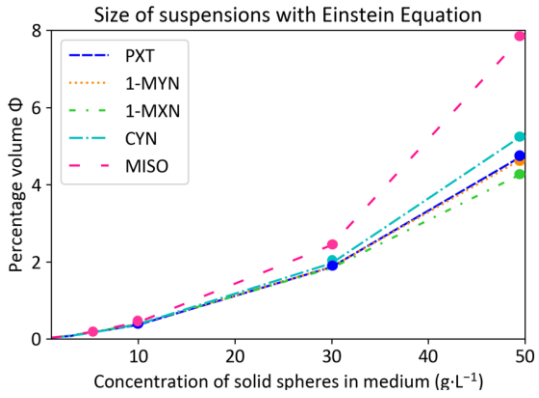

Figure 4.12: Volume fraction Φ of X-Po in the five solvents for various concentrations.

4.2.3. Polymer coil diameter

The polymer coil diameter of a polymer is determined by dynamic light scattering (DLS) and is influenced by the hydrodynamic interaction of a polymer chain with the solvent molecules.[121] Indeed, when a polymer chain moves, it causes the neighbouring solvent molecules to move with the polymer chain. Due to the Brownian motion of a polymer in a solvent, light-scattering fluctuates and an autocorrelator calculates the product of two scattering intensities separated by a delay time.[122] The autocorrelation function already teaches about the solution polydispersity and the polymer size in solution. The polydispersity is described by the peak width in the size distribution of the particle and by the gradient of the correlation coefficient. The size distribution representation by intensity is helpful to identify large particles in a solution of small particles, which is convenient for purity control for example. Besides, the size distribution representation by volume gives an understanding of the dominant particle size in solution.

The polymer solutions prepared using 1-methylnaphthalene, 1-methoxynaphthalene, 3-phenoxy-toluene, cyclohexyl hexanoate and in menthyl isovalerate at 50 g·L^{-1} were measured by DLS. In Figure

4.13 X-Po has a similar coil diameter of less than 1 nm in all tested solvents except in menthyl isovalerate where the peak is shifted to slightly larger size of roughly 1.7 nm. Malvern proclaims a measurement sensitivity down to 0.3 nm.[123] The measured X-Po diameter in the five tested solvents can be considered equal taking into account that these values are close to the detection limit. A concentration of 50 g·L^{-1} was required to get enough scattering, i.e., enough light intensity on the detector. However, at that concentration the polymer solutions are not in the dilute regime anymore. Therefore, the DLS measurements report the size of polymer aggregates. This is in agreement with the size in suspension obtained by the Einstein equation in Chapter 4.2.2.

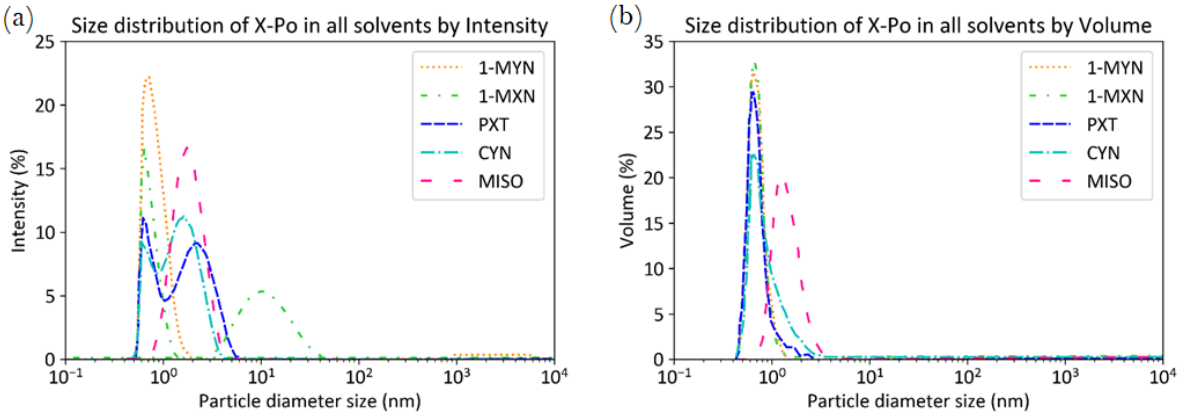

Figure 4.13: Size distribution of X-Po in all solvents represented by (a) intensity and (b) volume.

Measuring DLS of less concentrated polymer solutions would give the coil diameter of single polymer chains and not of an aggregate. However, X-Po met measurement limitations at low solution concentration since no signal could be detected. To get around this limitation, polymer X-Po should be investigated by DLS for a polymer with a higher molecular weight. The coiled single polymer chain would then be larger, would scatter more and there would be enough light to be detected, even at low concentrations.

4.3. Conclusion on polymer solution characterisation

In this chapter, the affinity of X-Po polymer with the ink solvents was investigated to characterise the polymer solutions made from 1-methynaphthalene, 1-methoxynaphthalene, 3-phenoxytoluene, cyclohexyl hexanoate and from menthyl isovalerate. The study was based on experimental measurements and empirical descriptions. The affinity of a polymer with a solvent indicates the intensity of interaction or binding occurring between the polymer chains and the solvent molecules. A solvent exhibiting a low interaction with a polymer is called a *poor* solvent and leads to enhanced intramolecular interactions resulting in a decrease of the radius of gyration R_g. On the opposite, in a *good* solvent, the polymer chains expand and tend to maximise their contact with the solvent molecules, resulting in a larger radius of gyration.

The polymer-solvent interaction is directly proportional to the polymer solubility in the solvent by the Hildebrand-Scott equation.[124] Thus, the solubility of a polymer in a solvent describes their interaction. To investigate the solubility of X-Po in the five solvents, the Non-solvent Induced Phase Separation

(NIPS) technique was performed by the use of the cloud-point determination. A non-solvent was added in the polymer solution dropwise until the solution turned turbid. Ethanol and acetone were tested as they are very *poor* solvents for X-Po. The more *poor* solvent needed to start the precipitation of the polymer solution, the stronger is the interaction between polymer and solvent. X-Po minimises its interaction more and more as it is dissolved in 1-methynaphthalene, in 1-methoxynaphthalene, in 3-phenoxytoluene, in cyclohexyl hexanoate and in menthyl isovalerate where it assumes a more collapsed conformation. The NIPS technique is a fast and material saving approach to judge the polymer-solvent interaction in different solutions.

An empirical observation was used to also characterise the polymer X-Po interaction with the five solvents. Most of the empirical descriptions investigate polymer solutions in the dilute regime. Fedor introduced a relationship between the overlap concentration c* and the intrinsic viscosity $[\eta]$ of the polymer solution, defined in Chapter 2.3.3. Mark-Houwink presented the parameters α and k, where α describes the polymer-solvent affinity. A *poor* solvent has α value from 0 to 0.5, a good solvent from 0.5 to 0.8, where 0.5 is the theta point. Above 0.8, α indicates that the polymer adopts an extended chain conformation. The determination of α is conducted graphically as well as the intrinsic viscosity, which describes the polymer contribution to the viscosity of the polymer solution. It turns out that X-Po has a random coil conformation in all solvents, which supports the very good solubility of X-Po in all solvents. Unfortunately, α cannot be used to distinguish between the solvents affinity with polymer X-Po. The intrinsic viscosity can also be determined using the Huggins and Kramer equations, introducing the constants K_H and K_K, respectively. While the Huggins equation uses the specific viscosity to define the intrinsic viscosity, the Kramer equation uses the reduced viscosity η_r. A good affinity is characterised by a low value of K_H, less than the theta point at 0.5. Above 0.5, K_H indicates a week affinity between the polymer and the solvent. Concerning the Kramer constant K_K, a *good* solvent leads to a negative K_K and a *bad* solvent produces a positive K_K. The Huggins and Kramer constants identified 3-phenoxytoluene, cyclohexyl hexanoate and menthyl isovalerate as solvents exhibiting the weakest interaction with X-Po, whereas 1-methoxynaphthalene is close to a theta solvent and 1-methylnaphthalene is considered as a *good* solvent for X-Po. At low polymer solution concentration, Solomon Ciuta developed an empirical observation with a single point to determine the intrinsic viscosity of a polymer solution using the reduced viscosity at one very low concentration. A low intrinsic viscosity is related to a small radius of gyration R_g and is obtained for a polymer in a *poor* solvent. Oppositely, a *good* solvent favours the polymer-solvent interaction resulting in a higher intrinsic viscosity. However, the intrinsic viscosities of the polymer solutions fall between 0.61 $L \cdot g^{-1}$ and 0.74 $L \cdot g^{-1}$ which are very similar. Thus one cannot distinguish the difference in polymer-solvent interactions of the investigated polymer solutions.

The size of the polymer X-Po in the solvents was then used to understand the interaction of the polymer with the solvent molecules. The radius of gyration R_g described by Flory and Fox equation was calculated with the intrinsic viscosity of the polymer solution, the polymer molecular weight and an universal constant independent of temperature and the polymer-solvent system given by $\Phi' = 2.1 \times 10^{26}$ $kmol^{-1}$. The radii of gyration calculated for X-Po in the five solvents are of same order of magnitude. So, the diverse polymer sizes in the tested polymer solutions could not be distinguished by the Flory and Fox equation.

Einstein describes the volume fraction Φ of polymer X-Po as being related to the ratio of the viscosity of the polymer solution by the viscosity of the pure solvent. Until a concentration of 10 $g \cdot L^{-1}$, the volume fraction Φ occupied by X-Po in the tested solvents is identical. Like Flory and Fox equation, Einstein equation highlights that X-Po has a similar volume fraction in the five tested solvents. No discrepancy among the solvents can be established. Above that concentration, the volume fraction measured does not correspond to a single polymer chain but to an aggregate.

Finally, the diameter of the polymer coil was investigated by DLS. It measures scattering intensity fluctuation over time of light passing through a solution. X-Po has a similar coil diameter of less than 1 nm in all tested solvents, except in menthyl isovalerate where the diameter is slightly larger of roughly 1.7 nm. A concentration of 50 $g \cdot L^{-1}$ was required to get enough scattering. However, at that concentration the polymer solutions are not in the dilute regime anymore resulting in the measurement of polymer aggregates.

In this chapter, various methods were tested to describe the polymer solution. The polymer-solvent affinity was characterised as the stability of a one-phase polymer solution when a non-solvent was added dropwise (NIPS), which gives a clear understanding of the polymer-solvent affinity depending on the tested solvent. X-Po has the stronger affinity with 1-methylnaphthalene, and it reduces as it goes with 1-methoxynaphthalene, 3-phenoxytoluene, cyclohexyl hexanoate, and the weakest affinity of X-Po is with menthyl isovalerate. The trend was confirmed by Huggins and Kramer constants, which could identify a solvent group affinity where 1-methylnaphthalene was a *good* solvent, 1-methoxynaphthalene a theta solvent, and the other solvents were considered *poor* solvents. Then, empirical and experimental approaches, such as the Mark-Houwink parameters, Solomon Ciuta equation, Flory and Fox equation, Einstein equation, and DLS were tested on the polymer solutions but could not distinguish the different polymer-solvent affinity. Polymer-solvent affinity is a critical information to understand the polymer conformation in solution and it was successfully described by the NIPS method.

5. Polymer cross-linking in bulk material and thin films

In this study, the degree of cross-linking of a thin film of a hole transport polymer is presented as a dependency on the ink formulation. An understanding of the correlation between layer stability and solvent exposure and the degree of cross-linking in a film was investigated. The degree of cross-linking of the material is defined by the ratio of the cross-linking reaction enthalpy in film to the cross-linking reaction enthalpy of the pure powder without solvent, determined by differential scanning calorimetry (DSC). The layer stability against solvent exposure is determined by the variation of layer topography induced by a solvent drop left on the layer surface for a given duration. A selection guideline for promising new ink solvents is discussed.

5.1. Cross-linking of X-Po in powder without solvent

To understand the cross-linking mechanism of the styrene unit contained in the polymer X-Po, it was first investigated in powder without solvent. The reaction involving two styrene units is described and followed by infrared spectroscopy (IR). The physical transformation of X-Po during heat treatment was characterised by DSC.

5.1.1. Styrene cross-linking reaction

IR spectroscopy was used to study the cross-linking process of styrene, the cross-linker unit contained in X-Po. During cross-linking of the polymer, the styrene signal reduces or disappears.[125] A US patent discloses the resulting species of the cross-linking reaction of two styrene units,[126] displayed in Figure 5.1.

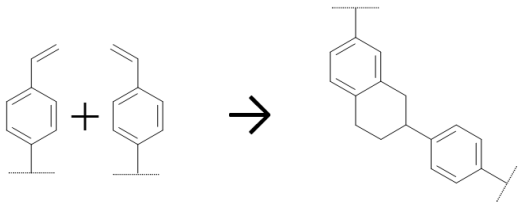

Figure 5.1: Resulting species of the cross-linking reaction of two styrene units, disclosed by US patent from reference.[126]

G. Klärner et al. described the intensity variations of vibration bands while the styrene cross-linking reaction occured.[127] Considering that only 10% of X-Po monomers contain the styrene cross-linker unit, the vibration bands corresponding to styrene and the resulting species after cross-linking are suffering from a weak intensity compared to all other IR vibrations of the polymer chain. Therefore, the polymer 7X-Po, characterised by 70 % of its monomers containing the styrene unit, was examined to accentuate the intensity variations of vibration bands during cross-linking. To perform the cross-linking reaction in powder, 7X-Po and X-Po were treated by a DSC heating ramp from room temperature to 300°C with a gradient of 20 $K \cdot min^{-1}$.

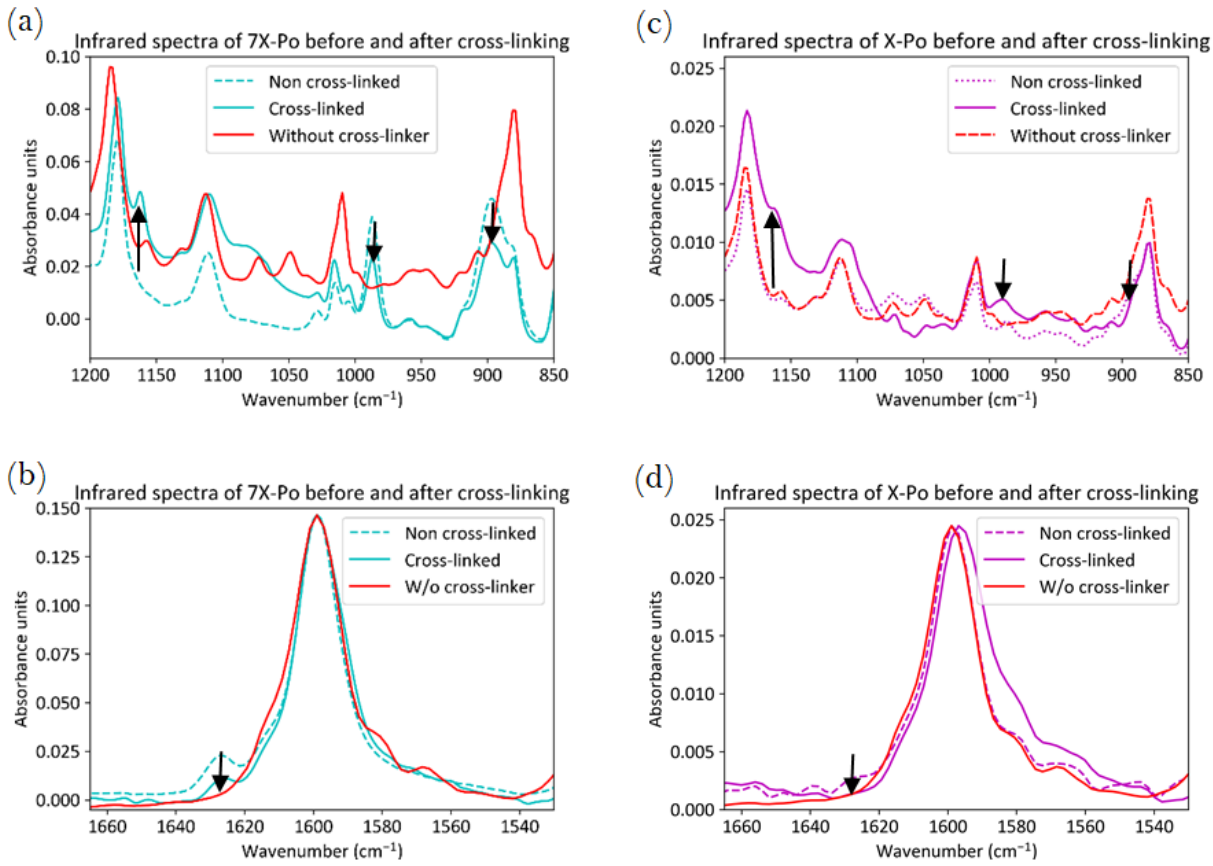

Figure 5.2: Infrared spectra of polymer powders of 7X-Po and X-Po before and after cross-linking through one DSC run from room temperature to 300°C at 20 K·min^{-1}. The spectrum of 7X-Po is displayed in (a) from 850 cm^{-1} to 1200 cm^{-1} and in (b) from 1530 cm^{-1} to 1665 cm^{-1}. The spectrum of X-Po is displayed in (c) from 850 cm^{-1} to 1200 cm^{-1} and in (d) from 1530 cm^{-1} to 1665 cm^{-1}.

Before heat treatment, the IR spectra of 7X-Po and X-Po samples both exhibit peaks around 905 cm^{-1} and 990 cm^{-1} associated to vinyl C-H out-of-plane bending vibrations. These weak bands are characteristic of the styrene unit. Another peak around 1630 cm^{-1} is visible before heating and is related to terminal vinyl C-C stretching absorption. After heating the powders, these three vibration bands decrease significantly for 7X-Po and disappear for X-Po, see Figure 5.2. New bands emerge after cross-linking, around 1165 cm^{-1} and 1175 cm^{-1}, which are affiliated to new C-C stretching vibrations.

In Figure 5.2, the infrared spectrum of Po, the non-cross-linkable version of X-Po is also displayed. It is a polymer chain without styrene cross-linker and is used as a reference to identify if the cross-linking reaction results in all styrene units reacted. In the case of X-Po, the cross-linked polymer overlaps with the Po spectrum around 905 cm^{-1}, 990 cm^{-1} and 1630 cm^{-1} indicating that all styrene units reacted. On the contrary, the spectrum of 7X-Po shows residual vibrations at these bands revealing that the cross-linking is not completed after the applied DSC heating ramp.

IR spectroscopy is a powerful analysis method to record the cross-linking reaction of styrene units. However, the signal strength is limited in the case of X-Po due to the low proportion of styrene in the polymer chain. The larger styrene content of 7X-Po provides a distinct understanding of the styrene cross-linking reaction. The results support the mechanism discussed in the literature.[126]

5.1.2. Cross-linking reaction enthalpy

DSC is a technique measuring the heat capacity of a material or mixture of materials in response to change of temperature. The sample, in form of powder, film or solution is placed inside a hermetically sealed aluminium pan. In the heat-flux DSC, the sample pan and the empty reference pan are set on thermocouples localised inside a furnace which is heated to the desired temperature at a given heating rate. While the sample and reference pans are heated up through the thermocouples, the heat capacity of the sample results in a temperature difference between the sample plan and the reference pan. This difference is measured by the thermocouples and is used to calculate the heat flow by the thermal equivalent of Ohm's law:

$$q = \frac{\Delta T}{R} \tag{5.1}$$

where q is the sample heat flow, ΔT is the temperature difference between the sample pan and the reference pan, and R is the thermal conductivity. Since a DSC measurement is running at a constant pressure, the heat flow is equivalent to an enthalpy change. The difference in heat flow between the sample and the reference is given by:

$$\Delta \frac{dH}{dt} = \left(\frac{dH}{dt}\right)_{sample} - \left(\frac{dH}{dt}\right)_{reference} \tag{5.2}$$

$$\text{with } \left(\frac{dq}{dt}\right)_P = \frac{dH}{dt} \tag{5.3}$$

where H is the enthalpy and $\frac{dH}{dt}$ is in $W \cdot s^{-1}$. In a DSC thermograph, the integral under a peak, above the baseline, gives the total enthalpy change for a physical transition. A thermogram of polymer material can reveal various physical reactions, such a glass transition at the temperature T_g, crystallisation, melting and cross-linking. To render visible specific reactions, the temperature rate should be carefully chosen. Generally, polymer materials are investigated by a heating rate between 20 $K \cdot min^{-1}$ and 50 $K \cdot min^{-1}$.

To identify the cross-linking reaction, the pure powders of X-Po and its analogue Po were measured at a heating rate of 20 $K \cdot min^{-1}$. Due to a programmed heating experiment, a change in baseline at the start-up can be observed in Figure 5.3 (a) and (b) resulting from a difference in the heat capacity of the sample and the reference. This difference can be explained by a weight discrepancy between the sample and the reference. The cross-linking reaction was first identified as an exothermic reaction, meaning heat was released, see Figure 5.3. Indeed, the only difference between Po and X-Po is the presence of a cross-linker unit. Therefore, the exothermic peak visible in X-Po thermogram is attributed to the cross-linking reaction at 250°C. By comparing the thermogram of X-Po with its non-cross-linkable analogue, the glass transition temperature T_g of the polymers is determined to be 130°C.

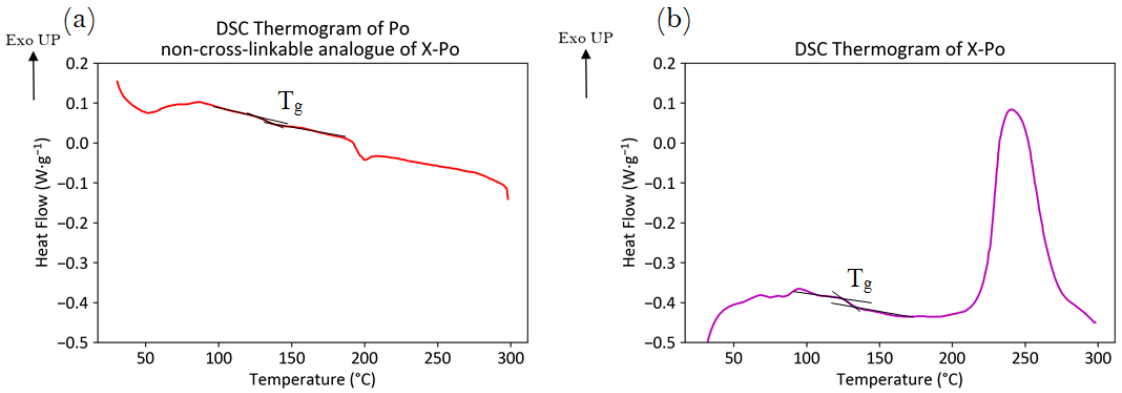

Figure 5.3: Thermograms of (a) Po and (b) X-Po polymer powders. The thermograms were recorded with a single heat ramp from room temperature to 300°C at a heating rate of 20 K·min^{-1}.

In addition, the thermal stability of the polymer powder was investigated by thermogravimetric analysis (TGA) from room temperature to 500°C. No weight loss was recorded until 370°C, as shown in Figure 5.4. Most degradation occurred at temperatures above 400°C. Polymer X-Po can be heated until 300°C without undergoing degradation.

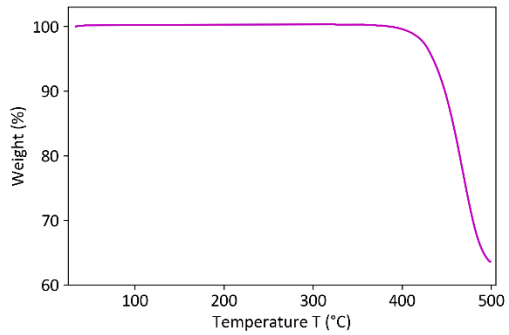

Figure 5.4: Thermal analysis of X-Po from room temperature to 500°C measured by TGA in nitrogen atmosphere.

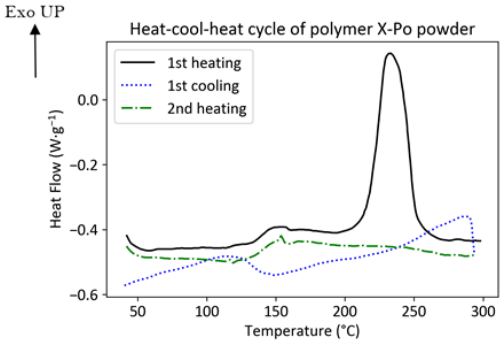

Figure 5.5: DSC thermogram of polymer X-Po powder in a heat-cool-heat cycle between room temperature and 300°C at a heating rate of 20 K·min^{-1}.

For the quantification of X-Po cross-linking efficiency, a heat-cool-heat cycle was recorded for polymer X-Po in form of powder without solvent, displayed in Figure 5.5. The heat ramp from room temperature to 300°C was repeated in a second run to check whether the cross-linking reaction was fully completed after the first heat ramp.[128] In the first run, a broad exothermic peak was observed in the X-Po thermogram in the temperature range between 200°C and 300°C, with a maximum peak at 240°C and an enthalpy of 49 J·g^{-1}. The exothermic peak represents a heat release during cross-linking. In the second run, no exothermic peak was observed between 200°C and 300°C confirming that the cross-linking reaction was completed after the first heat ramp.[129] After one DSC temperature cycle, the X-Po powder was not soluble anymore in 3-phenoxytoluene, even at a low concentration of 5g·L^{-1}, see Figure 5.6. The change of X-Po weight was recorded before and after being stirred in 3-phenoxytoluene for 24 hours. No weight loss was reported. This confirms the interpretation of the heat-cool-heat cycle of the X-Po thermogram, indicating that the cross-linking reaction was completed. The cross-linking enthalpy of 49 J·g^{-1} corresponds to 100% of cross-linking and is used in the following sections as reference.

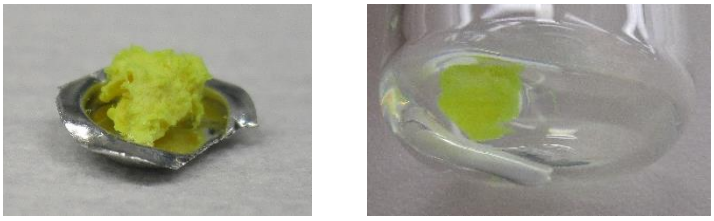

Figure 5.6: X-Po powder after undergoing a DSC run in a crucible from room temperature to 300°C (left) and after being stirred in 3-phenoxytoluene at a nominal concentration of 5 $g \cdot L^{-1}$ for 24 hours (right). 0% ±1% weight loss of the sample was measured after removing the supernatant of solvent and drying the solid.

5.2. Significance of cross-linking in polymer solution

In this section, the influence of ink solvent on the cross-linking reaction of polymer X-Po is investigated in more detail. In solution, cross-linker units are surrounded by solvent molecules which can enhance or reduce the cross-linking efficiency dependent on the polymer conformation in solution. The hypothesis is that a more collapsed conformation increases the reaction efficiency since the polymer chains are more attracted to each other than the solvent molecules. To review the cross-linking in solution, rheology and dynamic light scattering (DLS) measurements were performed.

5.2.1. Rheology investigation

It is well established that polymer molecular weight and chain length increase during cross-linking.[130] Increasing the molecular weight of a material having a linear structure is known to increase the viscosity of a solution.[122] Thus, when a polymer starts to cross-link in solution, the viscosity of the solution will increase.

Viscosity measurements can be performed with various instruments such as capillary, vibrational and rotational viscometers. The advantage of rotational viscometers is that fluid viscosity is determined as a function of shear rate by measuring the torque needed to turn an object in a fluid. The dependency of viscosity regarding shear rate gives an important information especially for the application of inkjet printing where the ink undergoes extreme shear stress at the jetting step through the nozzle. The most popular rotational viscometer for viscoelastic fluids is the cone-and-plate geometry.[117]

Figure 5.7 exhibits the viscosity increase of X-Po solutions which were heat-treated for three hours to initiate cross-linking in solution. None of the solutions shows an increased viscosity (determined after cooling at the otherwise same measuring conditions) up to a treatment temperature of 140°C. The polymer solution prepared using menthyl isovalerate (MISO) cross-links at 170°C. The polymer solution formulated with cyclohexyl hexanoate (CYX) reveals an increase of viscosity at 170°C, and cross-links at 180°C. A gradual viscosity increase is observable for the solution from 3-phenoxytoluene (PXT) up to 7-fold after heat treatment at 200°C. Higher temperatures led to very viscous solutions that are not measurable with the employed rheometer. The polymer solutions prepared using 1-methylnaphthalene (1-MYN) and 1-methoxynaphthalene (1-MXN) display a stable viscosity

independent of the heat treatment. The most reasonable explanation is that no measurable cross-linking reaction started in these two solutions.

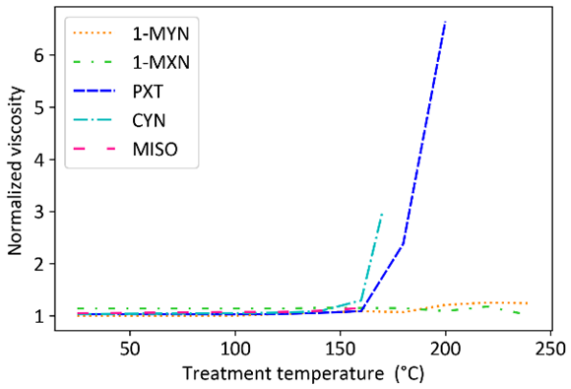

Figure 5.7: Viscosities polymer solutions of 50 g·L^{-1}.measured at room temperature after heat treatment for three hours at indicated temperature. The viscosities are normalised to the solution viscosity before heat treatment.

Table 5.1: Photographs of X-Po solutions from cyclohexyl hexanoate and from menthyl isovalerate after a heat treatment of 170°C and 180°C for three hours and cooling down to room temperature.

Solvent used to prepare the polymer solution	Treated at 170°C	Treated at 180°C
CYX	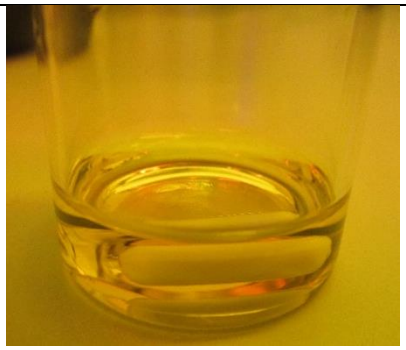	
MISO	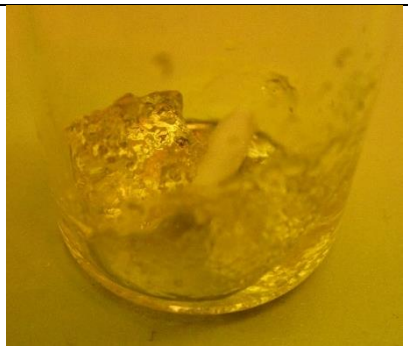	

The polymer solution prepared using menthyl isovalerate shows a constant viscosity up to a treatment temperature of 160°C. After a heat treatment of 170°C and 180°C, the polymer solution turns into a very viscous, jelly-like consistency. The polymer solution prepared using cyclohexyl hexanoate revealed a 3-fold viscosity after a heat treatment of 170°C. It can be seen in Table 5.1 that the solution exhibits a solid structure at 180°C.

Using rheology to track the cross-linking reaction of X-Po in solution gives an evident indication of macroscopic changes and an understanding of the difference between the tested polymer solutions. A polymer solution prepared using a *poor* solvent cross-linked at lower temperature than a polymer

solution prepared using a *good* solvent. However, no change in viscosity indicates that the degree of cross-linking is not preeminent enough to impact the viscosity of the solution. To study small cross-linking phenomenon, DLS was performed since it can detect change in polymer size even in small volumes.

5.2.2. Variation of species' size in solution

In order to study the cross-linking reaction in more detail and especially the start of the reaction, DLS was used to record changes of species size down to the nanometre scale. The polymer solutions were first measured after being dissolved at 50 $g \cdot L^{-1}$ at room temperature and filtered. The polymer solutions which were heat-treated for three hours at various temperatures to initiate cross-linking were also measured. The variation of polymer size in solution is an indication that the cross-linking reaction took place. However, due to optical transmission requirements and viscosity limitations, a choice of measured solutions had to be made. High viscous solutions could not be measured as well as solutions whose light absorption interfered with the measurement. The chosen polymer solutions were measured at 25°C and are displayed in Table 5.2.

Table 5.2: Temperatures applied to the polymer solutions for 3 hours prior to DLS measurements which were performed at room temperature. The purpose was to identify the progress of cross-linking in solution.

Solvent used to make the polymer solution	**Temperature applied for three hours to the polymer solutions**				
1-MYN	RT		160°C		200°C
1-MXN	RT		160°C		200°C
PXT	RT		160°C	180°C	
CYX	RT	140°C	160°C		
MISO	RT	140°C	160°C		

The size distribution of the polymer solutions measured by DSL can be represented by intensity or by volume. Both representations lead to different learnings. A minority of large particles can be identified by an intensity representation of the size distribution. Oppositely, the size distribution representation by volume gives an understanding of the dominant particle size in solution. In case of a homogeneous solution of one species size, both intensity and volume will show the same size distribution. However, if the solution is heterogeneous, one or the other representation will bring different information about the species. Intensity distribution highlights the presence of large species since they are the ones with the largest scattering intensity contribution. This is of great interest to identify the cross-linking progress in solution because even a small amount of cross-linked polymer chains will be visible. If only a few polymer chains started to cross-link in solution, the volume representation will reveal a high peak in small species size. In the intensity distribution, these few long chains will be represented by a peak in the bigger size range. Therefore, both intensity and volume representations are complementary in the understanding in cross-linking of polymer X-Po in solution.

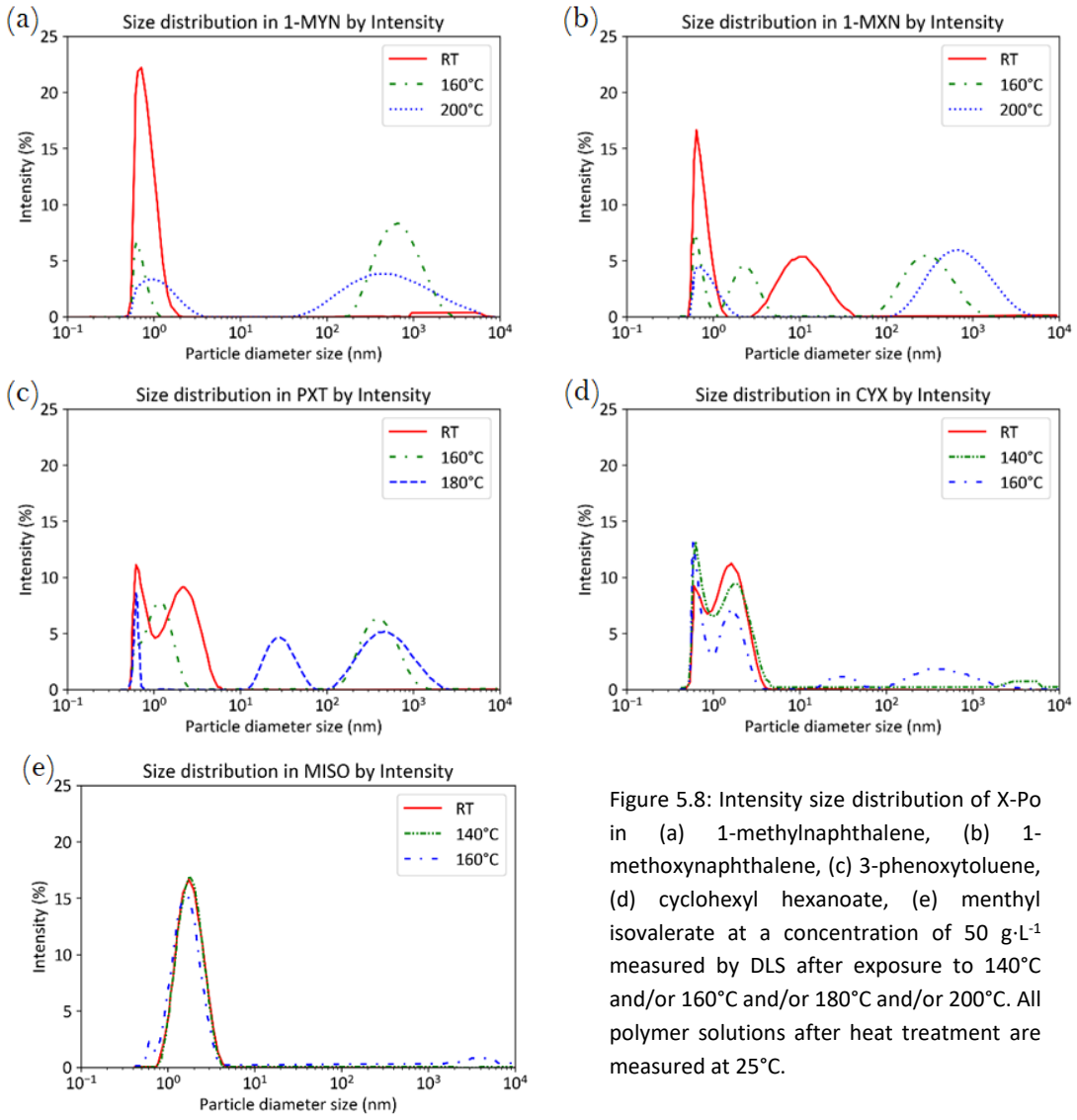

Figure 5.8: Intensity size distribution of X-Po in (a) 1-methylnaphthalene, (b) 1-methoxynaphthalene, (c) 3-phenoxytoluene, (d) cyclohexyl hexanoate, (e) menthyl isovalerate at a concentration of 50 $g \cdot L^{-1}$ measured by DLS after exposure to 140°C and/or 160°C and/or 180°C and/or 200°C. All polymer solutions after heat treatment are measured at 25°C.

From the rheology experiments, no change of viscosity was recorded for the polymer solutions using 1-methylnaphthalene and 1-methoxynaphthalene over the whole tested temperature range. However, the DLS measurements show that larger size species are appearing when the solution was exposed to a heat treatment of at least 160°C for all polymer solutions, suggesting that cross-linking of polymer chains does occur, see Figure 5.8. Being very sensitive to large particles, the intensity representation does not inform about the proportion of these cross-linked chains relatively to the non-cross-link counterparts. This is an important information when correlating these results with the rheology analyses.

From the volume distribution, it becomes obvious that the cross-linked part represents a very small volume of the overall polymer chains since no peak is visible in the larger species size in the polymer solutions prepared using 1-methylnaphthalene and 1-methoxynaphthalene, see Figure 5.9. The small fraction of cross-linked chains highlighted by the volume distribution is in line with the constant viscosity of both polymer solutions after a heat treatment of 160°C reported in Chapter 5.2.1.

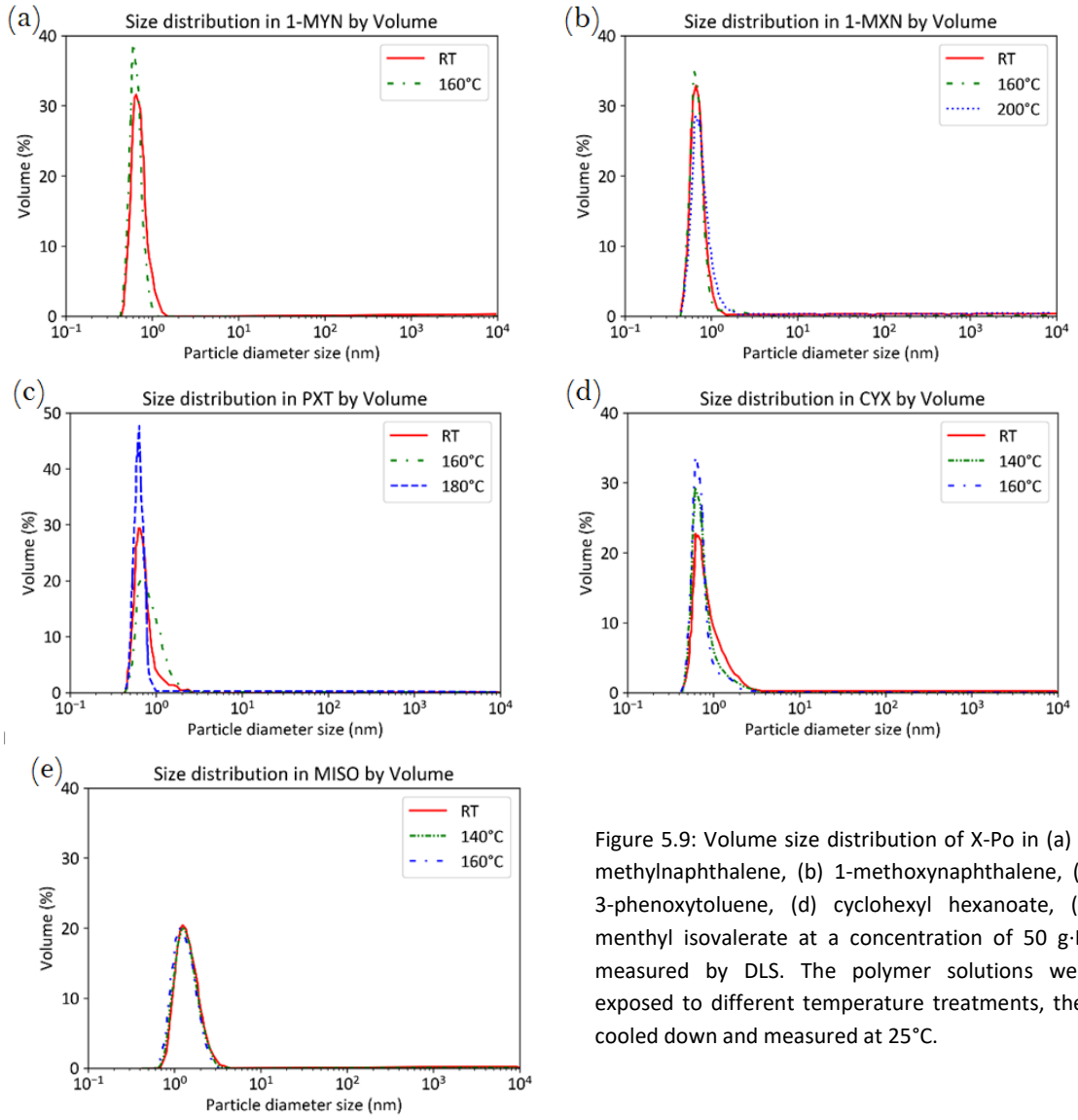

Figure 5.9: Volume size distribution of X-Po in (a) 1-methylnaphthalene, (b) 1-methoxynaphthalene, (c) 3-phenoxytoluene, (d) cyclohexyl hexanoate, (e) menthyl isovalerate at a concentration of 50 $g \cdot L^{-1}$ measured by DLS. The polymer solutions were exposed to different temperature treatments, then cooled down and measured at 25°C.

A gradual viscosity increase is observable for the solution from 3-phenoxytoluene, up to 7-fold after heat treatment at 200°C. However, solutions from 3-phenoxytoluene could only be measured by DLS until 180°C heat treatment to respect the optical transmission requirements as well as the polydispersity limitation. The size distribution measured in the polymer solutions prepared with 3-phenoxytoluene shows that cross-linking occurs already in solution treated at 160°C. No peak is visible in the larger species size in the volume distribution which means that the contribution of the cross-linked chains is small. However, the peak for small species gets broader, expressing that a small shift of the polymer size occurs. This correlates with the small change in viscosity recorded for the polymer solution after a heat treatment at 180°C.

The polymer solutions prepared using cyclohexyl hexanoate and menthyl isovalerate exhibits a fast and efficient cross-linking reaction in solution, as demonstrated by rheology. Larger species are visible in the size distribution by intensity for both polymer solutions after a heat treatment at 160°C. This means that the cross-linking reaction starts between 140°C and 160°C. A heat treatment of 170°C is enough to cross-link the polymer solution prepared using menthyl isovalerate, as seen in Table 5.1, revealing a fast reaction.

Due to optical limitations, DLS could not be applied to all polymer solution after heat treatment. However, its high sensitivity taught about the presence of cross-linked polymer chains where rheology could not yet identify viscosity variations. The DLS results complement the rheology measurements and a complete investigation of the cross-linking reaction in solution from the nanoscale up to the macroscopic scale is possible.

5.2.3. Cross-linking reaction enthalpy in solution

Differential scanning calorimetry measurements were carried out to study the impact of the ink solvent on X-Po cross-linking reaction in solution. We neglect the solvent used for polymer precipitation during the purification step after the synthesis. The investigation of X-Po cross-linking in solution was performed by pouring 30 µL of a 50 g·L^{-1} suspension in 3-phenoxytoluene. In solution, solvent boiling has a much higher reaction enthalpy than X-Po cross-linking reaction. Since the cross-linking reaction and boiling are occurring in the same temperature range, the resulting thermogram of the polymer solution from PXT is containing only the boiling information, with a boiling point of 270°C as visible in Figure 5.10a. A short vacuum run was applied to another sample to remove most of the solvent. In this case, solvent boiling has a significant smaller reaction enthalpy, as visible in Figure 5.10b. However, the applied vacuum was not enough to remove all solvent leading to droplet formation inside the pan identified by a broad endothermic peak starting at 200°C. Droplets are formed at a lower temperature since a higher volume of solvent molecules slows down the heat transfer. Therefore, no broad endothermic peak is visible from 200°C in Figure 5.10a.

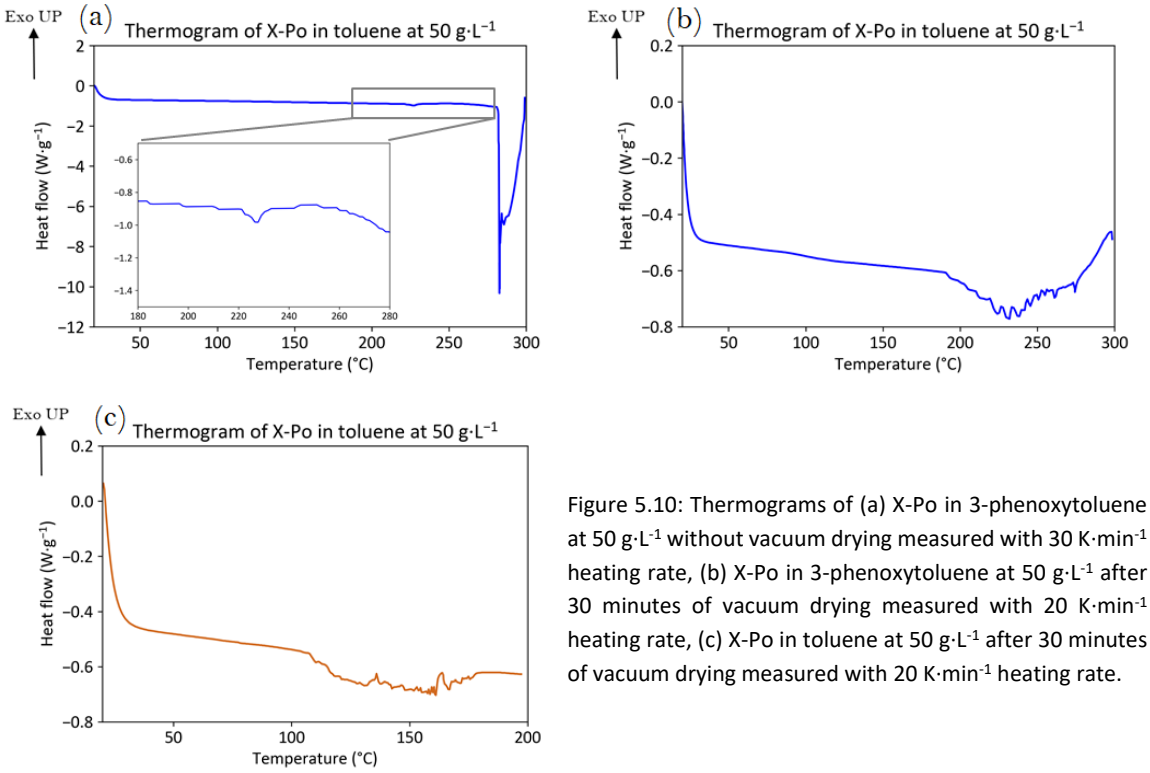

Figure 5.10: Thermograms of (a) X-Po in 3-phenoxytoluene at 50 g·L^{-1} without vacuum drying measured with 30 K·min^{-1} heating rate, (b) X-Po in 3-phenoxytoluene at 50 g·L^{-1} after 30 minutes of vacuum drying measured with 20 K·min^{-1} heating rate, (c) X-Po in toluene at 50 g·L^{-1} after 30 minutes of vacuum drying measured with 20 K·min^{-1} heating rate.

To confirm that the endothermic signal is boiling, a polymer solution was made from another solvent of different boiling point. X-Po was dissolved in toluene at 50 g·L^{-1}, then poured in a DSC pan and

dried under vacuum for 30 minutes. In Figure 5.10c one observes the toluene boiling reaction starting around its boiling point of 110°C, confirming that the endothermic peaks correspond to solvent boiling.

The presence of high boiling point solvents renders impossible the cross-linking analysis of X-Po since both reactions occur at similar temperatures. Therefore, to measure the cross-linking enthalpy of X-Po, the content of solvent should be reduced to a minimum, which amount to the content in films.

5.3. Polymer cross-linking in film

Cross-linking of X-Po was also examined in films processed from inkjet printing (IJP) solvents. This study of great significance emphasises the feasibility to build up a multilayer architecture by efficient HTL cross-linking in an IJP OLED device. Due to the high boiling point of IJP solvents, it is possible that not all solvent molecules are evaporated during vacuum drying, meaning that a small quantity is trapped in the films. Thus, the cross-linking reaction in the film might take place in the presence of these residual solvent molecules. To study the cross-linking efficiency in film, the film stability against solvent exposure was investigated. The degree of cross-linking in film was measured by DSC and the impact on the optical properties of the film was evaluated by ellipsometry.

5.3.1. Sample preparation

A fabrication process for printed large area films had to be established to perform the thin film stability test against solvent exposure by means of optical measurements. Optical measurements would be influenced by the bank substrate. In addition, film stability against solvent exposure is determined experimentally by surface deformation and a large measurement area is needed which is not the case in a pixelate substrate. So, a large and flat surface would simplify the analysis or make it possible at all. The challenge of building large area films by inkjet printing lies in film formation and film pinning on a substrate. Indeed, the developed inks are composed of low surface tension solvents enhancing the desired wetting in a pixelated substrate. However, a low surface tension ink tends to spread out on a flat substrate without a bank, making it hard to assume a predetermined pattern. In addition, inkjet printing is adapted to print small pattern due to the small droplet of a diameter around 20 µm (for 10 pL droplets). To form a large and homogeneous film, the droplet needs to merge with the neighbouring one, and the coffee-ring effect must be controlled. Usually, film formation is influenced by mixing solvents of different polarity and/or boiling points, which could not be done in this study since the pure solvents were to be reviewed.

Ink wetting

The wetting of an ink on a substrate describes the spreading of an ink droplet over a contact surface. When the droplet meets the substrate, the inertia of the droplet impacts the ink spreading. The surface tension of the ink must match the surface energy of the substrate in order to obtain the targeted wetting. However, it is often not that simple. The ink wetting is also influenced by other factors such as the viscosity as demonstrated in the example in Figure 5.11. The polymer X-Po was dissolved in two solvents of similar surface tension but of different viscosities differing by 3 mPa·s. Menthyl isovalerate has a slightly higher viscosity than cyclohexyl hexanoate and this leads to a considerable wetting difference of the two inks.

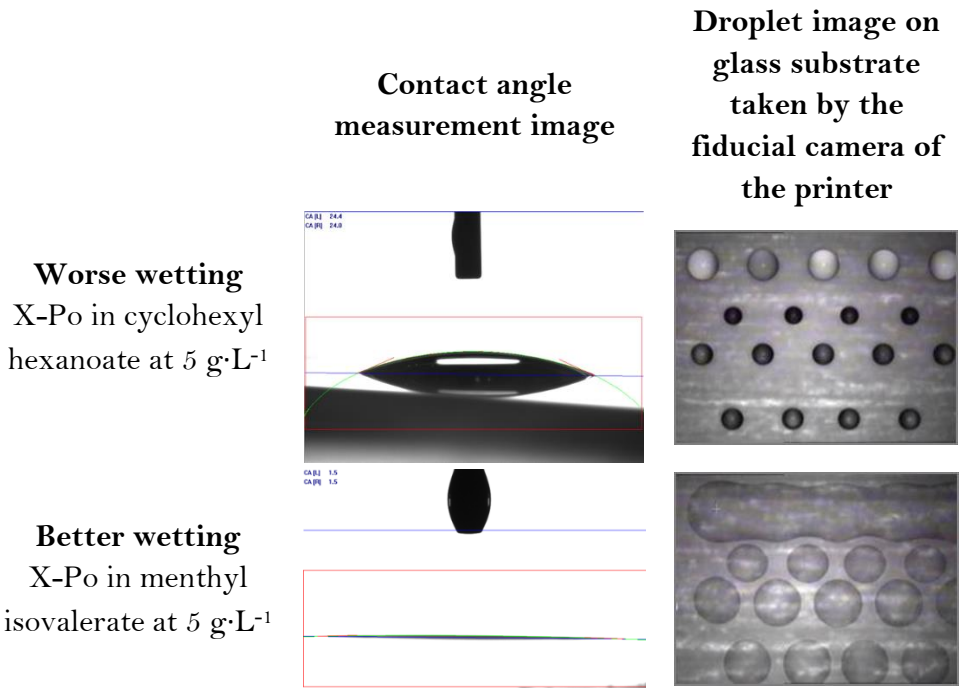

Figure 5.11: Ink wetting on glass substrate of X-Po inks from cyclohexyl hexanoate and from menthyl isovalerate at 5g·L^{-1}. (left) Picture of X-Po ink droplet dropped taken from the side, used to determine the surface tension of the ink. The baseline is blue; the drop outline is green and the tangent is red. (right) Picture of X-Po printed ink droplets taken from the fiducial camera of the printer. Different amounts of ink were printed. Four series were printed (from top to bottom): 30 pL, 10 pL, 20 pL and 20 pL.

Ink wetting on the substrate can be characterised by the droplet diameter on the substrate and by its contact angle with the substrate. The ink wetting guides the droplet spacing used to form a film. It must enable at least two droplets to merge. This upper limit of the droplet spacing is discussed in the following section. While printing, the print-head was kept at 500 µm above the substrate. The droplet velocity was set to be between 4 to 5 m·s^{-1}. These printing conditions ensure that the droplet velocity had no impact on the droplet wetting on the substrate.

Film formation

The film formation on a free surface depends on forces induced by the surface tension of the ink and the substrate.[131] To form a wet film, two ink drops on a glass substrate must merge together. Droplet spacing on a given substrate is influenced by the ink surface tension. A high surface tension ink requires a smaller droplet spacing than a low surface tension ink, as represented in Figure 5.12. So, for every combination substrate/ink, the minimum droplet spacing must be optimised to form a continuous wet film.

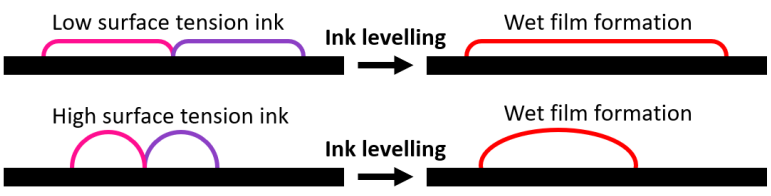

Figure 5.12: Schematic representation of ink wetting and drops merging resulting in wet film formation through ink levelling.

The droplet spacing can be decreased from this maximum value to reach thicker layers with only one ink formulation, i.e., ink concentration. However, due to drying behaviour, only a certain droplet spacing window, which is suitable for each combination substrate/ink, can lead to flat and smooth films.

Once the wet film is printed, slow solvent evaporation gives enough time to the film to level itself though capillary forces. These forces are responsible for a smooth and homogeneous film. However, while drying the solvent under vacuum, the film pattern faces formation instabilities such as the coffee-ring effect, responsible for poor lateral resolution and explained in Chapter 2.2.3. The solvent evaporates faster at the film sides, resulting in a material flow from the inside of the film towards the sides. In addition, a gradient of surface tension present across the film leads also to material flow towards the sides. This results in a inhomogeneous film thickness, where the sides are thicker than the centre of the film, see Figure 5.13.

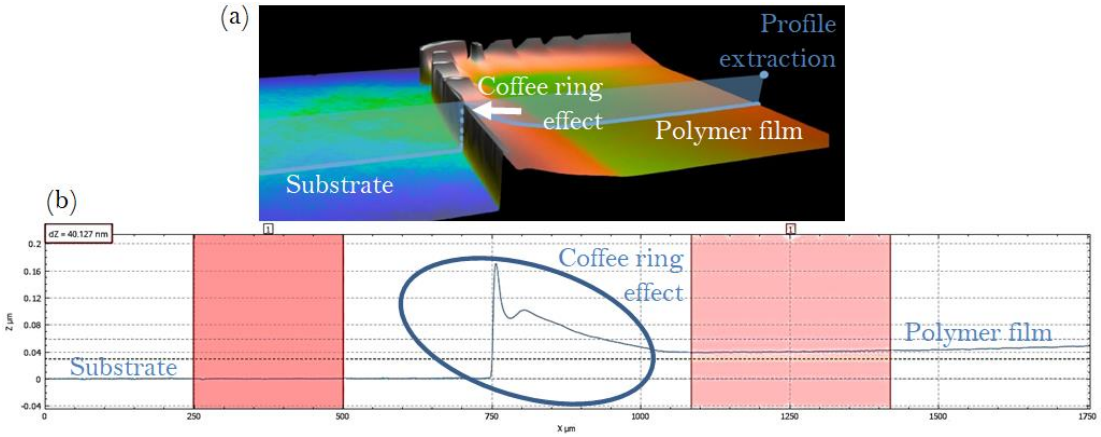

Figure 5.13: Interferometry picture and cross-section of a printed film demonstrating the coffee-ring effect. (a) 3D picture of the film corner where the coffee-ring effect is visible. (b) Cross-section of the same film, where the coffee-ring effect is identified by a blue circle.

Figure 5.14 shows the result of capillary flow leading to surface instabilities in inkjet printed films. The observed pattern is dependent on the droplet spacing, which corresponds to different amount of printed ink. This flow is due to surface tension gradients over the film and is intensified when the amount of ink is larger. The drying time increases with the amount of printed. In the vacuum chamber, a higher vapour pressure is reached when the amount of ink is larger, which reduces the solvent evaporation rate. This pattern formation is due to the flow of ink in the film which is stronger when more ink is printed. It limits the processing window of the inks to achieve flat and smooth film required for the cross-linking study in large area film.

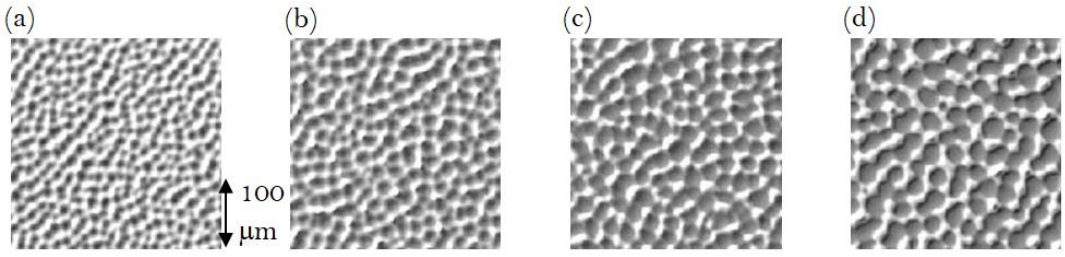

Figure 5.14: Thin film images taken by interferometry. X-Po films processed from MISO suffering of formation instabilities such as Marangoni and coffee-ring effect. The droplet spacing is (a) 30µm, (b) 35 µm, (c) 22 µm and (d) 20 µm in both x and y direction.

Solvent residue in cross-linked films

To process polymer X-Po from inkjet printing solvents, the polymer was first dissolved in a low viscosity solvent, then deposited in form of droplets by inkjet printing on a substrate and the solvent was removed by vacuum evaporation. During the vacuum process, as the solvent molecules evaporate from the wet film, the solvent concentration reduced substantially in the surface regime, i.e., at the interface film-air. The evaporation rate of the solvent then decreases exponentially as the drying proceeds.[132] This drying progression is responsible for a solvent concentration gradient in the polymer film. This is a diffusion-limited regime where the evaporation rate depends on the speed at which the solvent can diffuse through the high polymer concentrated surface. Thus, solvent molecules could be trapped in the film after vacuum drying. Further cross-linking process took place on a hotplate. In total, more solvent was evaporated under the vacuum treatment and most of the rest was removed during thermal annealing. Nevertheless, residual solvent molecules were still present in the film. It is commonly assumed that solvent residue in film is considered as impurities and can be harmful to film performance.

Solvent residue in cross-linked films: After vacuum dry

To investigate the percentage of trapped solvent molecules in dried films, X-Po was dissolved in 1-methylnaphthalene, 1-methoxynaphthalene, 3-phenoxytoluene, cyclohexyl hexanoate and menthyl isovalerate at 5 g·L^{-1}. Polymer solutions were poured inside a DSC pan in a volume of 30 µL, then placed in a vacuum chamber at a pressure of 10^{-4} mbar for two hours. The DSC pans were weighed before and after two hours of vacuum drying. The difference of masses indicates the portion of trapped solvent in the film, and is described as:

$$v_{ink} = \frac{m_{tot.i}}{d} \tag{5.4}$$

$$m_{poly} = \frac{v_{ink}}{c} \tag{5.5}$$

$$m_{s.rest} = m_f - m_{poly} \tag{5.6}$$

$$\%_{s.rest} = \frac{m_{s.rest}}{m_{tot.i} - m_{poly}} * 100 \tag{5.7}$$

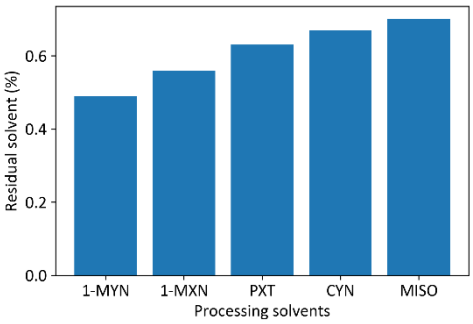

Figure 5.15: Trapped solvent in X-Po films after two hours vacuum drying determined by mass loss.

where v_{ink} is the ink volume of the wet film, $m_{tot.i}$ is the mass of the wet film, d is the density of the wet film, m_{poly} is the mass of polymer material, c is concentration of polymer in the ink, $m_{s.rest}$ is the mass of solvent residue in the film after drying and m_f is the mass of the film after drying. Figure 5.15 exposes that the amount of trapped solvent in the dried films varies depending on the ink solvent. X-Po solution from 1-methylnaphthalene shows 0.49 % of solvent trapped in the dried film, the lowest measured percentage. X-Po processed from 1-methoxynaphthalene, 3-phenoxytoluene and cyclohexyl hexanoate exhibit a higher percentage of solvent residue in film after drying of 0.56 %, 0.63 % and 0.67 %, respectively. The highest percentage of solvent residue in the dried film of 0.70 % was found for the

X-Po solution from menthyl isovalerate. So it can be concluded that solvent evaporation from a wet polymer film depends on the ink solvent and is directly correlated to the polymer-solvent affinity.[133-134] A *poor* polymer-solvent interaction such as X-Po and menthyl isovalerate favours a fast evaporation rate which leads to a high polymer density at the open surface and therefore traps more solvent in the bulk of the film. On the contrary, X-Po film from 1-methylnaphthalene, solvent exhibiting a *good* affinity to X-Po, tends to have a slower evaporation rate, thus the evaporation is constant over time due to the absence of a polymer density gradient in the drying surface of the wet film.

Solvent residue in cross-linked films: After annealing

In the actual process of fabricating an X-Po layer of an OLED, an annealing step followed the vacuum drying which is a second opportunity for the solvent to evaporate. A new method has been developed to investigate solvent residue in large area printed films after annealing with the objective to identify whether trapped solvent molecules remain in the film even after the annealing step. In this measurement, X-Po was processed from 3-phenoxytoluene on a glass substrate. The measurement procedure consists of placing the substrate inside a sample holder, with the face pointing down so that the X-Po film was directed toward the bottom (see Figure 5.16). 200 µL of toluene, a solvent miscible with the test solvent 3-phenoxytoluene, was poured into the sample holder which was then sealed to avoid solvent evaporation. After ten minutes, the solution was filled into a gas chromatographic vial to measure the amount of 3-phenoxytoluene found in the toluene solution (see procedure represented in Figure 5.16).

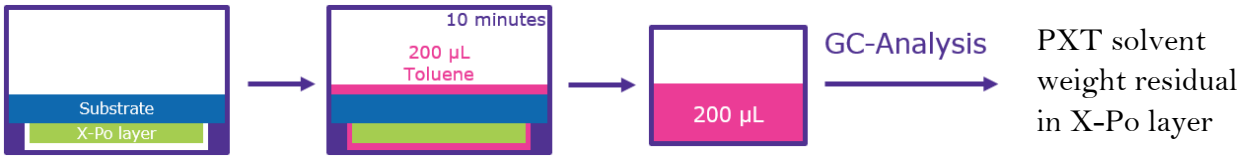

Figure 5.16: Newly developed measurement procedure to determine the solvent residue in X-Po film after the annealing step.

The amount of solvent residue is defined as the ratio of the residual solvent weight divided by the printed ink weight. Even though the GC method is very sensitive and permits the determination of nanograms, resulting in parts per million (ppm) solvent residue, the sample preparation reproducibility was not sufficient to rationalise deeper investigation. The only reasonable result was obtained from a printed film of X-Po from 3-phenoxytoluene being cross-linking at 225°C for 30 minutes. It led to a solvent residue in film between 5 ppm to 20 ppm in weight. For all the other solvents it is assumed that printed X-Po polymer films exhibit similar solvent concentrations of about 20 ppm in weight where the difference between solvents is smaller than the uncertainty in the sample preparation.

It can be concluded that after annealing and before subsequent printing, the five printed films are in similar conditions regarding solvent residue. There was no indication that solvent residue explains for any layer discrepancy in the performance of films processed from the tested solvents.

5.3.2. Stability of thin films against solvent exposure

One main challenge when studying the intermixing of subsequent solution-processed layers is the hidden nature of the resulting interface. Usually the stability of thin films against a subsequent solvent is tested by a rinsing test of spin coated films. By this procedure, the stability is characterised by the

percentage of the layer thickness left after solvent exposure. Solvent is dropped on the spin coated layer and is dried by spinning the solvent away. The thickness reduction corresponds to bulk removal and can be measured by profilometry, by interferometry or by ellipsometry. In the present case, the investigation was performed by a new technique of evaluating the film stability against solvent exposure, with experiments especially developed and adapted to study printed films.

Unlike rinsing tests performed by spin-coating, this unique approach allows the use of inkjet printing solvents. This is of great interest to understand the impact of solvents on interfaces in a printed device. In addition, the method mimics the intermixing process occurring between two printed layers, which does not correspond to bulk removal but rather to material mobility. To investigate the interface between an X-Po based HTL and an EML, X-Po ink was first printed onto a glass substrate, then dried under vacuum and subsequently annealed on a hotplate. A large area film of X-Po was made possible thanks to the knowledge developed about film formation detailed in Chapter 5.3.1. 90 pL of pure 3-phenoxytoluene solvent normally used to deposit the EML material was dropped by means of a print-head onto the X-Po based HTL. The droplet was left sessile on the layer and was subsequently removed by vacuum drying. Right after the contact between solvent and layer, capillary forces created by the droplet on the film guided the ink movement.[135] The solvent partially penetrated the layer and swelled it, respectively dissolved parts of the non-cross-linked polymer thin film.[136] This dissolved moieties were able to move in the liquid volume created by the solvent.[137-138] As a result, the wetted surface area piled up and solidified in the shape of a cone surrounded by a valley as can be seen in Figure 5.17. The layer change in topography is called deformation and is quantified to determine the HTL resistance against the EML solvent. The deformation height was extracted from the cross-section and is defined as the height difference between the peak and the valley.

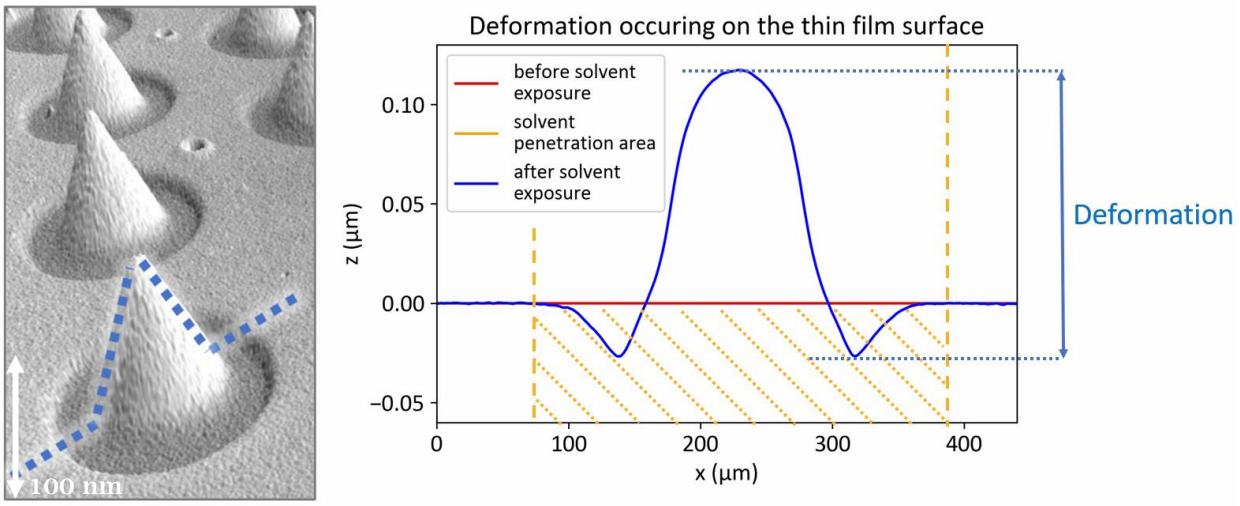

Figure 5.17: Surface deformation of X-Po film processed from 1-methylnaphalene caused by a 90 pL drop of 3-phenoxytoluene left on the film surface for five minutes and removed by vacuum drying. (left) Surface deformation observed by interferometry and represented as 3D picture. (right) Example of the cross-section of a typical surface deformation used to quantify the film stability against solvent exposure.

Differences in surface deformation were observed for layers processed from solvents either with strong affinity (1-methylnaphthalene) or weak affinity (menthyl isovalerate) to X-Po, see Figure 5.18. X-Po films processed from 1-methynaphthalene and from 1-methoxynaphthalene suffered from a deformation height of 98 nm and 100 nm, respectively, engendered by 3-phenoxytoluene drop exposure. 63 nm deformation was measured on X-Po film processed from 3-phenoxytoluene. The

smallest deformations were observed on films processed from cyclohexyl hexanoate and menthyl isovalerate and reached 10 nm and 13 nm, respectively, as can be seen from Figure 5.18.

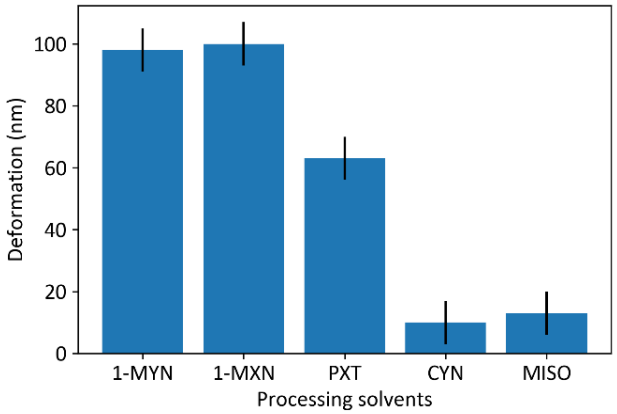

Figure 5.18: Deformation heights caused by 3-phenoxytoluene drop exposure on IJP polymer X-Po thin films depending on the ink solvent. The polymer films were 70 nm thick and were processed from 1-MYN, 1-MXN, PXT, CYX and MISO.

3D pictures of deformation of X-Po thin films are presented in Figure 5.19 depending on ink solvent used to process X-Po. From these results, it was discovered that the solubility of the thin film after being cross-linked depends on its ink formulation. X-Po processed from *poor* solvents provides stable films against solvent exposure, resulting in a smaller film deformation than in X-Po films processed from *good* solvents. This experiment teaches us about the impact of polymer-ink solvent interactions on thin film stability against a solvent used for a successive layer deposition. It is an inexpensive and quick investigation method giving an indication of a resulting interface sharpness with a subsequent EML layer. As introduced in Chapter 1 interface control is one of the main challenges for soluble processes since it has a significant impact on device performance.

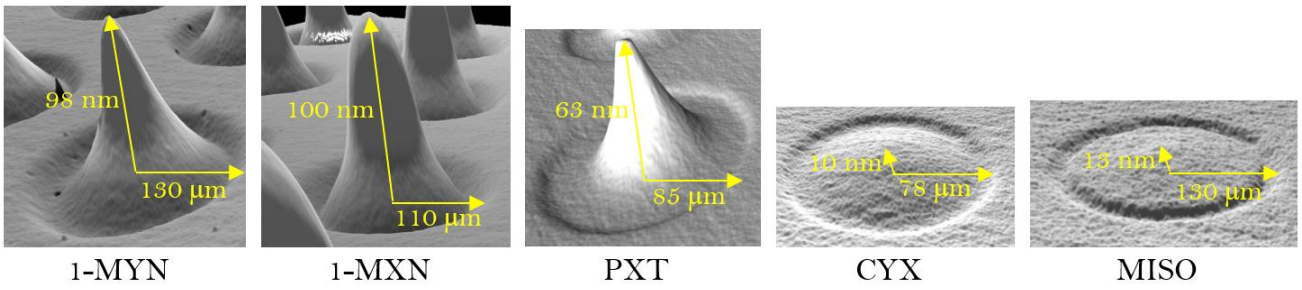

Figure 5.19: 3D pictures of the deformation visible on X-Po thin films processed from 1-MYN, 1-MXN, PXT, CYX and MISO caused by 3-phenoxytoluene drop exposure. The pictures were taken by interferometry. The polymer films were 70 nm thick.

The film deformation values presented in Figure 5.18 and 5.19 were obtained on films of 70 nm thickness. It was found that the deformation height was dependent on the original film thickness. Naturally, a thicker layer has more material than a thinner one. Therefore, there are more polymer chains likely to not be cross-linked and to participate to the film deformation. However, as Figure 5.20 demonstrates, the evolution of the deformation with the layer thickness is not linear for all ink solvents, the morphology of the polymer layer is more complicated. Nonetheless, the conclusion drawn for X-Po films of 70 nm remains valid for films down to 20 nm. Studying film stability against solvent

exposure of layers thicker than 40 nm allows for a clear differentiation of the results due to more distinctive values.

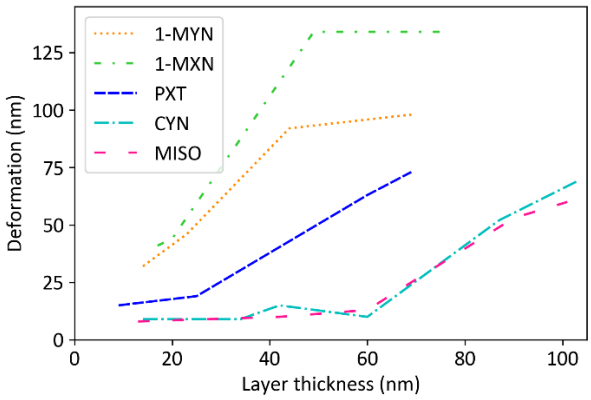

Figure 5.20: X-Po films deformation caused by 3-phenoxytoluene drop exposure on polymer films of various thicknesses.

3D pictures of the visible deformation on X-Po thin films processed from 1-methoxynaphthalene can be seen in Figure 5.21. X-Po films attained various thicknesses, from 53 nm to 105 nm, and the damages varied from 15 nm to 53 nm.

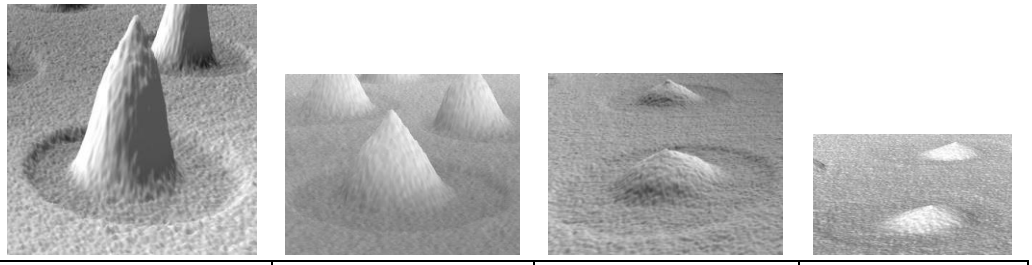

Layer thickness	105 nm	80 nm	70 nm	53 nm
Film deformation height	53 nm	33 nm	21 nm	15 nm

Figure 5.21: 3D pictures of the deformation visible on X-Po thin film processed from 1-MXN caused by PXT exposure. The pictures were taken by interferometry. The film deformation depends on the layer thickness.

Cross-linking of X-Po is thermally activated. Thus, one straightforward method to enhance the film stability against solvent exposure is to increase the annealing temperature. Toluene-based rinsing tests of spin-coated films of X-Po revealed that a treatment of 225°C for 30 minutes was sufficient for a complete cross-linking reaction in film. Therefore, a temperature of 225°C is used as a reference for the inkjet printed films of X-Po from 1-methylnaphthalene, 1-methoxynaphthalene, 3-phenoxytoluene, cyclohexyl hexanoate and menthyl isovalerate. However, it was found that annealing at the higher temperature of 250°C increased the film stability for all ink solvents, except 1-methylnaphthalene. The film deformation thereby reduced up to 50%. The actual film deformation after being exposed to 3-phenoxytoluene reduced from 92 nm to 64 nm when processed from 1-methoxynaphthalene, from 73 nm to 40 nm when processed from 3-phenoxytoluene, from 27 nm to 15 nm when processed from cyclohexyl hexanoate and from 34 nm to 15 nm when processed from menthyl isovalerate (see Figure 5.22). It can be concluded that a film processed from 1-methylnaphthalene requires more energy than the other films to improve its stability against solvent exposure since deformation height did not vary.

For example, a longer annealing duration should lead to a reduced film deformation after solvent exposure. 1-methylnaphthalene is the solvent exhibiting the strongest interaction with X-Po resulting in a poorly stable film against solvent exposure.

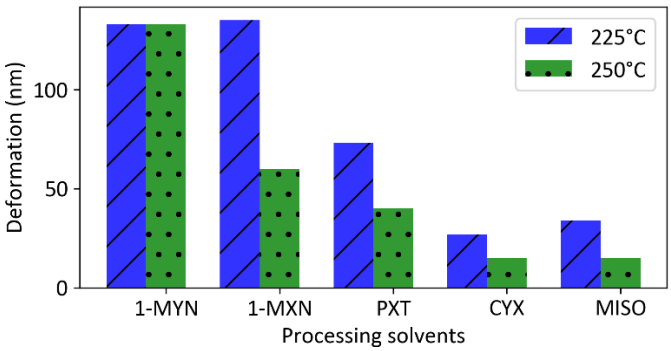

Figure 5.22: Film deformation following exposure to 3-phenoxytoluene on the 70 nm thick polymer films after annealing at different temperatures.

3D pictures of deformation of X-Po thin films depending on ink solvent and annealing temperature are displayed in Figure 5.23.

HTL annealing temperature	HTL processed from				
	1-MYN	1-MYN	PXT	CYX	MISO
225°C	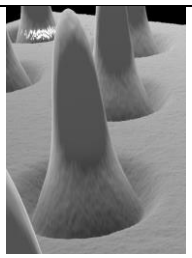	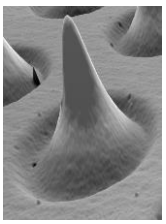	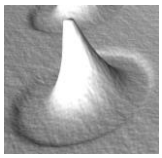	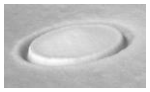	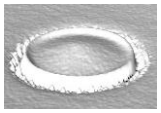
250°C	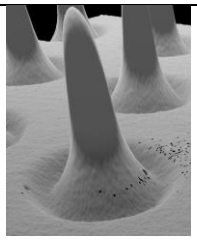	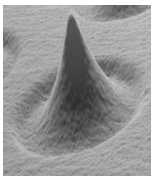	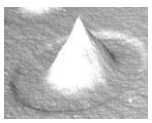	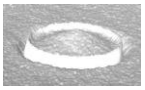	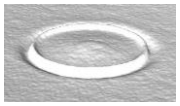

Figure 5.23: 3D pictures of the deformation visible on X-Po thin films processed from 1-MYN, 1-MXN, PXT, CYX and MISO and annealed at 225°C and 250°C, respectively, caused by PXT exposure. The pictures were taken by interferometry. The polymer films are 70 nm thick.

By these experiments, the difference of printed thin films depending on the ink solvent can be investigated and quantified. A direct correlation between ink solvent and thin film stability against solvent exposure was identified. Polymer films processed from *poor* solvents exhibit a smaller deformation after solvent exposure than polymer films of same thickness processed from *good* solvents for otherwise identical processes, i.e. the annealing temperature and duration. Thicker layers display a higher deformation than thinner layers of the same material and ink solvent. The film deformation can

be modified by the annealing process; a film annealed at a higher temperature is more stable against solvent exposure.

5.3.3. Degree of cross-linking

One possible way to influence the thin film stability against solvent exposure would be through influencing the cross-linking reaction, e.g., achieving a different degree of cross-linking completeness. DSC measurements were done to determine the degree of cross-linking in the investigated thin HTL films. Polymer solutions of 50 $g \cdot L^{-1}$ were poured inside a DSC pan in a volume of 30 µL. The pans were placed in a vacuum chamber and were exposed to a pressure of 10^{-4} mbar for two hours. The DSC thermograms of X-Po processed from all solvents were recorded from room temperature to 300°C using a heating rate of 20 $K \cdot min^{-1}$ and are displayed in Figure 5.24. Comparing the heat flow in the temperature window between 210°C and 260°C, clear differences between the different solvents are visible. From these thermograms, the cross-linking enthalpies of the X-Po films were determined and calculated by the integral of the heat flow curve from 210°C to 260°C, which is represented by the grey hatchings in Figure 5.24. A change in baseline is observed after the exothermic reaction due to a change in specific heat of the sample resulting from the cross-linking reaction.

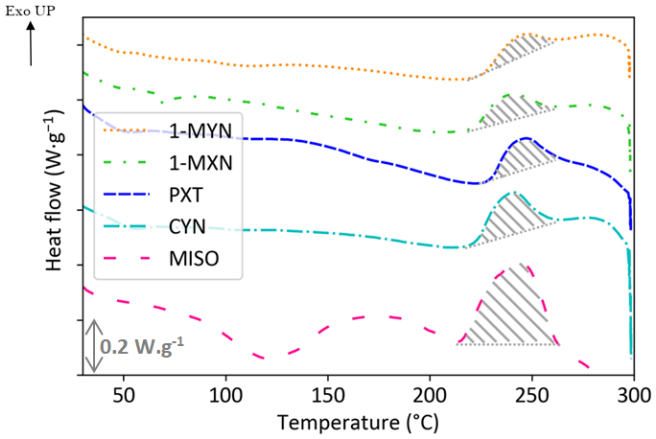

Figure 5.24: Cross-linking thermograms of X-Po in films measured by DSC from room temperature to 300°C. The area below the curve identified by the grey hatching was used to determine the cross-linking reaction enthalpy. An offset was applied to all thermograms for the sake of visibility. For the y-axis, each graduation corresponds to 0.2 $W \cdot g^{-1}$.

As a result, X-Po processed from menthyl isovalerate demonstrated the highest cross-linking enthalpy of 24.7 $J \cdot g^{-1}$ in film. On the other hand, the films processed from solvents like 1-methylnaphthalene and 1-methoxynaphthalene exhibited the lowest cross-linking enthalpies of 5.7 $J \cdot g^{-1}$ and 4.3 $J \cdot g^{-1}$, respectively. The cross-linking enthalpy for each film of X-Po is displayed in Table 5.3. In Chapter 5.2.3 it was shown that the cross-linking enthalpy could not be determined in solution, i.e., in the presence of a large amount of solvent molecules, since the solvent evaporation occurred in the same temperature window than the cross-linking reaction. Two hours of vacuum drying permitted to remove most of the solvent molecules (<1% solvent residue) from the DSC pan, as measured in Chapter 5.3.1, allowing for the interpretation of the DSC thermograms of X-Po films. Nonetheless, 0.47%, 0.56 %, 0.63 %, 0.67 % and 0.70% of solvent residues were found in X-Po films after vacuum drying and

processed from 1-methylnaphthalene, 1-methoxynaphthalene, 3-phenoxytoluene, cyclohexyl hexanoate and menthyl isovalerate, respectively. Films processed from menthyl isovalerate display the highest cross-linking enthalpy even though it is the film retaining the highest percentage of solvent after vacuum drying. So, it can be assumed that even higher cross-linking enthalpies could be reached in X-Po films processed from menthyl isovalerate if the drying process would be further optimised to retain the minimum amount of solvent possible. Trapped solvent in film is of importance for DSC measurements since the cross-linking enthalpy is determined by a single heat ramp from room temperature to 300°C at 20 K·min^{-1}. In a printed film, cross-linking occurs during 30 minutes at a constant temperature of 225°C. It was shown in Chapter 5.3.1 that after this annealing process the residual solvent concentration is similar, independent of the ink solvent. Thus, trapped solvent cannot explain the discrepancy of the cross-linking degree in printed films.

Thereby the degree of cross-linking of X-Po in films $X_{(Sx)}$ is established by the ratio between cross-linking enthalpy of the polymer in film ($\Delta H_{(Sx)}$) and cross-linking enthalpy in powder without solvent ($\Delta H_{(S0)}$). Thereby the cross-linking enthalpy $\Delta H_{(Sx)}$ is directly correlated to the cross-linking reaction density.[139] According to Lu and al.[140] it yields:

$$X_{(Sx)} = \frac{\Delta H_{(Sx)}}{\Delta H_{(S0)}} \tag{5.8}$$

Table 5.3: Comparison of cross-linking enthalpies and peaks of reaction of X-Po polymer powder and of X-Po films obtained from the five IJP solvent solutions after two hours vacuum drying, measured by DSC from room temperature to 300°C. The X-Po powder is used without solvent.

Film ink solvent	Cross-linking enthalpy [J·g^{-1}]	Peak of reaction [°C]	Normalised degree of cross-linking
1-MYN	5.7	241	0.12
1-MXN	4.3	248	0.09
PXT	6.4	246	0.14
CYX	9.4	241	0.20
MISO	24.7	246	0.53
X-Po powder without solvent	46.7	240	1

The impact of ink solvent on the degree of cross-linking of polymer X-Po is in accordance with what was observed in solution and assessed by ink viscosity measurement, see Chapter 5.2.1. The polymer solution prepared using *poor* solvents cross-link at lower temperature than polymer solutions prepared using *good* solvents. This result is paramount since it explains what happens in the X-Po film bulk when it is processed from various solvents. It brings a further understanding of the film stability experiment against solvent exposure. When processed from a *poor* solvent, X-Po reaches a higher cross-linking degree in film than a film processed from a *good* solvent. The high cross-linking degree awards an enhanced stability against solvent exposure to the film as demonstrated in Chapter 5.3.2.

5.3.4. Variation of optical properties

Optical properties of thin films can be related to their physical characteristics, since optical properties carry information about film thickness, composition and density.[141] Ellipsometry is a very sensitive and non-destructing measurement technique for optical properties of thin films. Using the spectroscopic ellipsometry over a broad range of wavelengths from ultraviolet to infrared increases the measurement options and more complex systems can be characterised.

In order to study the impact of the cross-linking degree on the polymer thin film optical properties, X-Po was processed from 1-methylnaphthalene, 3-phenoxytoluene and menthyl isovalerate on a quartz substrate to achieve a large area film (4 cm^2) of 70 nm thickness. These three ink solvents were chosen since X-Po showed the lowest/highest cross-linking degree in films processed from 1-methylnaphthalene/menthyl isovalerate, and a median value in films processed from 3-phenoxytoluene. After vacuum drying, the thin films were annealed at 160°C, 200°C and 225°C for 30 minutes on a hotplate to vary the cross-linking degree for a given ink solvent. After measuring thin film absorption in reflection and in transmission, the measured data were fitted with a special physical model of the fully cross-linked X-Po polymer. In this study, the spectra of inkjet printed films of X-Po were compared to the corresponding optical properties of a cross-linked X-Po spin-coated film, constituting the n and k constants. The spin-coated film was described as a one film with one refractive index n and one extinction coefficient k. The optical constants of X-Po cross-linked spin-coated films were known, and a model for X-Po was built from these films. The model was calculated from three X-Po spin-coated films after cross-linking at 225°C for 30 minutes. If the ink solvent does not have an impact on the optical properties of the printed film, all printed films should be describable by the model for the spin-coated films. To test this hypothesis, the existing model was used to fit each measurement of printed films, and the MSE was determined. The higher the MSE, the less meaningful is the model to describe the printed layer.

The calculated MSEs are reported in Figure 5.25. Considering that the films were transparent and non-rough, low MSE should be targeted. A maximum MSE value of 5 is considered to be a good value in this analysis knowing that the calculation runs over a wide range of wavelengths. When the thin films were annealed at 225°C, the MSE of X-Po thin films processed from 1-methylnaphthalene, 3-phenoxytoluene and menthyl isovalerate are approximately equal to MSE = 5. It can be concluded that after a heating treatment of 225°C, X-Po films processed from 1-methylnaphthalene, 3-phenoxytoluene and menthyl isovalerate exhibits a similar optical performance as a cross-linked spin-coated film.

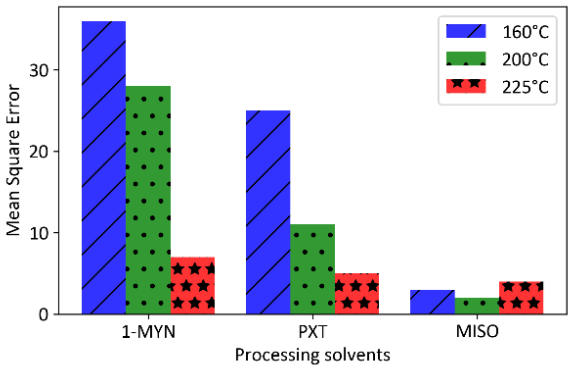

Figure 5.25: Mean square error calculated for X-Po thin films' absorption over wavelength range from 250 to 1000 nm. The thin films were processed from 1-MYN, PXT and MISO and were annealed either at 160°C, 200°C or 225°C.

A discrepancy of the results appeared between the ink solvents when the annealing temperature was lowered to 200°C and to 160°C. The MSE values of X-Po films processed from menthyl isovalerate are approximately equal to 5 for the three annealing temperatures. On the contrary, disparate MSE values were obtained in films processed from 1-methylnaphthalene and 3-phenoxytoluene for annealing temperatures of 200°C and 160°C. A strong increase of the MSE value is identified when the annealing temperature decreases. In films processed from 3-phenoxytoluene, the MSE values raise to 11 and to 26 for annealing temperatures of 200°C and of 160°C, respectively. The increase of the MSE values is stronger in films processed from 1-methylnaphthalene than in films from 3-phenoxytoluene. In films processed from 1-methylnaphthalene, the MSE values raise to 28 and to 36 for annealing temperatures of 200°C and of 160°C, respectively. When annealed at 160°C and 200°C, X-Po thin films processed from 3-phenoxytoluene and 1-methylnaphthalene have different optical properties than X-Po spin coated films annealed at 225°C. The conclusion is that the optical properties of X-Po inkjet printed films depend on the ink solvent from which the films were processed. It can be deduced that the three annealing temperatures do not impact the optical properties of X-Po films processed from menthyl isovalerate which are comparable to the optical properties of the X -Po spin coated films. On the other hand, annealing temperature appears to influence strongly the optical properties of X-Po films processed from 1-methylnaphthalene and from 3-phenoxytoluene. The ink solvent exhibits a strong influence on optical properties of X-Po films when annealed at 160°C and 200°C.

Employing ellipsometry is a powerful tool to understand the impact of cross-linking degree on the optical properties thin films (see Figure 5.26.). Films processed from a *poor* solvent, such as menthyl isovalerate, and annealed at 160°C up to 225°C, can achieve similar optical properties than a cross-linked spin coated film. Besides, films processed from a *good* solvent, such as 1-methylnaphthalene showed divergent optical properties from spin-coated films when the annealing temperature was set to 160°C and 200°C. Thanks to an annealing treatment of 225°C, the inkjet printed and cross-linkable films have the same optical properties than a spin coated film independent of the ink solvent.

In Chapter 5.3.3, it was revealed that X-Po reached a low cross-linking degree in films processed from a *good* solvent. It points out that the cross-linking degree tuned by ink solvent and film annealing temperature is related to the optical properties of the film. Non-fitting absorption spectra compared to the model derived for the spin-casted films demonstrates that the cross-linking degree is not as high as in a cross-linked spin-coated film, resulting in a change of the thin films' optical properties.

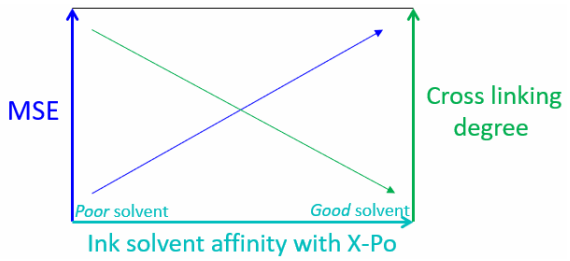

Figure 5.26: Impact of processing ink solvent affinity with X-Po on the cross-linking degree in film and on the calculated MSE value measured by ellipsometry. The MSE value characterises the difference between the model, describing a X-Po cross-linked spin-coated film, and the measured data for the Ψ and Δ values of X-Po inkjet printing films.

5.4. Conclusion on polymer cross-linking in bulk material and thin films

In this chapter, the cross-linking of X-Po was investigated in bulk material, in polymer solution and in thin films. Then, the impact of the cross-linking degree in film on the film stability against solvent exposure was studied as well as the impact on the optical properties of the film.

Infrared spectroscopy was used to analyse the cross-linking reaction of styrene units contained in X-Po. Due to the low proportion of styrene in the X-Po polymer chain, the signal strength was limited and the analysis was challenging. Therefore, polymer 7X-Po was investigated as 70% of its monomers contain a cross-linker (against 10% for X-Po). The enhanced styrene content of 7X-Po provides a distinct understanding of the styrene cross-linking reaction. The results support the mechanism discussed in the literature.[126] To quantify the cross-linking of X-Po, differential scanning calorimetry (DSC) was performed for the pure polymer. Thermogravimetric Analysis (TGA) revealed that the polymer does not undergo degradation until at least 300°C. The cross-linking of X-Po is an exothermic reaction with an enthalpy of 49 $J \cdot g^{-1}$, which was further considered as 100% of cross-linking.

Then, the cross-linking was studied as a dependency on the ink formulation. Polymer solutions were heated up to activate the cross-linking reaction while the cross-linker units were surrounded by solvent molecules. During cross-linking, polymer molecular weight and chain length increase which leads to an increase of the solution viscosity. Thus, the viscosity was recorded to monitor polymer cross-linking in solution by rheology. A polymer solution prepared using a *poor* solvent cross-linked at lower temperature than a polymer solution prepared using a *good* solvent. To investigate the cross-linking in solution at the nanometre scale, dynamic light scattering (DLS) measurements were performed. The variation of polymer size in solution measured by DLS is an indication that the cross-linking reaction took place. It was shown that after heat treatment, larger species were identified in all solutions except in the polymer solution from menthyl isovalerate. Cross-linking occurred even though no viscosity change was recorded. Nonetheless, these larger polymer chains are not present in a substantial volume. This correlates with the absence of viscosity change for some polymer chains. Quantifying the cross-linking in solution was tested with DSC. The presence of high boiling point solvents renders impossible the cross-linking analysis of X-Po since both reactions occur at similar temperatures.

Next, the cross-linking of X-Po was investigated in films. The layer stability against solvent exposure is determined by the variation of layer topography induced by a solvent drop on the layer surface for a given duration. The ink solvent of the HTL was identified to influence the HTL stability against subsequent solvent printing. Polymer films processed from *poor* solvents exhibit a smaller deformation after solvent exposure than polymer films of same thickness processed from *good* solvents for otherwise identical fabrication processes. To understand this stability discrepancy, the cross-linking degree in films was studied by DSC. The degree of cross-linking of the material was defined by the ratio of the cross-linking reaction enthalpy in film to the cross-linking reaction enthalpy of the pure powder without solvent. When processed from a *poor* solvent, X-Po reaches a higher cross-linking degree in film than a film processed from a *good* solvent. The high cross-linking degree awards an enhanced stability against solvent exposure to the film. The impact of the ink solvent on the cross-linking in film is in line with the trend observed in solution, where polymer solution prepared using *poor* solvents cross-linked at lower temperature than polymer solutions prepared using *good* solvents. Finally, the impact of the various cross-linking degree on film optical properties was studied. Optical properties are related to the film thickness, composition and density. Ellipsometry was used to measure the optical properties of printed X-Po. The measured data were compared to the optical properties of a

standardised spin-coated X-Po film, which was fully cross-linked. Films processed from a *poor* solvent achieved similar optical properties than a cross-linked spin coated film in the whole range of annealing temperatures. Films processed from a *good* solvent showed divergent optical properties from spin-coated films when the annealing temperature was lower than the reference temperature of 225°C.

In this chapter it was shown that a polymer solution made from a *poor* solvent cross-links at lower temperature than a polymer solution made from a *good* solvent. In films, high cross-linking degree was reached when the polymer X-Po was processed from a *poor* solvent and led to an enhance film stability against subsequent solvent printing.[142]

6. Inkjet printing of cross-linkable HTL in OLED devices

Cross-linkable hole transport layers are commonly used in OLED devices to render the layer insoluble to inks which are subsequently printed on top. The emissive layer is then deposited on the HTL without any risk of re-dissolving the layer. A complete cross-linking reaction in film ensures a stable interface in OLED devices processed from solution. In this last section, inkjet printing of HTL in a pixelated substrate and the formation of uni- and bipolar devices will be discussed. Finally, electrical and optical properties of OLED devices will be investigated for various ink solvents used for the HTL. In this chapter, the solvents acronym, presented in Table 3.3, will be used to identify the ink solvent instead of their complete name for ease of processing solvent comparison.

6.1. Inkjet printing of hole transport ink

For an HTL ink to be applied in an OLED device, its surface tension should allow the HTL ink to fully wet the pixel area. Low surface tension inks are preferred to reach full wetting. In addition, the resulting surface energy of the HTL layer after drying and annealing should allow the EML ink to fully wet its surface. This is of considerable importance to achieve homogeneous films resulting in uniform light emission across the pixel. Inhomogeneity, i.e., disparate thickness, will lead to localised stress in the pixel and thus will result in faster degradation during device operation.

Throughout the doctoral work, it was found that solvent used to print a given polymer can influence the resulting surface energy of the polymer film. Bipolar devices were built where the HTL ink solvent and the EML ink solvent were varied and a blue dye was used in the EML, according to the process presented in Chapter 3.3.2. The electroluminescent pictures of the OLED devices highlight the EML film formation discrepancy in dependence on the ink solvent of the HTL and of the EML, see Figure 6.1. In a pixel, the area where the EML is thicker results in a darker colour since the charge carrier transport through the thinner part appears brighter. Thus, the different EMLs show different film formation with an inhomogeneous thickness distribution. The different EML film formations for a given EML ink solvent on various HTL can be explained by its characteristic HTL surface energy.

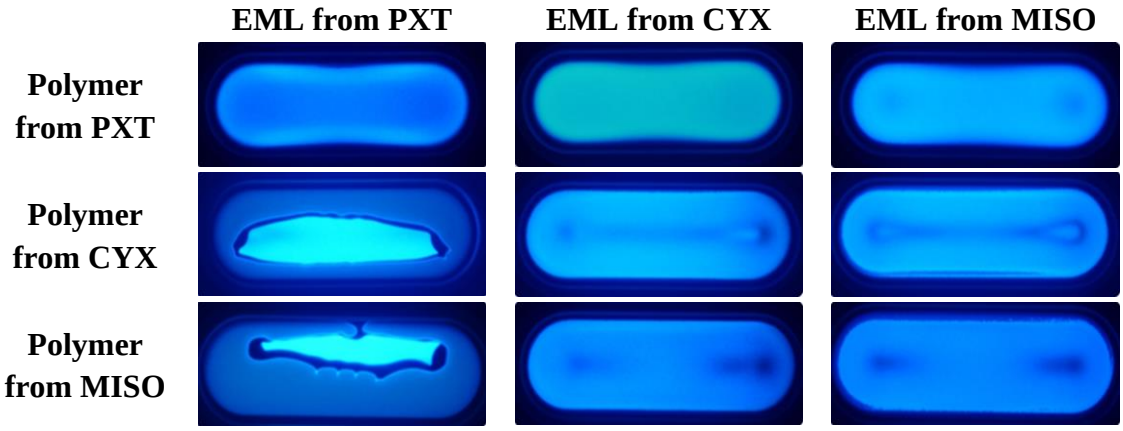

Figure 6.1: Electroluminescent pictures of OLED device subpixels taken at a luminescence of 1000 cd·m^{-2}. The HTL polymer was processed from PXT, CYX and MISO. On each HTL, an EML was processed from PXT, CYX and MISO.

Therefore, prior to the fabrication of OLED devices, the surface tension of X-Po inks and surface energy of X-Po films were investigated.

6.1.1. HTL surface energy

A film exhibiting a low surface energy is preferable as it offers good film wettability. Film wettability is ordinarily characterised by contact angle measurements. As introduced in Chapter 3.2.3, the contact angle is defined by the angle between the surface of the dropped liquid and the outline of the contact surface. The contact angle is labelled θ and an exemplarily taken picture by KRÜSS DSA100 is shown in Figure 6.2.

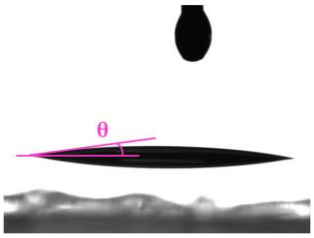

Figure 6.2: Photograph of contact angle measurement.

A sessile drop is used to determine the contact angle of a given solvent on a fixed substrate. This measurement technique is based on a macroscopic investigation of the interaction at the solid-liquid-air interface. The droplet diameter is usually greater than or equal to 1 mm which is larger than a printed droplet which exhibits a diameter of about 20 µm. In static contact angle measurement, the drop shape analysis software identifies the drop contour based on a grey-scale picture analysis. A mathematical model is chosen to describe the contour. It is recommended to use a circular arc for angles between 0-20°, an ellipse for 20-100° and a Young-Laplace-fit for angles of 100-180°. The software also performs a baseline recognition, which corresponds to the surface of the substrate. The contact angle is then calculated. For this study, a 15 µL drop of 3-phenoxytoluene was deposited onto five X-Po films processed either from 1-methylnaphthalene, 1-methoxynaphthalene, 3-phenoxytoluene, cyclohexyl hexanoate or from menthyl isovalerate. The equilibrium contact angles measured on each layer are reported in Table 6.1.

Table 6.1: Contact angle of PXT dropped on X-Po films processed from 1-MYN, 1-MXN, PXT, CYX and MISO. The results have an uncertainty of ±5° which was determined by multiple contact angle measurements of PXT on X-Po layers processed from MISO. The displayed value of PXT contact angle on X-Po layer processed from MISO is an averaged value over 6 measurements.

Processing solvents of X-Po layer	**1-MYN**	**1-MXN**	**PXT**	**CYX**	**MISO**
Measured contact angle of PXT on the polymer layer	14°	5°	6°	10°	9° (average value)

As can be seen, the determined contact angles are all lower than 14° for all HTL processing solvents. On the X-Po film processed from menthyl isovalerate, multiple measurements were performed, and a measurement uncertainty of 5° was determined which can be explained by the fact that these small angles are close to the detection limit. This can be explained by the determination of the baseline and drop contour which is based on a grey-scale picture whose resolution allows slight deviation from one

measurement to the following one. In addition, the measurements were performed at equilibrium whose visual determination can introduce errors. Therefore, it can be concluded that 3-phenoxytoluene shows a similar contact angle on all measured X-Po films. This contact angle is small and should ensure a very good wetting of the EML on top of the HTL. The tested processing solvents of X-Po do not change the surface energy of the polymer layer based on this macroscopic analysis.

Nonetheless, to produce OLED devices, the actual droplet size deposited onto the HTL layer is much smaller and is in the range of 10 pL exhibiting a diameter of about 20 µm. So, it cannot be excluded that the wetting of the EML, i.e., the droplet spreading, might behave differently during device fabrication. Although dosing systems which can dispense picolitre droplets exist.[143] These systems are usually very complex and the results hardly reproducible. To get a notion of the EML wetting onto X-Po films, a solvent droplet was dropped from the print-head and a picture of the droplet was taken by the printer camera right after landing. 3-Phenoxytoluene was chosen for the dropping solvent since it was used for the EML ink. By measuring the PXT droplet diameter, an understanding of the EML wetting can be obtained. As Figure 6.3 illustrates, PXT droplets on X-Po films processed from 1-MYN, 1-MXN, PXT, CYX and from MISO exhibit a similar diameter, indicating that the wetting of EML inks based on PXT must be comparable on all HTL layers.

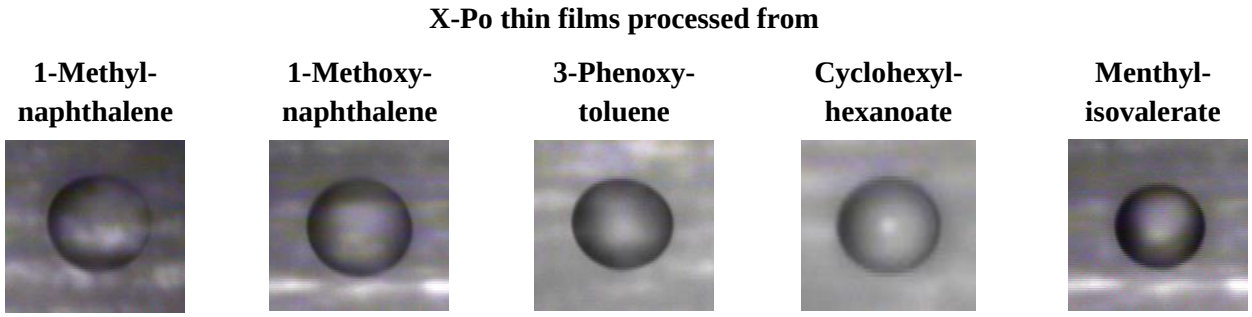

Figure 6.3: Pictures of 90 pL drop of 3-phenoxytoluene dropped onto X-Po films processed from 1-MYN, 1-MXN, PXT, CYX and from MISO. Pictures were taken by the printer camera.

6.1.2. EML film formation

The electroluminescence homogeneity of an OLED device depends on the homogeneity of the intra- and inter- subpixel layer profiles. It can lead to visual defects, also called mura, as well as to a low device performance.[98] Thereby it is of great importance that the multilayer stack is composed of flat and homogeneous layers. In addition, target thicknesses must be reached for each layer in order to achieve the best OLED performance. The thickness optimisation for each material system was investigated by spin coating the films. The HIL, the HTL and the EML target 40 nm, 20 nm and 80 nm, respectively. In this investigation, the ink concentration is analysed first to reach the film thickness in the appropriate range. Then, the desired thickness is reached by changing the number of drops deposited in a single subpixel for fine tuning.

Before fabricating OLED devices, the layer formation in the pixelated substrate was studied for the five X-Po inks and the two EML inks. X-Po was processed from 1-MYN, 1-MXN, PXT, CYX and from MISO. The polymers inks from 1-MYN, 1-MXN, PXT, CYX and from MISO required 8, 9, 8, 10 and 9 droplets, respectively, to reach a layer thickness of 20 nm. The waveforms were optimised to

jet droplets of 10 pL (±1 pL) reaching a speed of 4-5 m·s^{-1}. The EML was processed from PXT and from MISO. To investigate film profile formation in subpixels, profilometry was used as described in Chapter 3.2.3.

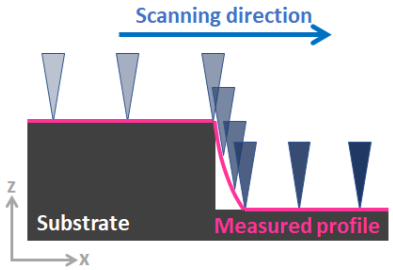

Figure 6.4: Schematic of the profilometer needle scanning a substrate exhibiting a substantial height change that can be assimilated to the subpixel banks. The needle is drawn at various times of a scan.

One artefact was observed by scanning a substantial height change at the bank sides. The needle scans a surface at a constant speed. When the needle reaches a substantial height reduction, the needle keeps moving in the scanning direction while reducing its height to reach the surface in the lower height. As a consequence, the measured profile on the left side of the bank shows a smooth and curved height changed as depicted in Figure 6.4, instead of revealing the sharp height change. On the opposite, when the needle meets a substantial height increase, the needle first hits the edge and then the height is adjusted while keeping a contact to the edge. Thus, in this configuration, the right side of the bank is better resolved.

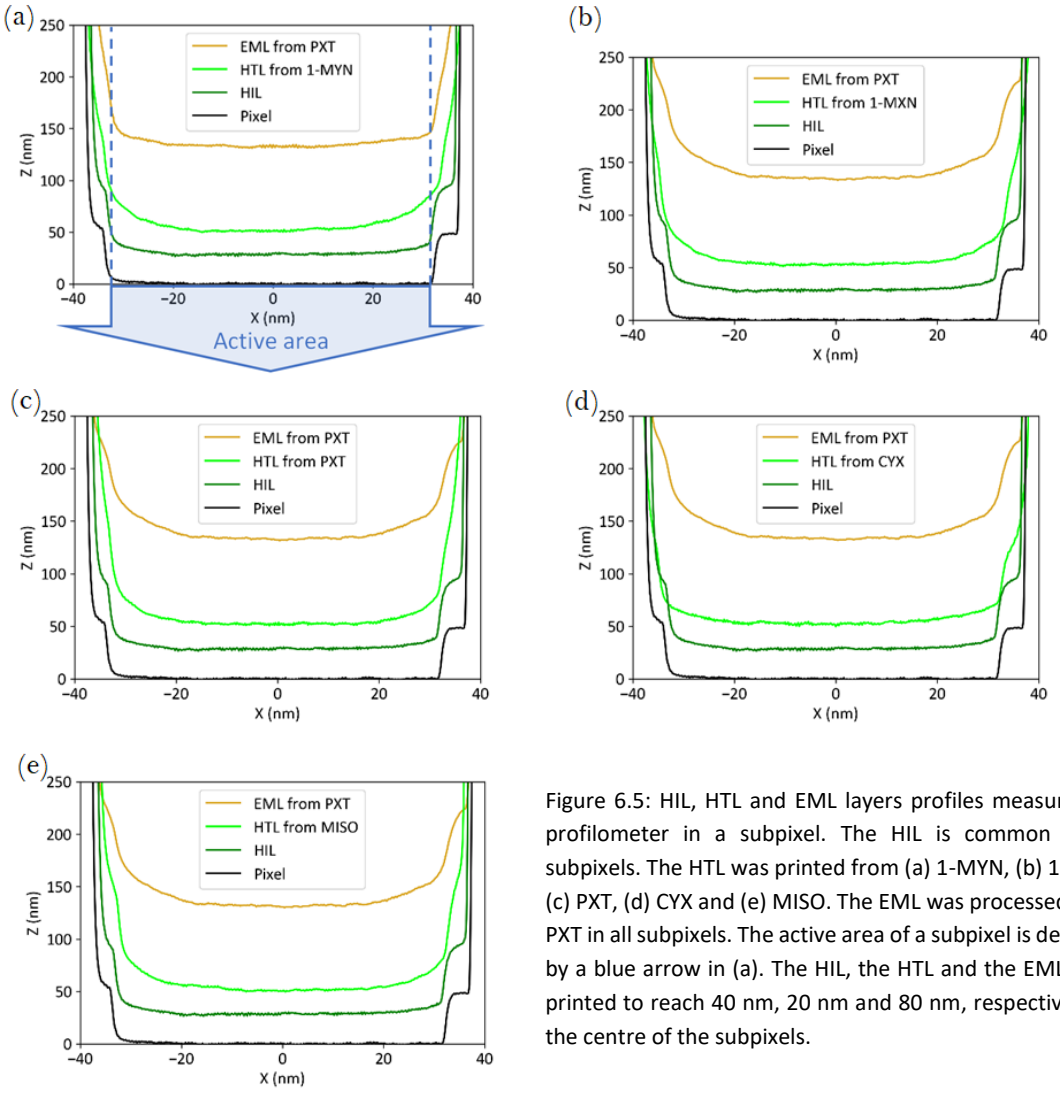

Figure 6.5: HIL, HTL and EML layers profiles measured by profilometer in a subpixel. The HIL is common to all subpixels. The HTL was printed from (a) 1-MYN, (b) 1-MXN, (c) PXT, (d) CYX and (e) MISO. The EML was processed from PXT in all subpixels. The active area of a subpixel is depicted by a blue arrow in (a). The HIL, the HTL and the EML were printed to reach 40 nm, 20 nm and 80 nm, respectively, in the centre of the subpixels.

In Figure 6.5 are presented the inkjet printed layers of HIL, HTL and EML measured by profilometry inside a subpixel. While for HIL and EML the same inks were printed for all profiles, the HTL processing solvent was varied. For clarity, each stack (HIL, HTL and EML) is displayed separately for each HTL processing solvent. From the profile representation, it can be seen that all HTL layers exhibit similar film formation on the HIL. As expected from the wetting test shown in Chapter 6.1.1, the EML ink from PXT reveals a comparable wetting on the five tested HTLs.

Additionally, a second EML ink based on MISO was investigated. MISO has a lower surface tension than PXT, which should lead to an ink wetting as good as or better than for the ink from PXT. Therefore, the EML wetting from MISO was tested only on one HTL, processed from PXT. In Figure 6.6 are represented the two EML layers printed on top of the HTL X-Po which was processed from PXT. After an optimisation of the solid concentration and the printing parameters, the two EML profiles are comparable. This enables them to be used for investigating the impact of the EML processing solvent on device performance.

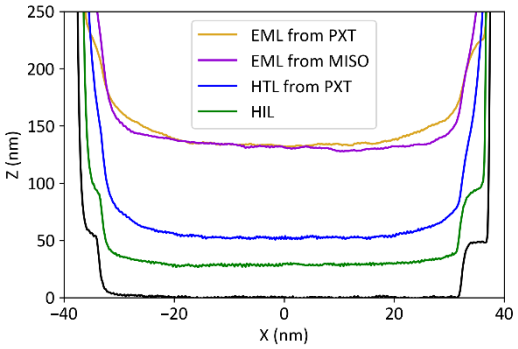

Figure 6.6: Comparison of EML profiles obtained by printing inks from PXT and MISO onto X-Po from PXT. The profiles were measured in a subpixel by profilometry.

6.2. Influence of hole transport ink on OLED devices

The ink solvent used for the HTL printing was shown in Chapter 5.3.3 to impact the cross-linking degree of X-Po in films. The hypothesis is that various cross-linking degrees lead to disparate film densities, thus different hole transport properties. In addition, the degree of cross-linking in a film dictates its resistance to solvent exposure. The direct impact of film stability against solvent exposure in a multilayer stack is the interface stability to the subsequently printed layer. When a film is not stable against solvent exposure, it intermixes with the following solution-processed layer. It is known that interface control is important for high and reproducible device performance. When it comes to the emissive layer, the interface with the HTL is crucial for hole-electron confinement and recombination to ensure high external quantum efficiencies.[144] Moreover, unreacted cross-linker molecules can act as radicals and may damage electrical properties of the OLED devices during electrical operation.[39]

6.2.1. Carrier mobility in HTL

To study the conductivity and mobility of X-Po, unipolar devices were built as described in Chapter 3.3.1. These devices are referred as hole-only devices (HODs). On one substrate, four pixels were measured allowing for some statistical analysis. The Ohmic behaviour of X-Po based HTL was

examined at low voltage and low current densities. In the Ohmic regime a variation in the current density of 2 to 3 orders of magnitude was found between three pixels of the same substrate. In this case the X-Po layer was processed from 1-MXN and annealed at 225°C, the current density changed from 0.002 mA·cm^{-2} to 0.2 mA·cm^{-2} at 1V, as can be seen in Figure 6.7. It means that the measured pixels of the same material, the same fabrication process, the same solvent produce strongly divergent J-V characteristics in the Ohmic regime. This very low reproducibility can be explained by leakage of the HTL layer leading to a low intrinsic conductivity. Physically that means that at low voltages the conductivity, defined as $\sigma = en\mu$, changes by two orders of magnitude. Here e is the elementary charge, n the charge carrier density and μ the charge carrier mobility. The origin of this leakage can be manifold: easy possibilities can be seen in the existence of pinholes which upon metallisation lead to conductive metallic whiskers through the layers or in the presence of chemical dopants through residual impurities in the utilised polymer and solvents.

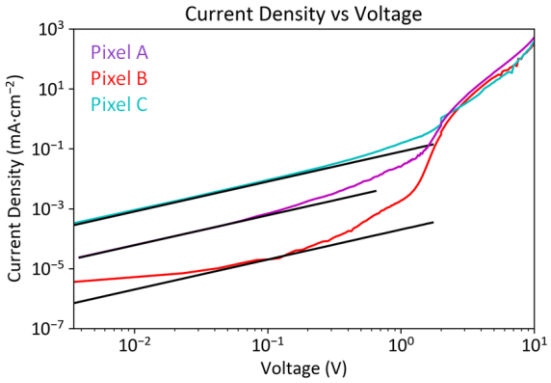

Figure 6.7: Current density vs voltage characteristics of HODs. The devices were built from 40 nm HIL films / HTL of 35 nm X-Po films from 1-MXN. The curves of the pixels (A in purple, B in red, C in cyan) and the linear fitting of n=1 are plotted on double logarithmic scales.

In order to reach the quadratic regime of space-charge-limited currents in the trap free regime, high voltages of up to 10V were applied to the HOD to use the Mott-Gurney law to determine the charge carrier mobility μ of the HTL. Unfortunately, in all reported I-V characteristics it was not possible to reach the required SCLC regime which prohibits the determination of the charge carrier mobility. The reason for not reaching the quadratic regime of the I-V curves is the existence of deep traps which are responsible for the steep increase in the I-V-characteristics following Ohm's regime.[145] Direct interpretation of the current–voltage characteristics, however, is difficult due to the absence of knowledge on the energetical trap distribution as well as on the injection and extraction barriers of the involved layers.[146]

6.2.2. Bipolar devices

Bipolar devices have a complex multilayer architecture and were built as presented in Chapter 3.3.2 using a green dye in the EML. It can be challenging to analyse the performance of bipolar devices since their different materials and interfaces are influencing device properties like luminous efficiency and device lifetime. Therefore, it was ensured that only such devices were compared, which differ from each other by only one parameter, allowing a reliable and straightforward analysis.

The bipolar devices fabricated in this doctoral work were aimed at reviewing the HTL/EML interface. Critical for luminous efficiency[35] and device lifetime, this interface can be influenced by various parameters including material for the HTL, the corresponding HTL ink solvent, the HTL annealing temperature, the materials for the EML, the EML ink solvent, the drying time, etc. Thereby it is

important to control and understand the interfacial structures of the multilayers because it is considered important to improve the OLED characteristics.[147] In order to pronounce the impact of the HTL/EML interface, the OLED devices were built so that the recombination zone is localised close to the HTL/EML interface. The OLED stack development to obtain the recombination zone next to the HTL/EML interface is the result of other people's work.[148]

HTL annealing temperature

X-Po is a cross-linkable polymer whose cross-linking reaction is activated by thermal energy. To investigate the impact of the cross-linking degree of the X-Po based HTL on OLED performance, the HTL was annealed at various temperatures for 30 minutes on a hotplate and tested in bipolar devices. The temperature range was chosen between 160°C and 260°C around the reference temperature of 225°C (explained in Chapter 5.3.2). In this investigation, the HTL was processed from PXT, a solvent exhibiting a medium strong interaction with the polymer in comparison to the other studied solvents of this work (see Chapter 4.1). The EML was also processed from PXT, which shows as a pure solvent also a medium deformation of the underlying HTL also processed from PXT (see Chapter 5.3.2).

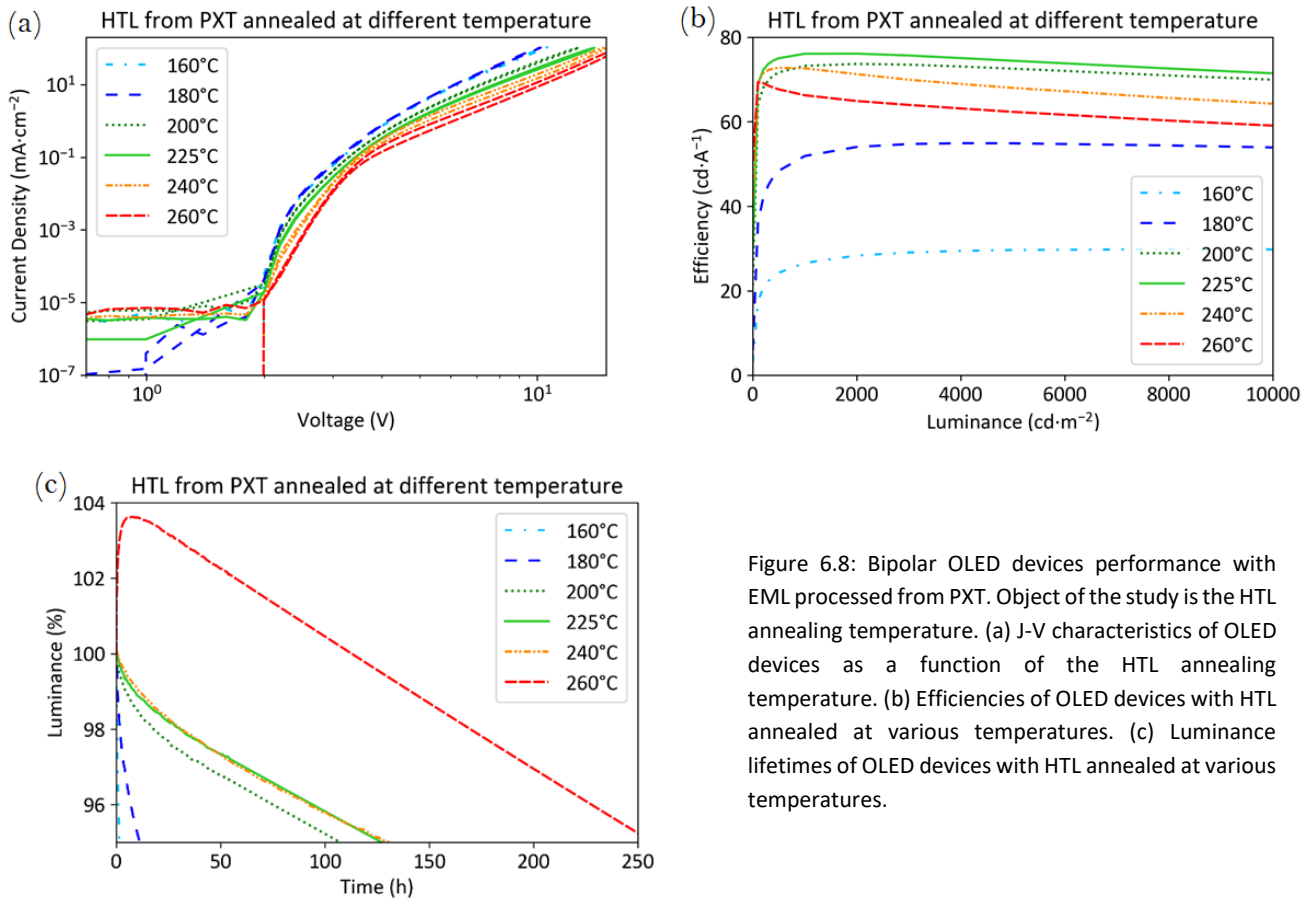

Figure 6.8: Bipolar OLED devices performance with EML processed from PXT. Object of the study is the HTL annealing temperature. (a) J-V characteristics of OLED devices as a function of the HTL annealing temperature. (b) Efficiencies of OLED devices with HTL annealed at various temperatures. (c) Luminance lifetimes of OLED devices with HTL annealed at various temperatures.

The influence of the HTL annealing temperature on OLED luminous efficiency, J-V characteristics and device lifetime performance is displayed in Figure 6.8. Devices comprising the HTL annealed at 160°C and at 180°C reveal the highest current densities of 100 mA·cm^{-2} at 10.4 V. As the HTL annealing temperature is increased from 180°C to 260°C, the driving voltage increases, as can be seen in Figure 6.8a. Devices with the HTL annealed at 260°C reach 100 mA·cm^{-2} at 16.5 V. A possible explanation can be seen either by changes in the hole transport properties, e.g., hole mobility of the

HTL due to increased cross-linking or by the formation of a higher injection barrier at the HTL/EML interface due to a more pronounced interface.[149] The luminous efficiency exhibits a different trend, as can be seen from Figure 6.8b. The lowest HTL annealing temperature lead to the lowest luminous efficiency among all measured devices with a value of 26.6 $cd \cdot A^{-1}$ at 1000 $cd \cdot m^{-2}$. An increase in HTL annealing temperature lead to enhanced efficiencies reaching a maximal value of 76.1 $cd \cdot A^{-1}$ at 1000 $cd \cdot m^{-2}$ for an HTL annealing temperature at 225°C. Above this temperature, the efficiency decreases slightly to 66.3 $cd \cdot A^{-1}$ at 1000 $cd \cdot m^{-2}$ for an annealing temperature of 260°C. In addition, the roll-off describing the decrease of efficiency with increasing luminance gets worse at the high temperatures. In Figure 6.8c the LT95 device lifetime, defined in Chapter 3.3.3, is plotted as a function of annealing temperature. It follows a similar trend as the luminous efficiency with temperature. Annealing of the HTL at 160°C results in a LT95 value of 1.5 h. An optimum LT95 device lifetime of 130h is obtained for the HTL annealed at 225°C and 240°C. The LT95 lifetime of the OLED built with the HTL annealed at 260°C is the largest of all investigated devices. Unfortunately, this record is only achieved due to a strong initial rise visible during the first 7h of operation which is not understood presently.

Since the HTL annealing temperature is directly correlated with the HTL cross-linking degree as was shown in Chapter 5.3.3, the OLED performance can therefore either be interpreted as being influenced by the HTL annealing temperature, or by the HTL cross-linking degree. The J-V characteristics are impacted by the HTL cross-linking degree due to an increasing polymer density and the removal of non-reacted cross-linker molecules with increasing temperature where latter can act as radicals or charge traps for holes. Such traps reduce the charge carrier mobility of holes and could be the reason for a shift of the recombination zone. In this respect Lee et al.[150] reported 2019 that the position of the recombination zone can influence the device lifetime of solution-processed OLEDs. The HTL cross-linking degree changes the stability of the cross-linked layer against subsequent printing. Consequently, during the OLED fabrication process, the EML processing solvent might cause the intermixing of the HTL and EML until the EML is dried. A stable HTL layer against the EML processing solvent ensures the formation of a sharp interface between HTL and EML and leads to a better confinement of electron-hole pairs within the emissive layer resulting in a higher recombination rate. The maximum luminous efficiency is achieved in OLEDs with HTL annealed at the optimum temperature of 225°C. Higher annealing temperatures may induce a damage of the polymer and therefore results in a lower device performance. For the lower annealing temperatures of 160 and 180°C higher current values are observed which probably result from charge carriers moving through the sample without recombination indicating a lower energy barrier between the HTL and EML. For OLED devices with an HTL annealed at temperatures above 225°C the current values decrease most probably to a higher energy barrier between the HTL and EML leading to a considerably higher luminous efficiency than the HTLs annealed at 160 and 180°C. The lifetime of the OLED devices also relates to the HTL cross-linking since the lifetime is sensitive to radical and chemical degradation during operation.[151] The LT95 stability increases up to 260°C annealing temperature, but only behaves similar until 240°C whereas at 260°C a strong initial rise obscures the interpretation.

HTL ink solvent

From the results obtained in Chapters 5.3.2 and 5.3.3, it is evident that the solvent used to process X-Po can tune the cross-linking efficiency of the polymer. Processing X-Po from a solvent, exhibiting a poor interaction with the polymer such as MISO, enables a high cross-linking degree in film resulting in a stable film against solvent exposure. The film stability was tested against the exposure of PXT,

which is also the EML ink solvent. It is also unequivocal that the hole transport material X-Po has a similar and high solubility in all investigated ink solvents, as demonstrated in Chapter 4.1.1. Moreover, the five tested HTL inks, i.e., X-Po dissolved in 1-MYN, 1-MXN, PXT, CYX and MISO, were processed in a way that they all produced comparable layer profiles and similar thicknesses. In addition, the boiling points of all ink solvents are very similar, and the residual solvent concentration after vacuum drying and annealing is considered to be similar and negligible in all films as seen in Chapter 5.3.1.

At first, OLED devices fabricated from different HTL ink solvents were investigated. Therefore, the printed HTL films were annealed at 225°C for 30 minutes before applying the EML processed from PXT. The luminous efficiencies obtained for these devices were similar and vary only within a small window between 74.3 cd·A^{-1} and 76.1 cd·A^{-1} at 1000 cd·cm^{-2} for all five HTL ink solvents, as can be seen in Figure 6.9a. The luminance lifetimes of these OLED devices are, however, different. The LT95 lifetimes vary between 74 h (HTL from MISO) and 150 h (HTL from CYX). However, this LT95 lifetime difference must be considered with caution since the reproducibility is poor. It can be concluded that the ink solvent of the HTL annealed at 225°C does not influence the OLED device efficiency. However, the lifetime characteristics suffer from poor reproducibility and display a weighted average lifetime of 121 hours. Thus, the LT95 varying from 74h (HTL from MISO) and 150 h (HTL from CYX) should not be further interpreted.

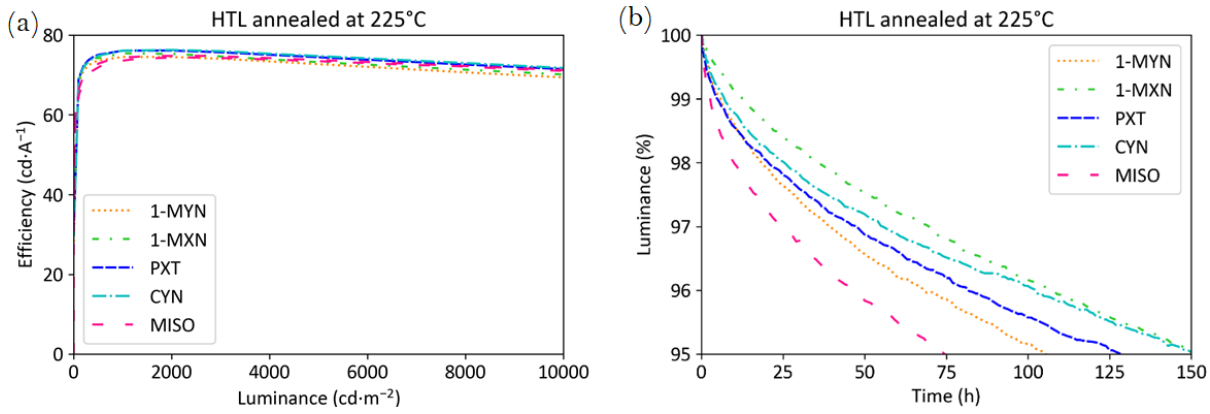

Figure 6.9: Bipolar OLED device performance with the EML processed from PXT. Object of the study is the impact of the HTL ink solvent in case of an HTL annealing temperature of 225°C. (a) Efficiency of OLED devices with the HTL processed from various solvents. (b) Luminance lifetime of OLED devices with the HTL processed from various solvents.

To further study the influence of the HTL cross-linking degree on the OLED device performance, the HTL was annealed at lower temperatures to pronounce the influence of the cross-linking for different solvents. The general influence of the ink solvents of X-Po on the cross-linking degree was already shown in Chapter 5.3.3. By lowering the annealing temperature of the HTL to 180°C, less energy is supplied for the cross-linking reaction and hence the difference in cross-linking degree between the HTL ink solvents should be enhanced. Nonetheless, by lowering the annealing temperature of the HTL, more solvent molecules could remain in the film. Besides the influence of the HTL ink solvent on the cross-linking degree, the solvent residue could also influence the cross-linking degree by allowing more movement of the polymer chains leading to a higher probability for the cross-linkers to react together. When the HTL printed layer is annealed at 180°C and subsequently the EML is processed from PXT, a clear efficiency discrepancy is visible among the five OLED devices, as can be seen in Figure 6.10a. The OLED efficiencies fluctuate between 20 cd·A^{-1} at 1000 cd·cm^{-2} achieved for

the device with the HTL processed from 1-MYN and 63 cd·A^{-1} at 1000 cd·cm^{-2} achieved with the HTL processed from MISO. Likewise, the OLED lifetimes exhibit a distinctive divergence among the five OLED devices. The LT95 lifetimes vary from 1 hour achieved for the device with the HTL processed from 1-MYN to 40 hours achieved for the device with the HTL processed from MISO.

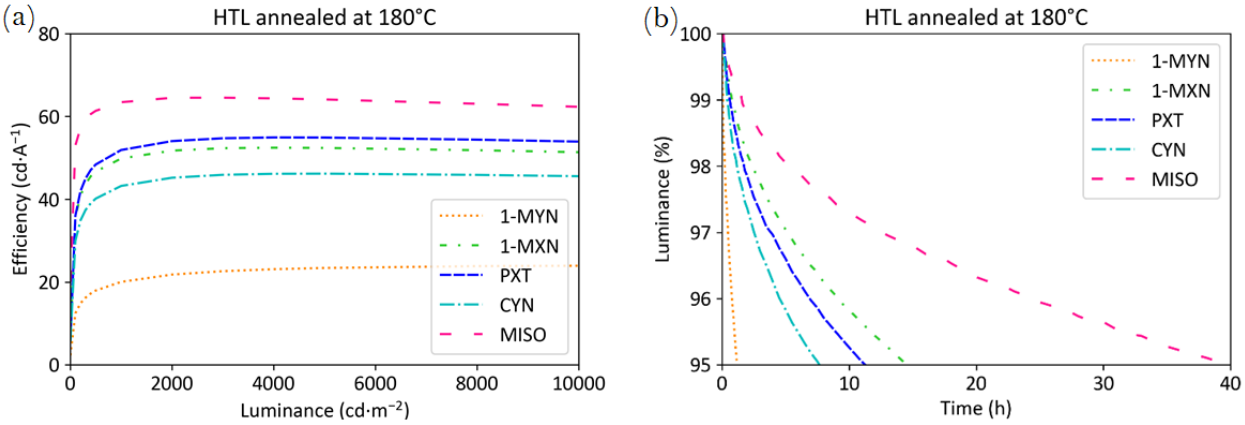

Figure 6.10: OLED performance in case of the EML being processed from PXT. Object of the study is to understand the impact of the HTL ink solvent when the HTL is annealed at 180°C. (a) Efficiency and (b) lifetimes of OLEDs in dependence of the HTL processing solvent as indicated.

For the solvents 1-MYN, PXT and MISO a correlation between the polymer-solvent interactions and the device performances can be drawn. It was shown that there exists a very strong polymer-solvent interaction between 1-MYN and X-Po meaning that 1-MYN is a good solvent for X-Po. This strong binding between 1-MYN and X-Po hinders a strong densification of the polymer chains and therewith the cross-linking. The result is a low efficiency and a low LT95 lifetime. This is different for the device with HTL processed from MISO. In this case MISO is a poor solvent and the binding of the solvent to the X-Po is weak and can be destroyed even at low temperatures. This leads to a strong densification and an efficient cross-linking. For MISO the efficiency is high and the LT95 lifetime is the longest. The other three solvents show intermediate behaviour in all respects: binding, efficiency and LT95. The results for the stronger binding solutions of X-Po with 1-MXN, PXT, CYX and MISO exhibit an increasing cross-linking degree and explain an increased film stability against solvent exposure probably resulting in a pronounced HTL/EML interface, a higher stability and a larger efficiency.

EML processing solvent

In this part of the thesis, interface conditions were interpreted in terms of stability of the HTL against a subsequently solution-processed EML on top of it. Interface stability can thereby be described as the capability to solution-process a subsequent layer without damaging the previous one. Besides the use of a cross-linked HTL, HTL stability against a solution-processed EML can also be achieved by the use of an EML solvent which shows a poor interaction with the HTL.[21-22, 152] Processing the EML from a poor solvent for the HTL polymer results in the absence of interaction between the EML solvent and the X-Po film while the EML is wet. In Chapter 4.1 it was confirmed that MISO is the solvent having the worst affinity with X-Po within the set of tested solvents. Nevertheless, MISO provides solubility enabling the dissolution of the emissive material at a concentration of 25 g·L^{-1}, which is sufficient to establish a target thickness of 80 nm in OLED devices in one printing step.

In Figure 6.11, the OLED performances of four devices are displayed. After processing the HIL X-Po was printed from 1-MYN, CYX, PXT and MISO. All HTLs were vacuum dried and annealed at 180°C

for 30 minutes as in the previous subchapter. An annealing temperature of 180°C was chosen due to the same reasons as before to concentrate on the cross-linking reaction by reducing the supplied thermal energy for the cross-linkers to react. The difference to the previous subchapter is that the EML was processed from MISO and not from PXT. The lifetime measurements of these devices are presented in Figure 6.11b. The four tested devices perform comparably, exhibiting LT95 values between 11h (HTL from 1-MYN) and 16h (HTL from PXT). The devices with the HTL processed from 1-MYN, PXT and CYX reveal almost identical luminous efficiencies, varying between 72.8 cd·A^{-1} (HTL from 1-MYN) and 74.0 cd·A^{-1} (HTL from PXT) at 1000 cd·cm^{-2} as can be seen in Figure 6.11a. One realises that the luminous efficiency of the device with the HTL processed from MISO only reaches 65.4 cd·cm^{-2}. The divergences of the efficiencies of the devices with EML processed from MISO are very low for all HTL solvents except MISO.

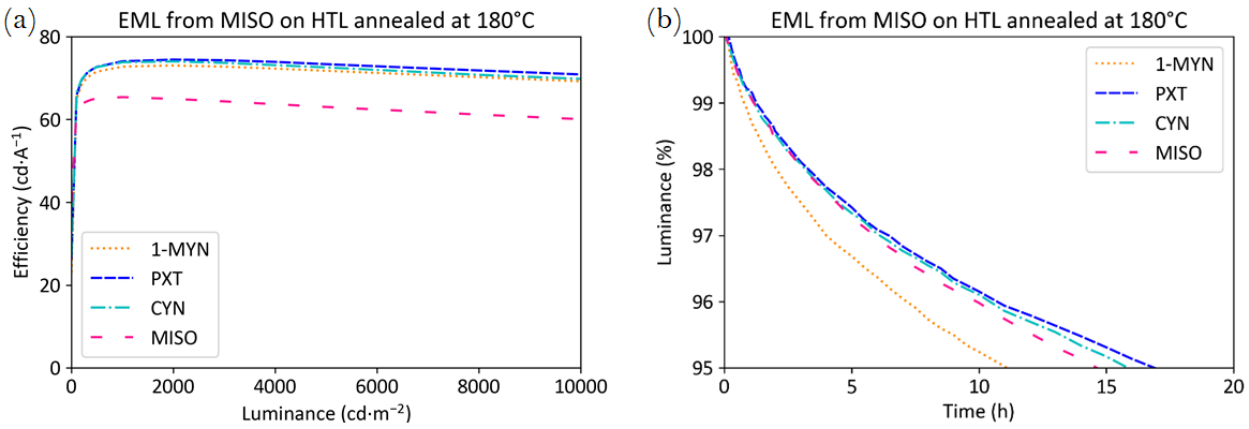

Figure 6.11: Performance of OLEDs where the EML was processed from MISO. Object of the study is the impact of the HTL ink solvent at an HTL annealing temperature of 180°C. (a) Efficiency of OLED devices with the HTL processed from various solvents. (b) Luminance lifetime of OLED devices with the HTL processed from various solvents.

In Figure 6.12, electroluminescence (EL) micrographs of four subpixels of the four OLED devices prepared from HTLs from different solvents and EML from MISO are shown. For ease of comparison, white frames were inserted into the EL pictures to mark the actual size of the emissive area. The sub-pixel corresponding to the MISO HTL (Figure 6.12d) appears smaller, especially due to the non-emitting boundaries at the rounded corners. This also explains the lower efficiency of the device with MISO prepared HTL in Figure 6.11a since a higher current is needed to reach 1000 cd·m^{-2}. This reduced light emission at the edges of the sub-pixel in Figure 6.12d compared to the other sub-pixels may be due to an inhomogeneous emissive layer profile in the subpixel potentially resulting from a different wetting or drying of the EML ink on the X-Po HTL processed from MISO.

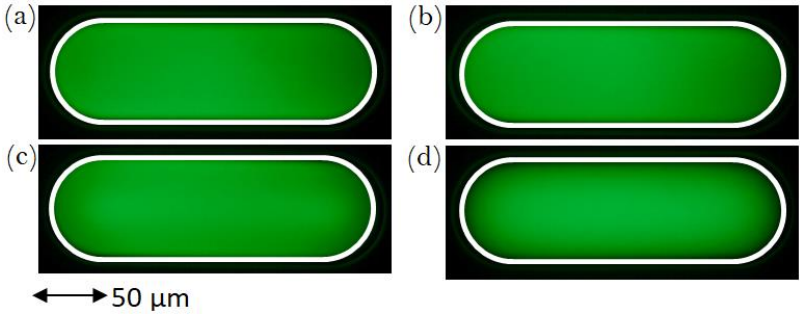

Figure 6.12: Electroluminescence photos of OLED devices taken by a microscope camera of single subpixels. The HTL of these devices was processed from (a) 1-MYN, (b) PXT, (c) CYX and (d) MISO. Pictures were taken at device luminance of 1000 cd·m^{-2}. White frames were added to better recognise the emissive areas of the four subpixels.

OLEDs where the EML was processed from MISO, a solvent exhibiting a poor interaction with the underlying X-Po layer, exhibited high luminous efficiencies in case of the HTL being printed from 1-MYN, PXT, CYX, despite the low HTL annealing temperature of 180°C. In contrast, when the EML was processed from PXT, a solvent showing a medium interaction with the X-Po HTL, a 180°C annealing temperature for the HTL was demonstrated as being harmful to the device performance. In Figure 6.13 a direct comparison between the luminous efficiencies reached in OLED devices with the HTL being processed either from PXT and annealed at 180°C and 225°C, or the EML being processed from PXT and MISO is displayed. As can be seen, the use of a poor solvent for the HTL for processing the EML ensures a constant luminous efficiency of the OLED device independently of the chosen HTL annealing temperature (180°C or 225°C).

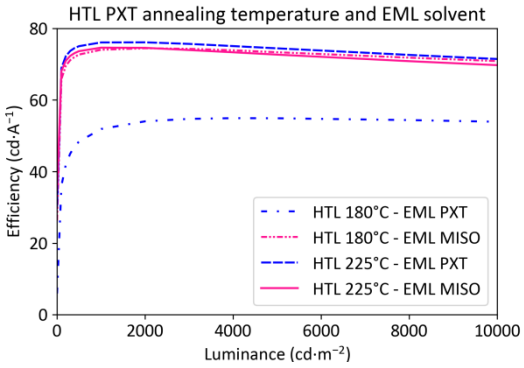

Figure 6.13: Impact of EML ink solvent on OLED performance in case of the HTL processed from PXT and annealed at either 180°C or 225°C.

6.3. Conclusion on cross-linking HTL in OLED devices

In this chapter, the polymer inks were printed in a pixelated substrate to build uni- and bipolar devices. To characterise the electrical and optical properties of OLED devices, all layers must achieve homogeneous film thicknesses enabling uniform light emission across the pixel. Inhomogeneity leads to localised stress in the pixel and thus results in faster degradation during device operation. Therefore, the HTL film formation was optimised to obtain flat and smooth films. Contact angles were measured on large area HTL films to anticipate the EML wetting. The two investigated EML inks exhibited comparable profiles, which enable them to be used for investigating the impact of the EML ink solvent on device performance.

After the profile optimisation, unipolar devices were built to study the impact of the cross-linking degree of X-Po in films on the hole transport properties. Moreover, unreacted cross-linker molecules can act as radicals or traps and may harm electrical properties of the OLED devices during electrical operation. In the Ohmic regime at low current densities, it was found that pixels of the same material, the same fabrication process, and the same solvent produce strongly divergent J-V characteristics. In order to determine the hole mobility μ within the HTL, the quadratic regime of space-charge-limited currents in the trap free regime must be reached. Unfortunately, in all reported I-V characteristics it was not possible to reach the required SCLC regime due to the existence of deep traps which prohibit the determination of the charge carrier mobility.

The impact of the HTL ink solvent was investigated in bipolar devices with the aim of reviewing the HTL/EML interface, critical for luminous efficiency and device lifetime. In the previous chapter a correlation was shown between the ink solvent and the cross-linking degree in film resulting in distinct

film stabilities against specific solvent exposure. The direct impact of film stability against solvent exposure in a multilayer stack was the interface stability to the subsequently printed layer. When a film was not stable against solvent exposure, it intermixed with the following solution-processed layer. It was shown that the cross-linking degree can be varied by the annealing temperature; the higher the annealing temperature, the higher was the cross-linking degree. The maximum luminous efficiency was achieved in OLEDs for HTL annealed at the optimum temperature of 225°C. Higher annealing temperatures induce damage to the polymer or to the other layers and therefore resulted in a lower device performance. On the other hand, lower annealing temperatures exhibited higher current densities explained by lower energy barriers between the HTL and EML. The lifetime of the OLED devices also related to the HTL cross-linking degree since the lifetime is sensitive to radical and chemical degradation during operation. The cross-linking degree was shown to considerably influence the luminous efficiency of OLED devices. The second attempt to enhance the cross-linking degree was performed by varying the HTL ink solvent. It was shown that the ink solvent of the HTL annealed at 225°C did not influence the OLED device efficiency. To deeper understand the cross-linking conditions, the HTL were annealed at 180°C, where less energy was available for the cross-linking reaction to occur. In this case HTLs processed from *poor* solvents exhibited higher luminous efficiency and a longer lifetime than HTL processed from *good* solvent. This can be explained by the high cross-linking degree reached in film from *poor* solvents resulting in an energetically steeper HTL/EML interface, a higher stability and a larger efficiency. Finally, OLED devices were built where the EML was processed from a solvent exhibiting a poor interaction with the underlying X-Po layer. A stable HTL/EML interface was expected since no interaction should occur between the subsequent solution-processed films. Higher luminous efficiencies were attained when the HTL was annealed at 180°C and when the EML was processed from a solvent showing a poor interaction with X-Po than when processed from a solvent with a medium interaction with X-Po.

The HTL ink solvent was demonstrated to have a strong influence on OLED device performance when the HTL was annealed at 180°C. *Poor* solvent insured a stable HTL against subsequent EML printing resulting in high luminous efficiency and longer lifetime. In addition, the EML ink solvent was shown to impact the OLED efficiency. Processing the EML from a solvent showing a poor interaction with the HTL improved the device performance when the HTL was annealed at 180°C.

In this chapter, it was shown that the hole conductivity within the HTL suffered from low reproducibility. Due to deep traps, the determination of the hole mobility was not achieved through I-V characteristics of unipolar devices. An annealing temperature of 180°C was used for the HTL to demonstrate the impact of the HTL polymer-solvent affinity on the electrical properties of bipolar devices. HTL processed from *poor* solvent exhibited higher luminous efficiencies and longer lifetimes than HTL processed from *good* solvent. The same was found for the EML, where higher luminous efficiencies were achieved when the EML was processed from a solvent showing a poor interaction with the HTL.

7. Summary

Interfaces, their definition, characterisation and controlled generation are studied intensively in various semiconductor devices having a multilayer architecture. Furthermore, not only in OLEDs, but also in OPVs and OFETs, solution processes are attractive in research laboratories and on the market. To ensure a stable layer against a subsequently solution-processed layer, various methods have been reviewed in the literature. This thesis focused on the use of cross-linked polymers, with a styrene cross-linker whose reaction is thermally triggered. To process this material, inkjet printing is the method of choice since it is a promising technology for high resolution displays. The aim of this work was to examine the influence of the ink solvent on the layer stability against subsequent printing and its impact on OLED device performance.

Prior to the investigation of the polymer ink and the resulting layers, a set of five solvents suiting the inkjet printing process was defined covering the relevant parameter space of surface tension, viscosity and boiling point. The solvents were described by the interaction with the investigated polymer X-Po. That way, the learnings can be applied to any set of material and solvent by a simple interaction characterisation. The affinity of X-Po with the ink solvent was characterised by experiments as well as empirical observations based on the Mark-Houwink parameters, the Huggins and Kramer constants, and the Solomon Ciuta equation. The intrinsic values of X-Po in the five tested solvents varied between 0.61 and 0.74 $L \cdot g^{-1}$ which due to their similarity hinders the identification of a preferred solvent for X-Po. On the opposite, Huggins and Kraemer constants identified 1-MYN as *good* solvent for X-Po, and PXT, CYX and MISO as *poor* solvents for X-Po. To enhance this differentiation among the five solvents, an experimental setup was developed based on the non-solvent induced phase separation (NIPS) method. By this developed technique, the strength of interaction between the polymer and the solvents were classified from the strongest to the weakest as: 1-MYN, 1-MXN, PXT, CYX and MISO. The trend observed by Huggins and Kraemer constants is in agreement with the experimental result of polymer-solvent interactions. Flory and Fox as well as Einstein equation revealed a similar radius of gyration of X-Po in the five solvents of 1.3 nm (±0.8 nm). DLS measurements could not experimentally confirm or disconfirm these results since experimental limitations were met at low concentration and unfortunately no relevant signal could be detected.

The styrene cross-linking reaction mechanism, already reported in patents,[126] was characterised in this work by DSC and FTIR. Due to the low content of styrene in the X-Po chain (10 %), direct analysis of the X-Po IR absorption was inconclusive. An increase of the cross-linking group by a factor of seven provided, however, a distinct understanding of the styrene cross-linking reaction and allowed for a further interpretation of the X-Po cross-linking reaction. DSC turned out to be an appropriate method to describe the exothermic reaction of styrene whose enthalpy attained 49 $J \cdot g^{-1}$ and the maximum heat flow was reached at 240°C.

Cross-linking was then studied in solution made from X-Po in 1-MYN, 1-MXN, PXT, CYX and MISO at 50 $g \cdot L^{-1}$ and was triggered by heating the solutions to different temperatures for three hours. Rheology measurements were carried out to track the cross-linking reaction of X-Po in solution and gave an evident indication of macroscopic changes. A heat treatment of 170°C and 180°C was enough to cross-link the polymer solution prepared using MISO and CYX revealing a fast reaction in these otherwise *poor* solvents. On the opposite, X-Po in 1-MYN and 1-MXN did not reveal any viscosity

variation independent of the temperature treatment. DSL measurements showed the presence of cross-linked polymer chains where rheology could not identify viscosity variations thanks to its higher sensitivity. The DLS results complemented the rheology measurements and a complete investigation of the cross-linking reaction in solution at the nanoscale up to the macroscopic scale was possible. A polymer solution prepared from a *poor* solvent cross-linked at lower temperature than a polymer solution prepared from a *good* solvent.

The impact of ink solvent on the degree of cross-linking of X-Po measured by DSC was in accordance with what was observed in solution and assessed by ink viscosity measurements. When processed from a *poor* solvent, X-Po reached a higher cross-linking degree in film than a film processed from a *good* solvent. The high cross-linking degree awarded the film of a stronger stability against further solvent exposure. A direct correlation between ink solvent and thin film stability against solvent exposure was identified. Polymer films processed from *poor* solvents exhibited a smaller deformation after solvent exposure than polymer films of same thickness processed from *good* solvents for an otherwise identical fabrication process. Thicker layers generally displayed a higher deformation than thinner layers of the same material and ink solvent. The film deformation could also be influenced by the thermal annealing process. A film annealed at higher temperature was more stable against solvent exposure.

To study the impact of ink solvent on the electronic properties of printed layers, uni- and bipolar devices were processed. Hole-only devices were built to determine the charge mobility within an X-Po HTL by space charge limited current (SCLC) techniques. In order to obtain reliable values for the mobility the quadratic regime of the I-V characteristics of SCLC must be reached. Therefore, high voltages were applied to the HODs. Unfortunately, the SCLC regime could not be attained. Light emission obscured the HODs behaviour due to injection of negative charges from the cathode destroying the conditions for SCLC. Therefore, the charge mobility within the HOD could not be determined. Finally, bipolar OLED devices were printed from various HTL inks. For the solvents 1-MYN, PXT and MISO, a correlation between the polymer-solvent interactions and the device performances could be drawn. OLED devices fabricated with HTL processed from *poor* solvent resulted in enhanced luminous efficiency as well as longer device lifetimes. This could be explained by an increased film stability against solvent exposure guaranteeing a stable HTL/EML interface resulting in a better confinement of electron-hole pairs within the emissive layer in favour of a higher recombination rate.

The importance of IJP solvent choice to fabricate a stable cross-linked polymer film was successfully demonstrated. This study demonstrates that the solvent selection is a critical parameter to enhance the full potential of OLED materials in devices. Tuning the degree of cross-linking of a polymer thin film resulting in different intermixing levels between successive layers is of general interest for multilayer structures. The developed solvent exposure stability test is generally applicable and can be of interest for other fields of activity, such as in the investigation of large area cross-linking homogeneity.

8. Outlook

As OLED device architectures become more and more complex, interface study and film properties will remain a focus and additional steps will have to be taken to advance the research on that topic. Of prime importance will be to evaluate the taken measures on a larger and even broader set of solvents, in order to identify the limits of polymer-solvent interaction resulting in stable inks but also in functional thin films. As an additional experimental technique to be used in the future, thin film stability against solvent exposure as reported in literature could use atomic force microscopy (AFM). After solvent exposure, morphology and layer thickness could be analysed to judge the efficiency of cross-linking or orthogonal solvents by AFM.[50] Also a mechanical characterisation by nanoindentation through AFM could be used.[153] Independently of the choice of the measurement method, further efforts should aim on the influence of ink solvent on cross-linking efficiency in films or devices. Solvent mixtures could be a next step toward a full understanding of the importance of solvent development and choice for solution processes.

In this thesis, one limitation was met concerning the visualisation of the buried interface between two layers. No depth profile was drawn along the multilayer stack to picture the learnings made by the various experiments on the layer stability against subsequent printing. Interface visualisation was demonstrated by various methods. Michael Bruns of Karlsruhe Institute of Technology presented a technique to measure depth profile of atomic concentration by x-ray photoelectron spectroscopy (XPS).[154] Depth-profiling analysis was also performed by time-of-flight secondary ion mass spectrometry (TOF-SIMS) involving ion beam etching.[155] Evaluation of interfaces were reported using neutron reflectometry (NR),[156] impedance spectroscopy (IS) and ultraviolet photoelectron spectroscopy (UPS).[149] However, these methods require long measurement times inhibiting the investigation of a large batch of samples. In addition, a strong attention should be brought to the measurement resolution when thin films of a few tenths of nanometre are under investigation. Ellipsometry is one possible measurement tool that can be employed to study interfaces in multilayer stacks at the nanometre scale. A graded interface between two layers can be modelled and was reported to be very accurate.[157] For the application in OLEDs, further development should be done on techniques with sub-nanometre resolution offering a fast analysis.

One of the fundamental problems with the orthogonal solvent system approach is that small-molecule materials can be washed away by a solvent even though the small molecule might not be soluble in that solvent. Recently, Aizawa et al.[158] demonstrated that if the molecular weight of the small molecule exceeds a certain threshold value, the film will remain intact. This work opens up a route to fabricate small-molecule-based multilayer solution-processed OLEDs.[159] Follow-up is needed in this direction in order to build up multilayer architecture from solution with small molecules which are of interest for high resolution displays. This path tackles interface control from the material instead of the ink solvent point of view.

Acknowledgments

This thesis is the result of three years and ten months of experience I have encountered at the Technische Universität Darmstadt and at Merck KGaA from various people who I wish to thank. Firstly, I would like to extend my gratitude to the members of the committee, Prof. von Seggern, Prof. Dörsam, Prof. Alff and Prof. Ensinger, for reading and accepting to assess this PhD thesis.

Prof. von Seggern, my Doktorvater, guided me throughout the research work which is why I would like to express him my gratitude but also for his patience and persistent help with the writing of the thesis. In addition, I wish to show my sincere appreciation to Prof. Dörsam, who welcomed me in his research group and gave me constant encouragement throughout my research work. It was a great chance to participate to the Doktorandkolloquium with the PhD students of the Institut für Druckmaschinen und Druckverfahren (IDD) where insightful discussions took place.

I would also like to extend my deepest gratitude to Remi Anemian and Peter Levermore, who gave me the opportunity to join the research team of OLED department in Merck Darmstadt. Without them, this thesis would not have been possible. I am also pleased to say thank you to Edgar Böhm, Aurélie Ludemann, Christian Heiss, Georg Bernatz and Rocco Fortte, who made my access simpler to the research facilities and various laboratories.

I gratefully acknowledge the assistance of Katja Maria Scheible for re-orienting my research topic into an exciting world exploring the impact of OLED ink formulation on material cross-linking properties. Gaëlle Béalle have been and still is a tremendous mentor for me. I would like to thank you for always being by my sides and for being a great advisor beyond imagination. During the challenging times, you gave me confidence, moral support and the freedom I needed to grow as a research scientist. I would also like to pay my special regards to Manuel Hamburger for his relentless support and profound belief in my work and abilities to carry this academic study. I am extremely grateful for your patience in the publication process of my article and your motivation that gave me power to excel in the research writing.

The completion of my dissertation would not have been accomplished without the support of the Merck OLED department. I express my deepest gratitude to the soluble team for playing a major role in my research work and my personal development, especially Hsin-Rong Tseng, Sebastian Meyer, Sebastian Stoltz and Miriam Engel.

Whenever possible, my days started in the best way around a coffee in the innovation center surrounded by Bouchon, Stevi, Mikiki, Christoph and Manuel. I already missed this fruitful morning discussions.

My fellow labmates played a decisive part in fulfilment of my goals and in keeping a good mental health. A special thanks for the fun-time we spent together, and for the stimulating discussions. The support of the OLED ink formulation and the OLED application printing team really meant a lot to

me. I was a great pleasure to work with you guys. Nathalie, Toto, Dieter, Chica, Denis and Thorsten, I hope to cross your road again in a lab sometimes.

Heartfelt thanks to the labs and team that welcomed me for punctual measurements: the IDD team, the first screening lab, the troubleshooting analytics lab, the early R&D formulation lab and the analytical lab for particle characterisation.

I wish to express my sincere thanks to the support and love of my family and friends. My mädels, my rainbow and Tac (from Tic&Tac) offered me a great cocktail encouragement and getaway moments which I cherished. I feel the need to thank my parents in French…

Tima et tipa, vous êtes mes piliers, mon moteur et mon filet de sécurité. Vous me donnez l'amour et les moyens nécessaires dont j'ai besoin pour accomplir tous mes projets, et je ne sais comment vous remercier. Je vous aime et je continuerai à vous rendre fiers.

Last but not least, I thank Katim for entering my life during this exciting and challenging time. You always believed in me, and you gave me wings.

Curriculum Vitae

Pauline Hibon

Contact

Arheilger Weg 21
64331 Weiterstadt
Germany

+33 665-204897

hibon.pauline@gmail.com

Paulinehibon.51.45

Nationality: French

Social

LinkedIn
https://www.linkedin.com/in/paulinehibon

Research gate
https://www.researchgate.net/profile/Pauline_Hibon

Hobbies & interests

- Rotaract Member of Darmstadt's club (Germany)
- Travelling & Outdoor Sports

Education

PhD Thesis, Merck KGaA, TU Darmstadt, Darmstadt (Germany) *5/2016 – Presen*

Influence of inkjet printing (IJP) solvents on cross-linkable polymers thin films stability

- Formulation of IJP inks for OLED devices
- Characterisation of thin films
- Large area printing

Master Thesis, Fraunhofer Institute IOF, Jena (Germany) *3/2015 - 4/201*

Organic Light Emitting electrochemical Cell

- Device characterisation
- Inkjet printing of small molecules

Master of Engineering in Electronics and Optics in Polytech Orléans, Orléans (France) *9/2010 - 3/201*

Photonics specialty

Exchange year at the department of Electrical Engineering, University of Cyprus, Nicosia (Cyprus)

Optics, Photonics and photovoltaics specialty

Work Experience

Laboratory Assistant *6/2014 – 8/201*

University of Cyprus, Nicosia (Cyprus)

- Pulsed Laser Deposition
- Thin films characterisation
- X-Ray Diffraction

Engineer Assistant *6/2013 – 9/201*

Lighting design office Aartill, Montmorency (France)

- Design of lighting plans in public, sportive, interior and architectural lighting
- Lighting calculation, computer-aided design
- Project management, cost estimation.

Public Relations Manager *9/2012 – 7/201*

Junior Company of Polytech Orléans Polytech Expertise, Orléans (France)

- Public relations with the medias for Polytech Expertise
- Meetings leading, Network creation

Key Skills

- expert in formulation of organic based media
- broad knowledfe in anayltical technics (FTIR, DLS, DSC, TGA, rheology)

Linguistics

French ●●●●●

English ●●●●●

German ●●●●○

Conference paper

- Böhm, Edgar et al (2017). 57-1: Invited Paper: Ink-Jet-Printed OLED Displays. SID Symposium Digest of Technical Papers. 48. 842-844. 10.1002/sdtp.11783.
- Oral presentation entitled ""Printed OLEDs: Tuning thin film stability against solvent by ink formulation" at the 29th Assembly of Advanced Material Congress in Octobre 2019, Sweden
- Hibon, P., et al. (2020), Improved thin film stability of differently formulated, printed, and crosslinked polymer layers against successive solvent printing. *J Appl Polym Sci*, 48895. doi: https://doi.org/10.1002/app.48895

Table of Figures

Table of Tables

List of Abbreviations

ATR	Attenuated Total Reflectance
CCD	Charge-Coupled Device
DIPS	Diffusion Induced Phase Separation
DLS	Dyanimic Light Scattering
DoD	Drop on Demand
DOS	Density of State
EBL	Electron Blocking Layer
EIL	Electron Injection Layer
EL	Electroluminescence
EML	Emissive Layer
EQE	External Quantum Efficiency
ETL	Electron Transport Layer
FTIR	Fourier-Transform Infrared Spectroscopy
GPC	Gel Permeation Chromatography
HBL	Hole Blocking Layer
HIL	Hole Injection Layer
HOD	Hole Only Device
HOMO	Highest Occupied Molecular Orbital
HTL	Hole Transport Layer
HTM	Hole Transport Material
IR	Infrared
ITO	Indium Tin Oxide
LCD	Liquid Crystal Display
LED	Light Emitting Diode
LT	Lifetime
LUMO	Lowest Unoccupied Molecular Orbital
MSE	Mean-Square-Error
NIPS	Non-solvent Induced Phase Separation
PPI	Pixel Per Inch
PCS	Photon Correlation Spectroscopy
OFET	Organic Field-Effect Transistor
OLED	Organic Light Emitting Diode

OPV	Organic Photovoltaic
QELS	Quasi-Elastic Light Scattering
SCLC	Space Charge Limited Current
SFT	Surface Tension
TAA	Triaryl Amine
TGA	Thermal Gravimetry Analysis
PVD	Physical Vapour Deposition

Formula Directory

α and k Mark-Houwink parameters

$\dot{\gamma}$ shear rate 1/s

γ_{e-h} charge carrier balance between injected holes and electrons in the EML (should be 1)

ε dielectric constant

ε_0 vacuum permittivity

η viscosity of the suspension mPa·s

$[\eta]$ intrinsic viscosity of the polymer in the specific solvent

η_{ext} external quantum efficiency

η_f ratio of radiative transition from singlet excitons.

η_L luminous efficiency in the unit cd·A^{-1}

η_r relative viscosity

η_s viscosity of the medium

η_{sp} specific viscosity

μ charge mobility

π bonding molecular orbital

π^* anti-bonding molecular orbital

σ shear stress in mPa

Φ volume fraction of solids in the suspension

Φ' a universal constant independent of temperature and polymer-solvent system where $\Phi' = 2.1 \times 10^{26}$ kmol^{-1}

φ_{opt} outcoupling efficiency: ratio of light emitted at the surface to the light produced in the bulk of the device (estimated 20%)

$\chi_{s/t}$ fraction of generated excitons which can decay radiatively (0.25 in fluorescence, 1 in phosphorescence)

ω angular speed

A active luminous area A= 4.606 mm^2

c concentration of polymer

c* overlap concentration

D diffusion coefficient

d_H hydrodynamic diameter

DS	droplet spacing
e	elementary electron charge 1.6021765×10^{-19} C
E_b	Injection barrier
E_F	Fermi level
Eg	energy gap
f	printing frequency
$\Delta H_{(Sx)}$	cross-linking enthalpy of the polymer in film
$\Delta H_{(S0)}$	cross-linking enthalpy in powder without solvent
I	current in mA
j	current density in $mA\cdot cm^{-2}$
k	extinction coefficient
k_B	Boltzmann constant 1.38×10^{-23} $m^2\cdot kg\cdot s^{-2}\cdot K^{-1}$
K_H	Huggins constant
K_K	Kramer constant
L	luminance in $cd\cdot m^2$
L_0	initial luminance
m_f	total mass after drying of material and solvent residue
m_s	mass of solvent residue in bulk
M_w	molecular weight
n	index of refraction
AF	the acceleration factor must be determined for each colour
q	sample heat flow
R	resistance of a thermocouple
r_c	effective interactive capture radius
R_g	radius of gyration
R_h	hydrodynamic radius
r_s	solvent residue in w%
S_0	singlet ground state
S_1	first singlet excited state
T	temperature
T_g	transition glass
ΔT	temperature difference between the sample pan and the reference pan
V_0	applied voltage
v_{print}	printing speed

$X_{(Sx)}$ cross linking degree

List of References

1. Inoguchi, T.; Takeda, M.; Kakihara, Y.; Nakata, Y.; Yoshida, M., Stable High-Brightness Thin-Film Electroluminescent Panels. *J. SID 1974 digest International Symposium* **1974**, *84*.
2. Tang, C. W.; VanSlyke, S. A., Organic Electroluminescent Diodes. *Appl. Phys. Lett.* **1987**, *51*, 913-915.
3. Shirakawa, H.; Louis, E. J.; MacDiarmid, A. G.; Chiang, C. K.; Heeger, A. J., Synthesis of Electrically Conducting Organic Polymers: Halogen Derivatives of Polyacetylene,(Ch)X. *J. Chem. Soc. Chem. Comm.* **1977**, 578-580.
4. Burroughes, J. H.; Bradley, D. D.; Brown, A.; Marks, R.; Mackay, K.; Friend, R. H.; Burns, P.; Holmes, A., Light-Emitting Diodes Based on Conjugated Polymers. *Nature* **1990**, *347*, 539.
5. Gustafsson, G.; Cao, Y.; Treacy, G.; Klavetter, F.; Colaneri, N.; Heeger, A., Flexible Light-Emitting Diodes Made from Soluble Conducting Polymers. *Nature* **1992**, *357*, 477.
6. Ishii, H.; Sugiyama, K.; Ito, E.; Seki, K., Energy Level Alignment and Interfacial Electronic Structures at Organic/Metal and Organic/Organic Interfaces. *Adv. Mater.* **1999**, *11*, 605-625.
7. Parker, I. D., Carrier Tunneling and Device Characteristics in Polymer Light-Emitting Diodes. *J. Appl. Phys.* **1994**, *75*, 1656-1666.
8. Su, W.-F.; Chen, Y., Synthesis and Optoelectronic Properties of Thermally Cross-Linkable Hole-Transporting Poly (Fluorene-Co-Triphenylamine). *Polymer* **2011**, *52*, 77-85.
9. Li, Y.-J.; Sasabe, H.; Su, S.-J.; Tanaka, D.; Takeda, T.; Pu, Y.-J.; Kido, J., Highly Efficient Green Phosphorescent Oled Based on Pyridine-Containing Starburst Electron-Transporting Materials. *Chem. Lett.* **2010**, *39*, 140-141.
10. Søndergaard, R. R.; Hösel, M.; Krebs, F. C., Roll-to-Roll Fabrication of Large Area Functional Organic Materials. *J. Polym. Sci., Part B: Polym. Phys.* **2013**, *51*, 16-34.
11. Bharathan, J.; Yang, Y., Polymer Electroluminescent Devices Processed by Inkjet Printing: I. Polymer Light-Emitting Logo. *Appl. Phys. Lett.* **1998**, *72*, 2660-2662.
12. Zhong, C.; Duan, C.; Huang, F.; Wu, H.; Cao, Y., Materials and Devices toward Fully Solution Processable Organic Light-Emitting Diodes. *Chem. Mater.* **2010**, *23*, 326-340.
13. Li, Y., Rgb Printed Amoled: Challenges and Opportunities. *SID Symposium Digest of Technical Papers* **2018**, *49*, 95-98.
14. Shao, L.-Q.; Ting-Dong; Liang, J.-S.; Bi, Z.-T.; Zhe-Li; Jingyao-Song; Huo, S.-T., The Development of 403 Ppi Real Rgb Printing Amoled. *SID Symposium Digest of Technical Papers* **2019**, *50*, 1943-1945.
15. Prakash, S.; Sims, M.; Wyrsta, I.; Parker, I. D.; Kondakov, D.; Gao, W., Solution-Processed Oleds: Unique Challenges and Advantages. *SID Symposium Digest of Technical Papers* **2013**, *44*, 678-681.
16. Ho, S.; Chen, Y.; Liu, S.; Peng, C.; Zhao, D.; So, F., Interface Effect on Efficiency Loss in Organic Light Emitting Diodes with Solution Processed Emitting Layers. *Adv. Mater. Interfaces* **2016**, *3*, 1600320.
17. Smith, A. R.; Lee, K. H.; Nelson, A.; James, M.; Burn, P. L.; Gentle, I. R., Diffusion–the Hidden Menace in Organic Optoelectronic Devices. *Adv. Mater.* **2012**, *24*, 822-826.
18. Steuerman, D. W.; Garcia, A.; Dante, M.; Yang, R.; Löfvander, J. P.; Nguyen, T. Q., Imaging the Interfaces of Conjugated Polymer Optoelectronic Devices. *Adv. Mater.* **2008**, *20*, 528-534.
19. Perumal, A.; Faber, H.; Yaacobi-Gross, N.; Pattanasattayavong, P.; Burgess, C.; Jha, S.; McLachlan, M. A.; Stavrinou, P. N.; Anthopoulos, T. D.; Bradley, D. D., High-Efficiency, Solution-Processed, Multilayer Phosphorescent Organic Light-Emitting Diodes with a Copper Thiocyanate Hole-Injection/Hole-Transport Layer. *Adv. Mater.* **2015**, *27*, 93-100.
20. Huang, F.; Cheng, Y.-J.; Zhang, Y.; Liu, M. S.; Jen, A. K. Y., Crosslinkable Hole-Transporting Materials for Solution Processed Polymer Light-Emitting Diodes. *J. Mater. Chem.* **2008**, *18*, 4495-4509.
21. Huang, F.; Wu, H.; Cao, Y., Water/Alcohol Soluble Conjugated Polymers as Highly Efficient Electron Transporting/Injection Layer in Optoelectronic Devices. *Chem. Soc. Rev.* **2010**, *39*, 2500-2521.
22. Sax, S.; Rugen-Penkalla, N.; Neuhold, A.; Schuh, S.; Zojer, E.; List, E. J.; Müllen, K., Efficient Blue-Light-Emitting Polymer Heterostructure Devices: The Fabrication of Multilayer Structures from Orthogonal Solvents. *Adv. Mater.* **2010**, *22*, 2087-2091.
23. Cheng, Y.-J.; Liu, M. S.; Zhang, Y.; Niu, Y.; Huang, F.; Ka, J.-W.; Yip, H.-L.; Tian, Y.; Jen, A. K. Y., Thermally Cross-Linkable Hole-Transporting Materials on Conducting Polymer: Synthesis,

Characterization, and Applications for Polymer Light-Emitting Devices. *Chem. Mater.* **2008**, *20*, 413-422.
24. Müller, C. D.; Falcou, A.; Reckefuss, N.; Rojahn, M.; Wiederhirn, V.; Rudati, P.; Frohne, H.; Nuyken, O.; Becker, H.; Meerholz, K., Multi-Colour Organic Light-Emitting Displays by Solution Processing. *Nature* **2003**, *421*, 829.
25. Li, W., et al., Covalently Interlinked Organic Led Transport Layers Via Spin-Coating/Siloxane Condensation. *Adv. Mater.* **1999**, *11*, 730-734.
26. Tseng, S.-R.; Lin, S.-C.; Meng, H.-F.; Liao, H.-H.; Yeh, C.-H.; Lai, H.-C.; Horng, S.-F.; Hsu, C.-S., General Method to Solution-Process Multilayer Polymer Light-Emitting Diodes. *Appl. Phys. Lett.* **2006**, *88*, 163501.
27. Chen, C.-Y., et al., Continuous Blade Coating for Multi-Layer Large-Area Organic Light-Emitting Diode and Solar Cell. *J. Appl. Phys.* **2011**, *110*, 094501.
28. Yeh, H.-C.; Meng, H.-F.; Lin, H.-W.; Chao, T.-C.; Tseng, M.-R.; Zan, H.-W., All-Small-Molecule Efficient White Organic Light-Emitting Diodes by Multi-Layer Blade Coating. *Org. Electron.* **2012**, *13*, 914-918.
29. Garcia, A.; Yang, R.; Jin, Y.; Walker, B.; Nguyen, T.-Q., Structure-Function Relationships of Conjugated Polyelectrolyte Electron Injection Layers in Polymer Light Emitting Diodes. *Appl. Phys. Lett.* **2007**, *91*, 153502.
30. Ma, W.; Iyer, P. K.; Gong, X.; Liu, B.; Moses, D.; Bazan, G. C.; Heeger, A. J., Water/Methanol-Soluble Conjugated Copolymer as an Electron-Transport Layer in Polymer Light-Emitting Diodes. *Adv. Mater.* **2005**, *17*, 274-277.
31. Zhang, Y.; Huang, F.; Chi, Y.; Jen, A. K. Y., Highly Efficient White Polymer Light-Emitting Diodes Based on Nanometer-Scale Control of the Electron Injection Layer Morphology through Solvent Processing. *Adv. Mater.* **2008**, *20*, 1565-1570.
32. Hansen, E. F.; Derrick, M. R.; Schilling, M. R.; Garcia, R., The Effects of Solution Application on Some Mechanical and Physical Properties of Thermoplastic Amorphous Polymers Used in Conservation: Poly(Vinyl Acetate)S. *J. Am. Inst. Conserv.* **1991**, *30*, 203-213.
33. Olayemi, J. Y.; Adeyeye, A. A., Some Properties of Polyvinyl Acetate Films Cast from Methanol, Acetone and Chloroform as Solvent. *Polym. Test.* **1982**, *3*, 25-35.
34. Ohisa, S.; Matsuba, G.; Yamada, N. L.; Pu, Y.-J.; Sasabe, H.; Kido, J., Precise Evaluation of Angstrom-Ordered Mixed Interfaces in Solution-Processed Oleds by Neutron Reflectometry. *Adv. Mater.* **2014**, *1*, 1400097.
35. Kang, P.-G.; Shin, D. H.; Na, H.-Y.; Doh, Y.-J.; John, K.; Liam, S.; Suh, M. C., The Interfacial Effect between Htl and Eml on the Efficiency of Solution Processed Green Phosphorescent Oleds. *SID Symposium Digest of Technical Papers* **2016**, *47*, 494-497.
36. Pope, M.; Kallmann, H.; Magnante, P., Electroluminescence in Organic Crystals. *J. Chem. Phys.* **1963**, *38*, 2042-2043.
37. Helfrich, W.; Schneider, W., Recombination Radiation in Anthracene Crystals. *Phys. Rev. Lett.* **1965**, *14*, 229.
38. Geffroy, B.; Le Roy, P.; Prat, C., Organic Light-Emitting Diode (Oled) Technology: Materials, Devices and Display Technologies. *Polym. Int.* **2006**, *55*, 572-582.
39. Gaspar, D. J.; Polikarpov, E., *Oled Fundamentals: Materials, Devices, and Processing of Organic Light-Emitting Diodes*; CRC press, 2015.
40. Bässler, H., Charge Transport in Disordered Organic Photoconductors a Monte Carlo Simulation Study. *Phys. Status Solidi B* **1993**, *175*, 15-56.
41. Heun, S.; Bässler, H.; Borsenberger, P., The Spectral Assessment of the Origin of the Polaronic Contribution to Charge Transport in a Highly Conjugated Triarylamine Donor Molecule. *Chem. Phys.* **1995**, *200*, 265-270.
42. Brütting, W., Physics of Organic Semiconductors. *Phys. Status Solidi A* **2004**, *201*, 1031-1031.
43. Van der Holst, J.; Van Oost, F.; Coehoorn, R.; Bobbert, P., Electron-Hole Recombination in Disordered Organic Semiconductors: Validity of the Langevin Formula. *Phys. Rev. B* **2009**, *80*, 235202.
44. https://www.thermofisher.com/order/catalog/product/379-0340 (accessed 28.10.2019).
45. Baldo, M.; O'brien, D.; Thompson, M.; Forrest, S., Excitonic Singlet-Triplet Ratio in a Semiconducting Organic Thin Film. *Phys. Rev. B* **1999**, *60*, 14422.

46. Baldo, M. A.; O'brien, D.; You, Y.; Shoustikov, A.; Sibley, S.; Thompson, M.; Forrest, S. R., Highly Efficient Phosphorescent Emission from Organic Electroluminescent Devices. *Nature* **1998**, *395*, 151-154.
47. Salaneck, W. R.; Lundström, I.; Rånby, B. G., *Conjugated Polymers and Related Materials: The Interconnection of Chemical and Electronic Structure: Proceedings of the Eighty-First Nobel Symposium*; Oxford University Press, USA, 1993; Vol. 81.
48. Taylor, D., Vacuum-Thermal-Evaporation: The Route for Roll-to-Roll Production of Large-Area Organic Electronic Circuits. *Semicond. Sci. Technol.* **2015**, *30*, 054002.
49. Newby, C.; Lee, J.-K.; Ober, C. K., The Solvent Problem: Redissolution of Macromolecules in Solution-Processed Organic Electronics. *Macromol. Res.* **2013**, *21*, 248-256.
50. Trattnig, R.; Pevzner, L.; Jäger, M.; Schlesinger, R.; Nardi, M. V.; Ligorio, G.; Christodoulou, C.; Koch, N.; Baumgarten, M.; Müllen, K., Bright Blue Solution Processed Triple-Layer Polymer Light-Emitting Diodes Realized by Thermal Layer Stabilization and Orthogonal Solvents. *Adv. Funct. Mater.* **2013**, *23*, 4897-4905.
51. Böhm, E.; Levermore, P.; Tseng, H.-R.; Bealle, G.; Wang, H.-J.; Hibon, P.; Heil, H.; Jatsch, A.; Buchholz, H., Ink-Jet-Printed Oled Displays. 2017.
52. Zhu, M.; Yang, C., Blue Fluorescent Emitters: Design Tactics and Applications in Organic Light-Emitting Diodes. *Chem. Soc. Rev.* **2013**, *42*, 4963-4976.
53. Zhang, Z.; Wang, Q.; Dai, Y.; Liu, Y.; Wang, L.; Ma, D., High Efficiency Fluorescent White Organic Light-Emitting Diodes with Red, Green and Blue Separately Monochromatic Emission Layers. *Org. Electron.* **2009**, *10*, 491-495.
54. Lou, Y.; Okawa, Y.; Wang, Z.; Naka, S.; Okada, H., Efficient Electron Transport in 4, 4′-Bis [N-(1-Napthyl)-N-Phenyl-Amino] Biphenyl and the Applications in White Organic Light Emitting Devices. *Org. Electron.* **2013**, *14*, 1015-1020.
55. Shirakawa, H., Nobel Lecture: The Discovery of Polyacetylene Film—the Dawning of an Era of Conducting Polymers. *Rev. Mod. Phys.* **2001**, *73*, 713.
56. Shahnawaz; Sudheendran Swayamprabha, S.; Nagar, M. R.; Yadav, R. A. K.; Gull, S.; Dubey, D. K.; Jou, J.-H., Hole-Transporting Materials for Organic Light-Emitting Diodes: An Overview. *J. Mater. Chem. C* **2019**, *7*, 7144-7158.
57. Schols, S.; Verlaak, S.; Rolin, C.; Cheyns, D.; Genoe, J.; Heremans, P., An Organic Light-Emitting Diode with Field-Effect Electron Transport. *Adv. Funct. Mater.* **2008**, *18*, 136-144.
58. Benvenho, A. R. V.; Serbena, J. P. M.; Lessmann, R.; Hümmelgen, I. A.; Mello, R. M. Q. d.; Li, R. W. C.; Cuvero, J. H.; Gruber, J., Efficient Organic Light-Emitting Diodes with Fluorine-Doped Tin-Oxide Anode and Electrochemically Synthesized Sulfonated Polyaniline as Hole Transport Layer. *Braz. J. Phys.* **2005**, *35*, 1016-1019.
59. Park, S.-R.; Kang, J.-H.; Ahn, D. A.; Suh, M. C., A Cross-Linkable Hole Transport Material Having Improved Mobility through a Semi-Interpenetrating Polymer Network Approach for Solution-Processed Green Pholeds. *J. Mater. Chem. C* **2018**, *6*, 7750-7758.
60. Grigalevicius, S.; Zhang, B.; Xie, Z.; Forster, M.; Scherf, U., Polycarbazole-Based Networks Made by Photo-Crosslinking for Hole Transporting Layers of Oled Devices. *Org. Electron.* **2011**, *12*, 2253-2257.
61. Zuniga, C. A.; Barlow, S.; Marder, S. R., Approaches to Solution-Processed Multilayer Organic Light-Emitting Diodes Based on Cross-Linking. *Chem. Mater.* **2011**, *23*, 658-681.
62. Günes, S.; Neugebauer, H.; Sariciftci, N. S., Conjugated Polymer-Based Organic Solar Cells. *Chem. Rev.* **2007**, *107*, 1324-1338.
63. Kawase, T.; Shimoda, T.; Newsome, C.; Sirringhaus, H.; Friend, R. H., Inkjet Printing of Polymer Thin Film Transistors. *Thin solid films* **2003**, *438*, 279-287.
64. Jeanmaire, D. L.; Hawkins, G. A.; Sharma, R. Continuous Inkjet Printhead with Selectable Printing Volumes of Ink. 2003.
65. Bogy, D. B.; Talke, F. E., Experimental and Theoretical Study of Wave Propagation Phenomena in Drop-on-Demand Ink Jet Devices. *IBM J. Res. Dev.* **1984**, *28*, 314-321.
66. Tekin, E.; Smith, P. J.; Schubert, U. S., Inkjet Printing as a Deposition and Patterning Tool for Polymers and Inorganic Particles. *Soft Matter.* **2008**, *4*, 703-713.
67. Lee, E. R., *Microdrop Generation*; CRC press, 2018.
68. Sirringhaus, H.; Sele, C. W.; Werte, v., T.; Ramsdale, C., *Organic Electronics: Materials, Manufacturing, and Applications*; John Wiley & Sons, 2006.
69. http://fab.cba.mit.edu/classes/865.18/additive/inkjet-printing/index.html (accessed 28.10.2019).

70. Brünahl, J.; Grishin, A. M., Piezoelectric Shear Mode Drop-on-Demand Inkjet Actuator. *Sensor. Actuat A-Phys* **2002**, *101*, 371-382.
71. Smith, P. J.; Morrin, A., An Introduction. In *Reactive Inkjet Printing*, 2017; pp 1-11.
72. Fromm, J. E., Numerical Calculation of the Fluid Dynamics of Drop-on-Demand Jets. *IBM J. Res. Dev.* **1984**, *28*, 322-333.
73. Singh, M.; Haverinen, H. M.; Dhagat, P.; Jabbour, G. E., Inkjet Printing - Process and Its Applications. *Adv. Mater.* **2010**, *22*, 673-685.
74. de Gans, B.; Kazancioglu, E.; Meyer, W.; Schubert, U. S., Ink-Jet Printing Polymers and Polymer Libraries Using Micropipettes. *Macromol. Rapid Commun.* **2004**, *25*, 292-296.
75. Jang, D.; Kim, D.; Moon, J., Influence of Fluid Physical Properties on Ink-Jet Printability. *Langmuir* **2009**, *25*, 2629-2635.
76. Tekin, E.; Holder, E.; Kozodaev, D.; Schubert, U. S., Controlled Pattern Formation of Poly[2-Methoxy-5-(2′-Ethylhexyloxyl)–1,4-Phenylenevinylene] (Meh–Ppv) by Ink-Jet Printing. *Adv. Funct. Mater.* **2007**, *17*, 277-284.
77. Soltman, D.; Subramanian, V., Inkjet-Printed Line Morphologies and Temperature Control of the Coffee Ring Effect. *Langmuir* **2008**, *24*, 2224-2231.
78. Tekin, E.; de Gans, B.-J.; Schubert, U. S., Ink-Jet Printing of Polymers – from Single Dots to Thin Film Libraries. *J. Mater. Chem.* **2004**, *14*, 2627-2632.
79. Tekoglu, S.; Hernandez-Sosa, G.; Kluge, E.; Lemmer, U.; Mechau, N., Gravure Printed Flexible Small-Molecule Organic Light Emitting Diodes. *Org. Electron.* **2013**, *14*, 3493-3499.
80. Deegan, R. D., Pattern Formation in Drying Drops. *Phys. Rev. E* **2000**, *61*, 475-485.
81. Deegan, R. D.; Bakajin, O.; Dupont, T. F.; Huber, G.; Nagel, S. R.; Witten, T. A., Capillary Flow as the Cause of Ring Stains from Dried Liquid Drops. *Nature* **1997**, *389*, 827-829.
82. Ko, H.-Y.; Park, J.; Shin, H.; Moon, J., Rapid Self-Assembly of Monodisperse Colloidal Spheres in an Ink-Jet Printed Droplet. *Chem. Mater.* **2004**, *16*, 4212-4215.
83. Teichler, A.; Shu, Z.; Wild, A.; Bader, C.; Nowotny, J.; Kirchner, G.; Harkema, S.; Perelaer, J.; Schubert, U. S., Inkjet Printing of Chemically Tailored Light-Emitting Polymers. *Eur. Polym. J.* **2013**, *49*, 2186-2195.
84. Grosberg, A. Y.; Khokhlov, A. R., *Giant Molecules: Here, and There, and Everywhere*, 1997.
85. Fred, W.; Billmeyer, J., Textbook of Polymer Science. Wiley, New York: 1984.
86. Francuskiewicz, F., Dissolution and Precipitation of Polymers. In *Polymer Fractionation*, Francuskiewicz, F., Ed. Springer Berlin Heidelberg: Berlin, Heidelberg, 1994; pp 10-18.
87. Drioli, E.; Giorno, L.; Macedonio, F., *Membrane Engineering*; Walter de Gruyter GmbH & Co KG, 2018.
88. Zade, S. S.; Bendikov, M., Twisting of Conjugated Oligomers and Polymers: Case Study of Oligo- and Polythiophene. *Chemistry – A European Journal* **2007**, *13*, 3688-3700.
89. Teraoka, I., *Polymer Solutions: An Introduction to Physical Properties*; John Wiley & Sons, 2002.
90. Rao, M. A., *Rheology of Fluid and Semisolid Foods: Principles and Applications*; Springer Science & Business Media, 2010.
91. Eckes, F.; Stegmaier, K.; Hayer, A.; Heil, H.; Joosten, D. Polymere Enthaltend Substituierte Triarylamin-Einheiten Sowie Elektrolumineszenzvorrichtungen Enthaltend Diese Polymere. WO2013156130A1, 2013.
92. Miller-Chou, B. A.; Koenig, J. L., A Review of Polymer Dissolution. *Prog. Polym. Sci.* **2003**, *28*, 1223-1270.
93. Hina, S.; Zhang, Y.; Wang, H., Characterization of Polymeric Solutions: A Brief Overview. *Rev. Adv. Mater. Sci.* **2014**, *36*, 165-176.
94. *Dynamic Light Scattering: An Introduction in 30 Minutes*; Malvern Instruments: p 8.
95. Venerus David, C., Free Surface Effects on Normal Stress Measurements in Cone and Plate Flow. In *Applied Rheology*, 2007; Vol. 17, pp 36494-1.
96. Voigt, M. M.; Mackenzie, R. C.; King, S. P.; Yau, C. P.; Atienzar, P.; Dane, J.; Keivanidis, P. E.; Zadrazil, I.; Bradley, D. D.; Nelson, J., Gravure Printing Inverted Organic Solar Cells: The Influence of Ink Properties on Film Quality and Device Performance. *Sol. Energy Mater. Sol. Cells* **2012**, *105*, 77-85.
97. Kazmierski, B. K. Inkjet Printing onto Patterned Substrates. Durham University, 2016.
98. Chesterfield, R.; Johnson, A.; Lang, C.; Stainer, M.; Ziebarth, J., Solution-Coating Technology for Amoled Displays. *J. SID* **2011**, 24-29.
99. Wyant, J. C. In *White Light Interferometry*, Holography: A Tribute to Yuri Denisyuk and Emmett Leith, International Society for Optics and Photonics: 2002; pp 98-107.

100. Duvivier, D.; Blake, T. D.; De Coninck, J., Toward a Predictive Theory of Wetting Dynamics. *Langmuir* **2013**, *29*, 10132-10140.
101. Himcinschi, C.; Friedrich, M.; Murray, C.; Streiter, I.; Schulz, S.; Gessner, T.; Zahn, D., Characterization of Silica Xerogel Films by Variable-Angle Spectroscopic Ellipsometry and Infrared Spectroscopy. *Semicond. Sci. Technol.* **2001**, *16*, 806.
102. Othman, M.; Lubguban, J.; Lubguban, A. A.; Gangopadhyay, S.; Miller, R.; Volksen, W.; Kim, H.-C., Characterization of Porous Low-K Films Using Variable Angle Spectroscopic Ellipsometry. *J. Appl. Phys.* **2006**, *99*, 083503.
103. Li, H.; Tessler, N.; Brédas, J.-L., Assessment of the Factors Influencing Charge-Carrier Mobility Measurements in Organic Field-Effect Transistors. *Adv. Funct. Mater.* **2018**, *28*, 1803096.
104. Kim, S.-K.; Yang, H.; Kim, Y.-S., Control of Carrier Injection and Transport in Quantum Dot Light Emitting Diodes (Qleds) Via Modulating Schottky Injection Barrier and Carrier Mobility. *J. Appl. Phys.* **2019**, *126*, 185702.
105. Wetzelaer, G.-J. A.; Blom, P. W., Diffusion-Driven Currents in Organic-Semiconductor Diodes. *NPG Asia Mater.* **2014**, *6*, 110.
106. Tritt, T. M., Thermoelectric Materials: Principles, Structure, Properties, and Applications. In *Encyclopedia of Materials: Science and Technology*, Buschow, K. H. J.; Cahn, R. W.; Flemings, M. C.; Ilschner, B.; Kramer, E. J.; Mahajan, S.; Veyssière, P., Eds. Elsevier: Oxford, 2002; pp 1-11.
107. Rose, A., Space-Charge-Limited Currents in Solids. *Phys. Rev.* **1955**, *97*, 1538-1544.
108. Park, G.-W.; Lee, S.-J.; Ko, J.-H., Comparison of Outcoupling Efficiency between Bottom-Emission and Top-Emission Organic Light-Emitting Diodes Using Fdtd Simulation. *J. Nanoelectron. Optoelectron.* **2016**, *11*, 229-233.
109. Su, W.-F., Polymer Size and Polymer Solutions. In *Principles of Polymer Design and Synthesis*, Springer Berlin Heidelberg: Berlin, Heidelberg, 2013; pp 9-26.
110. Marciniak, A., The Hildebrand Solubility Parameters of Ionic Liquids - Part 2. *Int. J. Mol. Sci.* **2011**, *12*, 3553-3575.
111. Zhu, Q.-N.; Wang, Q.; Hu, Y.-B.; Abliz, X., Practical Determination of the Solubility Parameters of 1-Alkyl-3-Methylimidazolium Bromide ([Cnc1im]Br, N = 5, 6, 7, 8) Ionic Liquids by Inverse Gas Chromatography and the Hansen Solubility Parameter. *Molecules* **2019**, *24*, 1346.
112. Rotureau, E.; Dellacherie, E.; Durand, A., Viscosity of Aqueous Solutions of Polysaccharides and Hydrophobically Modified Polysaccharides: Application of Fedors Equation. *Eur. Polym. J.* **2006**, *42*, 1086-1092.
113. Huggins, M. L., The Viscosity of Dilute Solutions of Long-Chain Molecules. Iv. Dependence on Concentration. *JACS* **1942**, *64*, 2716-2718.
114. Kraemer, E. O., Molecular Weights of Celluloses and Cellulose Derivates. *Ind. Eng. Chem.* **1938**, *30*, 1200-1203.
115. Pamies, R.; Cifre, J. G. H.; Martínez, M. d. C. L.; de la Torre, J. G., Determination of Intrinsic Viscosities of Macromolecules and Nanoparticles. Comparison of Single-Point and Dilution Procedures. *Colloid Polym. Sci.* **2008**, *286*, 1223-1231.
116. Mello, I. L.; Delpech, M. C.; Coutinho, F. M. B.; Albino, F. F. M., Viscometric Study of High-Cis Polybutadiene in Toluene Solution. *J. Braz. Chem. Soc.* **2006**, *17*, 194-199.
117. Carreau, P. J.; De Kee, D. C. R.; Chhabra, R. P., *Rheology of Polymeric Systems*: New York, NY, US 1997; Vol. 78, p 428-428.
118. Flory, P. J.; Fox, T. G., Treatment of Intrinsic Viscosities. *JACS* **1951**, *73*, 1904-1908.
119. Alberto Masuelli, M., Mark-Houwink Parameters for Aqueous-Soluble Polymers and Biopolymers at Various Temperatures. *J Polym. and Biopolymer Phys. Chem.* **2014**, *2*, 37-43.
120. Mardles, E. W. J., Viscosity of Suspensions and the Einstein Equation. *Nature* **1940**, *145*, 970-970.
121. Berne, B. J.; Pecora, R., *Dynamic Light Scattering: With Applications to Chemistry, Biology, and Physics*; Courier Corporation, 2000.
122. Teraoka, A. A.; Teraoka, I., *Polymer Solutions: An Introduction to Physical Properties*; John Wiley & Sons, 2002.
123. Panalytical, M. https://www.malvernpanalytical.com/en/support/product-support/zetasizer-range/zetasizer-nano-range.
124. Flory, P. J., Thermodynamics of High Polymer Solutions. *J. Chem. Phys.* **1942**, *10*, 51-61.
125. Hirschl, C., et al., Determining the Degree of Crosslinking of Ethylene Vinyl Acetate Photovoltaic Module Encapsulants - a Comparative Study. *Sol. Energy Mater. Sol. Cells* **2013**, *116*, 203-218.
126. Chung, T. C.; Yuan, X. P. Methods and Materials for Hydrocarbon Recovery. 2011.

127. Klärner, G.; Lee, J. I.; Lee, V. Y.; Chan, E.; Chen, J. P.; Nelson, A.; Markiewicz, D.; Siemens, R.; Scott, J. C.; Miller, R. D., Cross-Linkable Polymers Based on Dialkylfluorenes. *Chem. Mater.* **1999**, *11*, 1800-1805.
128. Stark, W.; Jaunich, M., Investigation of Ethylene/Vinyl Acetate Copolymer (Eva) by Thermal Analysis Dsc and Dma. *Polym. Test.* **2011**, *30*, 236-242.
129. Stark, W.; Jaunich, M.; Bohmeyer, W.; Lange, K., Investigation of the Crosslinking Behaviour of Ethylene Vinyl Acetate (Eva) for Solar Cell Encapsulation by Rheology and Ultrasound. *Polym. Test.* **2012**, *31*, 904-908.
130. Roberts, J. D.; Caserio, M. C., *Basic Principles of Organic Chemistry*; WA Benjamin, Inc., 1977.
131. Bornemann, N.; Sauer, H.; Dörsam, E., Gravure Printed Ultrathin Layers of Small-Molecule Semiconductors on Glass. *J. Imaging Sci. Techn.* **2011**, *55*, 40201-1-40201-8.
132. Tsige, M.; Grest, G. S., Solvent Evaporation and Interdiffusion in Polymer Films. *J. Condens. Matter Phys.* **2005**, *17*, S4119.
133. Kourkoulis, S. K., *Fracture and Failure of Natural Building Stones: Applications in the Restoration of Ancient Monuments*; Springer Science & Business Media, 2007.
134. Chen, J.; Zhuang, H.; Zhao, J.; Gardella Jr., J. A., Solvent Effects on Polymer Surface Structure. *Surf. Interface Anal.* **2001**, *31*, 713-720.
135. Kettle, J.; Lamminmäki, T.; Gane, P., A Review of Modified Surfaces for High Speed Inkjet Coating. *Surf. Coat. Technol.* **2010**, *204*, 2103-2109.
136. Pekcan, Ö.; Canpolat, M.; Kaya, D., In Situ Fluorescence Experiments for Real-Time Monitoring of Annealed High-T Latex Film Dissolution. *Journal of Applied Polymer Science - J APPL POLYM SCI* **1996**, *60*, 2105-2112.
137. Raupp, S. M.; Siebel, D. K.; Kitz, P. G.; Scharfer, P.; Schabel, W., Interdiffusion in Polymeric Multilayer Systems Studied by Inverse Micro-Raman Spectroscopy. *Macromolecules* **2017**, *50*, 6819-6828.
138. Vrentas, J. S.; Duda, J. L., Diffusion in Polymer–Solvent Systems. Ii. A Predictive Theory for the Dependence of Diffusion Coefficients on Temperature, Concentration, and Molecular Weight. *J Polym. Sci. : Polym. Phys. Edition* **1977**, *15*, 417-439.
139. Bianchi, O.; Oliveira, R. V. B.; Fiorio, R.; Martins, J. D. N.; Zattera, A. J.; Canto, L. B., Assessment of Avrami, Ozawa and Avrami–Ozawa Equations for Determination of Eva Crosslinking Kinetics from Dsc Measurements. *Polym. Test.* **2008**, *27*, 722-729.
140. Lu, M.; Shim, M.; Kim, S., Dynamic Dsc Characterization of Epoxy Resin by Means of the Avrami Equation. *J. Therm. Anal. Calorim.* **1999**, *58*, 701-709.
141. Airaksinen, V.-M., Silicon Wafer and Thin Film Measurements. In *Handbook of Silicon Based Mems Materials and Technologies (Second Edition)*, Tilli, M.; Motooka, T.; Airaksinen, V.-M.; Franssila, S.; Paulasto-Kröckel, M.; Lindroos, V., Eds. William Andrew Publishing: Boston, 2015; pp 381-390.
142. Hibon, P.; von Seggern, H.; Tseng, H.-R.; Leonhard, C.; Hamburger, M.; Béalle, G., Improved Thin Film Stability of Differently Formulated, Printed, and Crosslinked Polymer Layers against Successive Solvent Printing. *Journal of Applied Polymer Science - J APPL POLYM SCI* **2020**, *n/a*, 48895.
143. Taylor, M.; Urquhart, A. J.; Zelzer, M.; Davies, M. C.; Alexander, M. R., Picoliter Water Contact Angle Measurement on Polymers. *Langmuir* **2007**, *23*, 6875-6878.
144. Liu, N.; Mei, S.; Sun, D.; Shi, W.; Feng, J.; Zhou, Y.; Mei, F.; Xu, J.; Jiang, Y.; Cao, X., Effects of Charge Transport Materials on Blue Fluorescent Organic Light-Emitting Diodes with a Host-Dopant System. *Micromachines* **2019**, *10*, 344.
145. Lampert, M. A.; Schilling, R. B., Current Injection in Solids: The Regional Approximation Method. In *Semiconduct. Semimet.*, Willardson, R. K.; Beer, A. C., Eds. Elsevier: 1970; Vol. 6, pp 1-96.
146. Widmer, J.; Fischer, J.; Tress, W.; Leo, K.; Riede, M., Electric Potential Mapping by Thickness Variation: A New Method for Model-Free Mobility Determination in Organic Semiconductor Thin Films. *Org. Electron.* **2013**, *14*, 3460-3471.
147. Ohisa, S.; Pu, Y.-J.; Yamada, N. L.; Matsuba, G.; Kido, J., Molecular Interdiffusion between Stacked Layers by Solution and Thermal Annealing Processes in Organic Light Emitting Devices. *ACS Appl. Mater. Interfaces* **2015**, *7*, 20779-20785.
148. Merck Private Communication.
149. Ahn, D. A.; Lee, S.; Chung, J.; Park, Y.; Suh, M. C., Impact of Interface Mixing on the Performance of Solution Processed Organic Light Emitting Diodes—Impedance and Ultraviolet Photoelectron Spectroscopy Study. *ACS Appl. Mater. Interfaces* **2017**, *9*, 22748-22756.

150. Lee, J. Y.; Kim, N. S.; Suh, M. C., Late-News Poster: Influence of Drying and Mixing Condition of the Host Materials on the Lifetime of Solution-Processed Oleds. *SID Symposium Digest of Technical Papers* **2019**, *50*, 1954-1956.
151. Kondakov, D. Y.; Pawlik, T. D.; Nichols, W. F.; Lenhart, W. C., Free-Radical Pathways in Operational Degradation of Oleds. *J. SID* **2008**, *16*, 37-46.
152. Vayer, M.; Vital, A.; Sinturel, C., New Insights into Polymer-Solvent Affinity in Thin Films. *Eur. Polym. J.* **2017**, *93*, 132-139.
153. Lin, S.; Chen, C.-T.; Bdikin, I.; Ball, V.; Grácio, J.; Buehler, M. J., Tuning Heterogeneous Poly (Dopamine) Structures and Mechanics: In Silico Covalent Cross-Linking and Thin Film Nanoindentation. *Soft Matter*. **2014**, *10*, 457-464.
154. Peters, K.; Raupp, S.; Hummel, H.; Bruns, M.; Scharfer, P.; Schabel, W., Formation of Blade and Slot Die Coated Small Molecule Multilayers for Oled Applications Studied Theoretically and by Xps Depth Profiling. *AIP Advances* **2016**, *6*, 065108.
155. Shard, A. G., et al., Argon Cluster Ion Beams for Organic Depth Profiling: Results from a Vamas Interlaboratory Study. *Anal. Chem.* **2012**, *84*, 7865-7873.
156. Ohisa, S.; Pu, Y.-J.; Yamada, N. L.; Matsubaa, G.; Kido, J., Influence of Solution- and Thermal-Annealing Processes on the Sub-Nanometer-Ordered Organic–Organic Interface Structure of Organic Light-Emitting Devices. *Nanoscale* **2017**, *9*, 25-30.
157. Kim, T.; Yoon, J.; Kim, Y.; Aspnes, D.; Klein, M.; Ko, D.-S.; Kim, Y.-W.; Elarde, V.; Coleman, J., Analysis of Interface Layers by Spectroscopic Ellipsometry. *Appl. Surf. Sci.* **2008**, *255*, 640-642.
158. Aizawa, N.; Pu, Y.-J.; Watanabe, M.; Chiba, T.; Ideta, K.; Toyota, N.; Igarashi, M.; Suzuri, Y.; Sasabe, H.; Kido, J., Solution-Processed Multilayer Small-Molecule Light-Emitting Devices with High-Efficiency White-Light Emission. *Nat. commun.* **2014**, *5*, 5756.
159. Ho, S.; Liu, S.; Chen, Y.; So, F., Review of Recent Progress in Multilayer Solution-Processed Organic Light-Emitting Diodes. *J. Photon. Energy* **2015**, *5*, 057611-057611.